Rheometry and Direct Flow Observations of a Model Wax-Oil System

by

Christopher Dimitriou

Submitted to the Department of Mechanical Engineering
in partial fulfillment of the requirements for the degree of

Master of Science in Mechanical Engineering

at the

MASSACHUSETTS INSTITUTE OF TECHNOLOGY

June 2010

Author .....
Department of Mechanical Engineering
May 18, 2010

Certified by .....
Gareth H. McKinley
Professor
Thesis Supervisor

Accepted by .....
David Hardt
Chairman, Department Committee on Graduate Theses

Rheometry and Direct Flow Observations of a Model Wax-Oil System

by

Christopher Dimitriou

Submitted to the Department of Mechanical Engineering
on May 18, 2010, in partial fulfillment of the
requirements for the degree of
Master of Science in Mechanical Engineering

Abstract

Waxy crude oils are a commonly encountered type of crude oil which must be dealt with by oil production companies. They are characterized by a gel-like behavior at temperatures below their wax appearance temperature (T_{wa}) and often exhibit a yield stress. The restart of pipelines containing gelled waxy crude is a commonly encountered problem in production scenarios where low ambient temperatures are encountered, especially due to the increasingly important role that deep-water oil exploration has in meeting production needs. In this thesis, a model wax-oil system is formulated which closely mimics the thermorheological complexity of an actual waxy crude oil. The composition of the model system is characterized using chemical characterization techniques, and the basic rheological properties of these components are probed using temperature sweeps and stress sweeps. Large amplitude oscillatory shear (LAOS) is also used to gain additional insight into the rheology of the model system. The results from the LAOS measurements show that the wax-oil system exhibits a strain stiffening and shear thinning response under oscillatory shear. The system is then studied using a combined approach of rheology and flow measurement techniques. We describe the design, fabrication and calibration of a quantitative flow imaging apparatus that enables measurements of the local kinematics within the model fluid using Particle Image Velocimetry (PIV). This Rheo-PIV approach forms the basis for the study of the model fluid using *Flow Assurance Rheometry.* The data from this combined approach shows that the model fluid exhibits a complex behavior due to heterogeneities within the domain of the fluid. Specifically, the wax-oil system is shown to consist of two distinct phases: rigid clumps or fragments that are formed by aggregates of wax crystallites, and fluid-like regions which contain fewer wax precipitates. It is shown that under imposition of a steady shear stress, these rigid fragments break down over time into smaller pieces, and this contributes to the fluidization of the model wax-oil. The effect of surface roughness on the dynamics of this shear-induced fragmentation process is also investigated. It is shown that when the gelled system is in contact with a roughened surface, the fragmentation process happens faster.

Thesis Supervisor: Gareth H. McKinley
Title: Professor

Acknowledgments

I would first like to acknowledge the help I have received from a number of people who have worked with me to bring this thesis to fruition. My advisor of course, Gareth McKinley, as well as the other Chevron project collaborators whose input was valuable - among them are Rama Venkatesan, Patrick Doyle and Robert Armstrong. I would also like to thank everyone in the NNF group for being such a fun group of people to work with for the past two years. Lastly, I am grateful to my friends and family for their support.

Contents

List of Figures

List of Tables

Chapter 1

Introduction

Crude oil is a widely traded and important commodity in the global economy. Since the by-products of crude oil are vital to so many different industries, the production of crude oil has had to steadily grow in order to keep up with demand. In the United States alone, consumption of crude oil has continuously increased since the beginning of the 20th century. Production of crude oil in the US peaked in the 1970's (shown in Figure 1-1), and consequently imports of crude oil have had to grow in order to keep up with this growing demand [41].

Predictions made in the mid 20th century such as those by Hubbert showed that production of crude oil within a given region would follow a bell shaped curve which, after peaking, would decrease slowly over time [25]. While the Hubbert peak theory predicts that eventually global production of crude oil will reach a peak, the point in time at which this peak will occur is still unclear - although estimates are typically on the order of several decades [8]. One of the reasons for the exact point in time where world oil production will peak being difficult to predict is that modern oil exploration techniques have been uncovering new reserves of petroleum in remote locations. As the technology used to both find these reserves and extract the oil from them continues to develop, total global production of oil can continue to grow. Hence, a significant segment of the oil industry today is focused solely on the exploration and extraction of crude oil from remote reserves. In many cases these remote reserves are offshore and in deep waters [10].

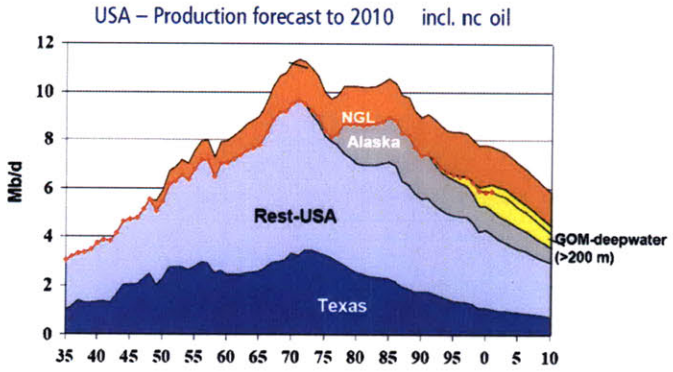

Figure 1-1: Production of crude oil in the United States, shown for different sources. Image from a paper by Tsoskounogiou [44]. Total production peaked in the 1970's, while deepwater production has seen an increase in the past decade

Understanding the composition of crude oil is an important first step in determining what type of petroleum products can be extracted from it, but also in determining the best way to extract the oil. In general, the composition of crude oil consists of a mixture of hydrocarbon molecules. A large percentatge of these hydrocarbon molecules are alkanes, which consist of only carbon and hydrogen atoms, and in general have the chemical formula C_nH_{2n+2} [40]. These alkanes tend to have many structural variants (or isomers), and so it is common to denote their straight chained variant as an n-alkane. Another variant of these alkanes are cycloalkanes, which are similar to alkanes but their molecules consist of one or more rings of carbon. For cycloalkanes, the chemical formula is generally of the form $C_nH_{2(n+1-g)}$, where g is the number of rings in the molecule. The typical range of %wt. by atom for crude oil is given in Table 1.1, while the typical ranges of the amount of cycloalkanes relative to n-alkanes are given in Table 1.2, . The physical properties of crude oil (such as its viscosity, or density) depend on the relative proportions of alkanes and cycloalkanes to other molecules which may be part of the mixture.

Wax is a commonly occurring component of crude oil, and is generally characterized as consisting of paraffins, which is another name for the larger alkanes (or hydrocarbons of the form C_nH_{2n+2}) within the oil mixture [41]. In the case of waxes, "large" tends to denote a value of n ranging from $20 \leq n \leq 40$ [41]. Waxy crude oils are thus crude oils which have a relatively large amount of wax in them [49].

Element	Percent range
Carbon	83 - 87%
Hydrogen	10 - 14%
Nitrogen	0.1 - 2%
Oxygen	0.1 - 1.5%
Sulfur	0.5 - 6%

Table 1.1: Range of elements present in crude oil, together with typical % wt. range for each element (data taken from Simanzhenkov and Idem [40])

Type of Hydrocarbon	Percent range
Paraffins	15- 60%
Cycloalkanes	30 - 60%
Aromatics	3 - 30%

Table 1.2: Range of types of hydrocarbons present in crude oil, together with typical % wt. range for each type (data taken from Simanzhenkov and Idem [40])

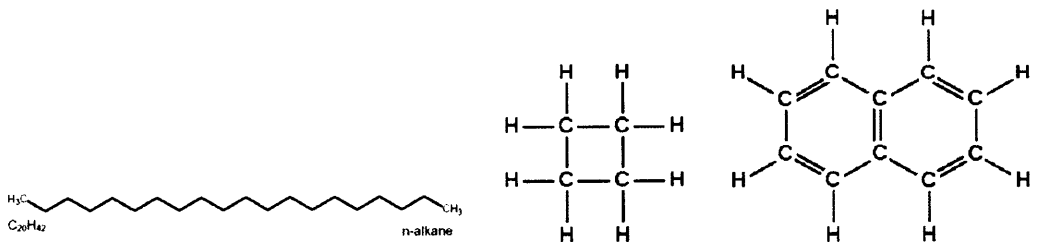

(a) An n-alkane (b) Cyclobutane (c) Naphthalene

Figure 1-2: Examples of the types of molecules which are present in crude oil. The compound shown in Figure 1-2(a) is an n-alkane, while the compound in Figure 1-2(b) is a cycloalkane, specifically cyclobutane. Figure 1-2(c) is an example of an aromatic hydrocarbon, in this particular case naphthalene. The carbon atoms in aromatic hydrocarbons are unsaturated, unlike the cycloalkanes.

When isolated, paraffin is usually a solid at room temperature, with a melting point which tends to lie between 50°C and 65°C [41]. As one might expect, the physical properties of a waxy crude oil can vary greatly depending on the percentage of wax that they contain. Typically the rheology of waxy crude oils is very sensitive to temperature changes due to the fact that it is possible for these waxes to crystallize and then precipitate out of the oil with a small decrease in temperature. With modern oil extraction techniques involving flow of oil through long pipelines reaching deep reservoirs (~10km) through cold seawater (~5°C) [22], changes in the rheological behavior of these waxy oils due to temperature drops are becoming more and more important. As a result, there is considerable amount of interest in the oil industry to improve current understanding of the thermorheological behavior of waxy-crude oils [10] [22] [26].

Within the oil industry, there is an entire sub-discipline that deals with the problems encountered while attempting to ensure the continuous flow of crude oil through production lines. This research area is called *Flow Assurance.* Many of the problems flow assurance specialists must deal with are associated with preventing the occurrence of a gelled pipeline. A gelled pipeline may occur in the case where the temperature of the crude oil drops locally (near the wall) below a given point at which wax, or other precipitates begin to form. This type of occurence is shown schematically in Figure 1-3. Gelled waxy crude oils often exhibit rheological behavior akin to yield stress fluids. Specifically, there exists a stress, or range of stresses, over which the viscosity of the gelled system decreases by several orders of magnitude [47]. Thus, in order to restart flow of a gelled pipeline, a pressure larger than the typical operating pressure is required to exceed the yield stress of the fluid at the wall. For a newtonian fluid (which is what a crude oil is at high temperatures), this typical operating pressure is given by the well known result:

$$\frac{\Delta P}{\frac{1}{2}\rho V^2 \frac{L}{D}} = f = \frac{64}{\mathrm{Re}} \tag{1.1}$$

Where L is the length of the pipeline, D is the diameter of the pipe, V is the bulk

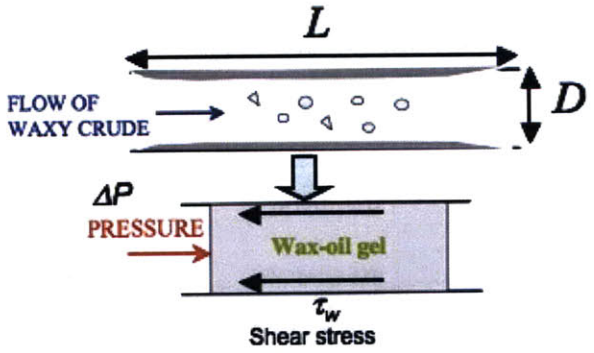

Figure 1-3: Gelation of a pipeline through which waxy crude oil is transported

velocity of the fluid in the pipe, and Re is the Reynolds number for the flow in the pipe (given by $\mathrm{Re} = \frac{\rho V D}{\mu}$). However, in the case of a gelled pipeline, the pressure ΔP must exceed that given above in order to exceed the yield stress of the gel at the pipe wall. This pressure can be roughly determined by carrying out a force balance along a cylindrical length of gelled fluid in a pipeline. It is thus given by:

$$\Delta P = \frac{4L\tau_y}{D} \tag{1.2}$$

Where τ_y is the yield stress of the gel, L is the length of the pipe and D is the diameter of the pipe. These scenarios are typically avoided by insulating pipelines, or even heating them. However, current flow assurance strategies tend to be too conservative, and thus too costly of an option to make oil production under adverse conditions viable [37].

A better understanding of the thermorheological behavior of waxy crude oils would facilitate the improvement of these strategies. One of the main limitations of current flow assurance strategies is that they are based on simple empirical models that describe the rheological behavior of precipitate-containing production fluids [37] (an example of such a model is the one proposed by Pedersen in [35]). Thus, an in-depth experimental approach that uncovers how the rheology of these fluids is affected by the presence of precipitates is required. The work in this thesis deals with the experimental aspect of this approach. The term *Flow Assurance Rheometry* is used to refer to new experimental techniques which are developed for the purpose of studying

the rheology of waxy crude oils. These techniques involve direct measurements of the velocity field of a wax-oil system undergoing deformation in a rheometer. A large portion of this thesis discusses the application of flow assurance rheometry to studying shear heterogeneities in a model wax-oil system. Yielding of the system under an externally-imposed shear stress is studied, as well as the evolution of the structure of the system under steady imposed shear rates. This experimental approach can then be used to verify constitutive models which are based on micro-scale simulations.

Chapter 2

Literature Review

2.1 Rheology of waxy crude oils

The presence of wax in petroleum oils and its practical importance to production of of crude oil has been known for a long time. There are examples in the literature of the study of wax precipitates in petroleum going back at least as far as the 1920's. Padgett et. al. [34] published a paper in 1926 which studied the morphology of wax crystallites that are formed in a number of petroleum-derived samples. The authors placed their samples between crossed polarizing filters and observed how light was transmitted through these samples under a microscope. Due to the optical anisotropy of the wax precipitates, this technique allows for one to observe wax crystallites or precipitates as bright spots in a dark field image. This phenomenon is also known as birefringence [28], and it results from the decomposition of incoming polarized light into two components, an "ordinary" and "extraordinary" ray. This occurs when the index of refraction of a material is directionally dependent [17]. Padgett used this technique to study the morphology of these precipitates for both a model system (paraffin wax dissolved in oils of varying viscosity), as well as in wax distillates which were derived from a particular crude oil. Some interesting observations were made - specifically that the oil viscosity is connected to the size of wax crystallites which are formed, as well as there being a large variation in the shape of the wax crystallites between the different types of samples. Among these types of samples are slack wax (a

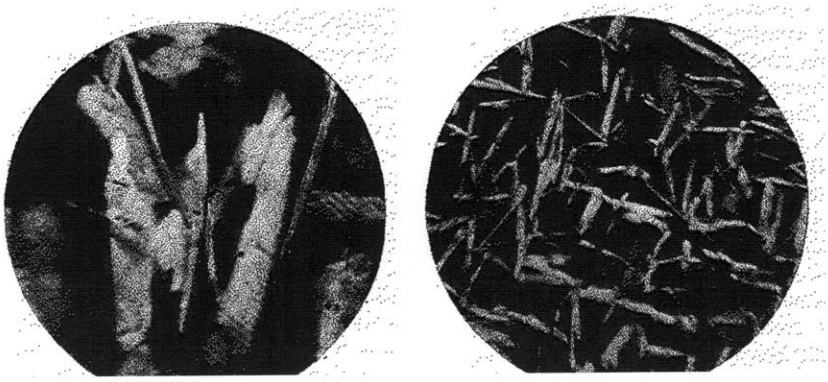

Figure 2-1: Images from Padgett [34] showing size and shape of wax precipitates in oil-wax mixtures prepared in the lab. The larger wax precipitates in the image on the left are due to the lower viscosity of the oil in the mixture. Both images were taken at a magnification of 300×.

semi-refined wax), heavy raw-wax distillate, and mixtures of paraffin wax in mineral oil.

While Padgett described the morphology of wax precipitates formed in petroleum products in great detail, his analysis lacked any description of the possible effects these precipitates may have on their rheological behavior. The paper published by Gil and Russell in 1954 [21] attempted to address some of these issues. One of the most important findings in [21] is the inadequacy of the *pour point*, T_{pour}, as an index of pumpability for crude oils. The pour point is an empirically-determined temperature which indicates the point at which an oil can flow under the effect of gravity (ASTMD97 [16]). In general, it is helpful to understand the difference between pour point and wax appearance temperature (denoted in this thesis as T_{wa}). In theory, the wax appearance temperature should indicate the point at which wax precipitates of the form shown in Figure 2-1 first begin to form in a crude oil. Since it is often difficult to determine this temperature exactly, the pour point was developed as a standardized test which could indicate the temperature at which wax precipitates considerably change the rheology of the oil. The rheology of the oil may only change by a small amount when the first wax precipitates form, so in general the pour point temperature is lower than the wax appearance temperature for a specific oil.

For these and other reasons, Gil and Russell state that the pour point temperature

can only provide a quick indication of whether or not an oil will be able to easily flow through a pipeline (a "go/not go" test). Because of this, Gil and Russell emphasize the importance of obtaining more reproducible results, which could be achieved through the use of a rotating cylinder viscometer. Rather than actually using a concentric cylinder viscometer in their experiments, Gil and Russell obtained most of their data by observing the flow behavior of waxy fuel oils in capillary tubes. The authors showed how the rheology of these fluids depends on thermal history of the oil, and also indicated some of the limitations of their experimental methods. Specifically they showed that the axial pressure distribution in a gelled pipeline or capillary tube is not always linear (due to the bulk compressibility of the gel).

A more recent paper published by Perkins and Turner [36] attempted to overcome some of the shortcomings of Gil and Russell's approach by carrying out measurements of the rheology of Prudhoe Bay crude oil using a bob and cup viscometer. Perkins and Turner obtained flow curves of the shear stress - shear rate and fitted an empirical equation to this data. In addition, the authors provided a brief discussion on how the compressibility of the gelled oil will result in a longer time period required for restart of a gelled pipeline. According to Perkins and Turner the combination of compressibility and thixotropic behavior of the gelled oil, result in a pressure wave requiring a long time to travel down a gelled pipeline.

Thixotropy, in general and as defined by Perkins and Turner, is the tendency of a fluid to experience degradation at steady shear rates, i.e. a decrease in viscosity or other rheological properties over time [5]. This type of behavior is relevant to a restart scenario because in a section of a gelled pipeline the gel near the inlet will first "feel" the effects of high pressure at the inlet due to its compressibility. Subsequently, the fluid near the inlet degrades faster than the fluid near the outlet (this degradation is a result of the thixotropic behavior of the gel). This results in varying rheological properties of the fluid along the length of the pipe. Thus, a lower pressure is required to yield the gel in the pipeline, because the entire length of the gel is not being yielded at the same time. Using an experimental apparatus in the lab, the authors [36] showed that for a 50 foot long pipe of inner diameter D =0.335

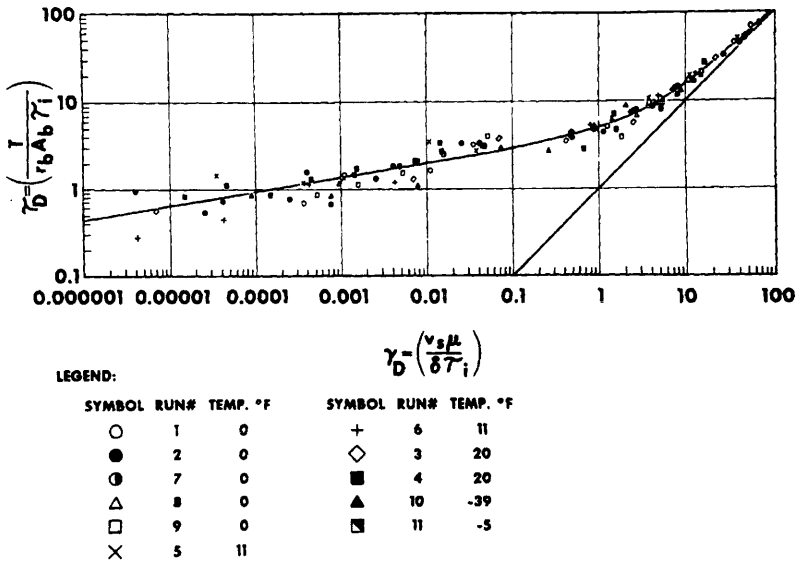

Figure 2-2: Flow curve of scaled shear stress vs. shear rate for Prudhoe Bay crude oil from the paper by Perkins [36]. Variables are scaled appropriately: μ is the Newtonian viscosity at high shear rates, τ_i is the yield strength of the oil sample, δ is the gap size between the cup and bob. The solid line is the empirical fit developed by the authors.

inches, approximately 20 minutes were required for the pressure distribution along the pipeline to settle into a steady state. Although not discussed here, the dynamics of gelled pipeline restart are described in detail in the papers by Davidson et. al. from 2004 [12] and Vinay et. al. from 2007 [46].

Wardhaugh and Boger [50] make note of many of the flaws in the prior approaches towards measuring the yielding behavior of waxy crude oils. They also rejected the approach of using pipelines or capillaries to study the yielding of waxy crude oils because of the coupling between compressibility and thixotropy. Instead, Wardhaugh and Boger took an approach where four different experimental setups were utilized to study yielding of a waxy crude oil (in their case a Jackson-Hutton crude oil and a McKee crude oil). The first of these involved the use of the vane geometry, while the other three setups utilized a cone and plate geometry under constant rotation, oscillatory shear, and a controlled constant stress (i.e. creep tests). The data of Wardhaugh and Boger shows that the two crude oils exhibited a yielding behavior which consists of three distinct stages (these stages are shown in Figure 2-3). The first is an

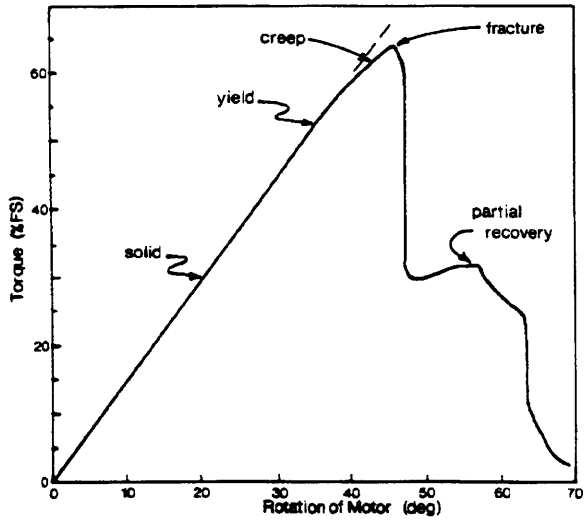

Figure 2-3: Yielding behavior of the Jackson-Hutton crude oil used by Wardaugh and Boger. At low strains the sample behaves as an elastic solid, with a linear stress-deformation curve. However, at high enough deformations the sample plastically deforms and the stress drops. Some recovery of the sample is also observed upon removing the imposed deformation.

initial elastic response to an imposed strain from which the fluid can recover. Upon unloading, the elastic response phase is then followed by a slow plastic deformation of the fluid (at higher strains), which is subsequently followed by a sudden failure of the sample. The sudden failure of the sample is evident from the dramatic decrease in the shear stress which occurs above a given strain value. The paper by Chang and Boger is another instance in the literature where this type of behavior is also shown [9].

More recent papers such as those published by Visintin et. al [47] [48] studied not only waxy crude oils, but also crude oil emulsion gels formed due to the presence of water. In [47] Visintin uses a combined experimental approach was taken which utilized DSC (Differential Scanning Calorimetry), Microscopy and Rheology in order to understand the effects of precipitated wax on the rheological behavior of a paraffinic crude oil (with no water content). The authors in this paper demomnstrated that the viscosity-shear stress behavior of their gelled crude oil showed a dramatic decrease in viscosity above a critical value of the shear stress. This shear stress can be effectively

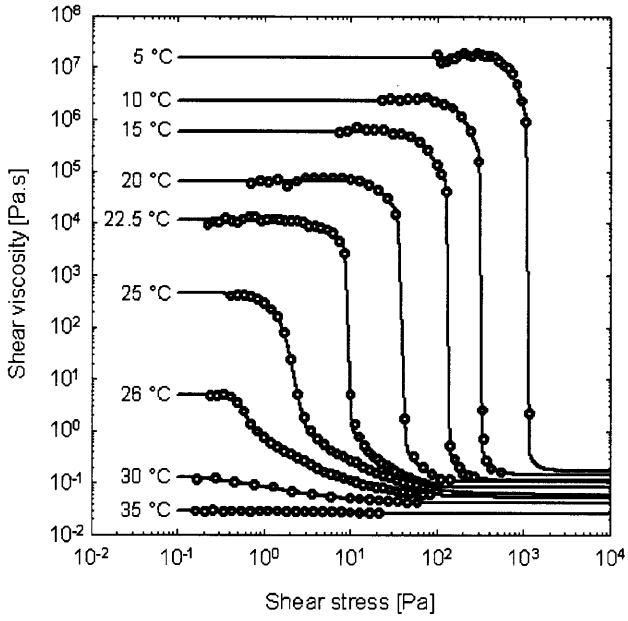

Figure 2-4: Data from [47] by Visintin showing the yield stress for crude oil "A" (a crude with a 5%wt. wax content) held at a range of temperatures. Solid lines indicate the fit to the RBC model.

termed a yield stress, however the transition to lower viscosities is more gradual at higher temperatures, and occurs at lower stresses. Visintin's data is shown in Figure 2-4. The authors fit the particular data using a Roberts-Barnes-Carew model [38] which is of the form given in 2.1.

$$\frac{\eta' - \eta'_\infty}{\eta'_0 - \eta'_\infty} = \frac{1}{1 + (\sigma/\sigma_c)^m} \tag{2.1}$$

Visintin also showed how the cooling rate of the waxy crude oil used in its preparation can considerably affect the value of its storage and loss moduli, G' and G''. In particular, higher cooling rates favor lower values of G' and G'', while slower cooling rates lead to a stronger gel network - this is the very concept of thermal history, which is responsible for variations in the rheological behavior of the system. Visintin compared his data to images showing wax precipitates formed in the crude oil which has been cooled below the gelation temperature at low and high cooling rates. These images (shown in Figure 2-5(a)) indicate that slower cooling times favor larger crystal formation and this is the reason for the stronger gel network (or higher values of G'

and G''). The slower cooling times will also result in less aging of the gel during any subsequent "hold time" where the material is kept at a constant temperature and no stress is imposed - this data is shown in Figure 2-5(b). With faster cooling rates, Visintin stated that the lower gel strength is a result of the wax crystals forming smaller clusters.

Motivated by these observations, Visintin noted that the gelled crude oils exhibit a behavior similar to weakly attractive colloidal gels, for which the rheological parameters are determined by the interactions between the wax precipitates. These interactions depend heavily on their initial arrangement, size and volume fraction, which is the reason for their sensitivity to variations in thermal and mechanical history. The structure of the crystallites can also be characterized by a fractal dimension, D, which grows as crystallites break apart and become smaller under applied stresses.

Visintin carried out a quantitative comparison between the behavior of the waxy crude oil and that of a colloidal gel formed by fused silica in paraffin oil. Specifically, the plot shown in Figure 2-6 indicates a general agreement between the plot of relative viscosity vs. volume fraction for the waxy crude oil and the fused silica colloidal gel. The relative viscosity is a viscosity scaled by a value which Visintin denotes as η_{sol}. The value η_{sol} is essentially an extrapolated viscosity obtained by following the thermorheological behavior of the waxy crude oil as temperature decreases, while not accounting for the dramatic change in this behavior which occurs at the gelation temperature (this value can be obtained by looking at the viscosity from Figure 2-4 at high shear stresses). The volume fraction of wax crystallites was determined through the use of Differential Scanning Calorimetry, or DSC, which relates the latent heat to the mass of wax precipitates which form as temperature is changed.

Later Visintin et. al. [48] studied another waxy crude oil, which contains a rather high amount of wax ($\sim$ 10% wt.). The authors formulated an emulsion of this oil in water - this was achieved by using a stirrer to create the emulsion, while the size of droplets was controlled and measured by the authors by using laser light scattering. The effect of changes in water fraction on rheological behavior was studied. The authors showed an increase in both of the viscoelastic moduli for higher amounts of

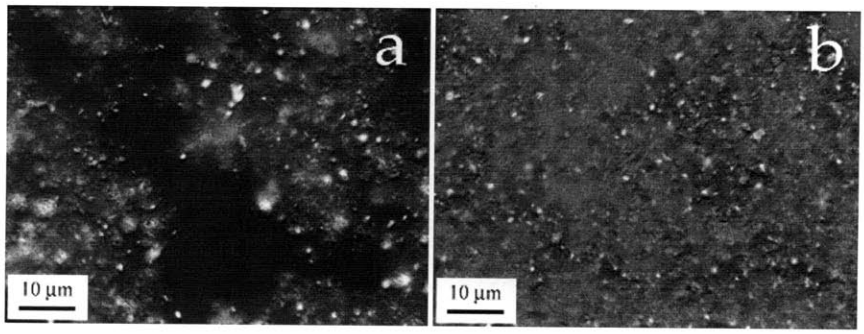

(a) Optical microscopy images of wax microstructure formed in the crude oil studied by Visintin. On the left is a sample cooled at 0.05°C per minute and on the right is a sample cooled at 1°C per minute. Images are taken at a magnification of 100×, with the sample located between crossed polarizers. Higher overall brightness of the image on the left is a result of the higher depolarization of the crystals which indicates a higher compactness.

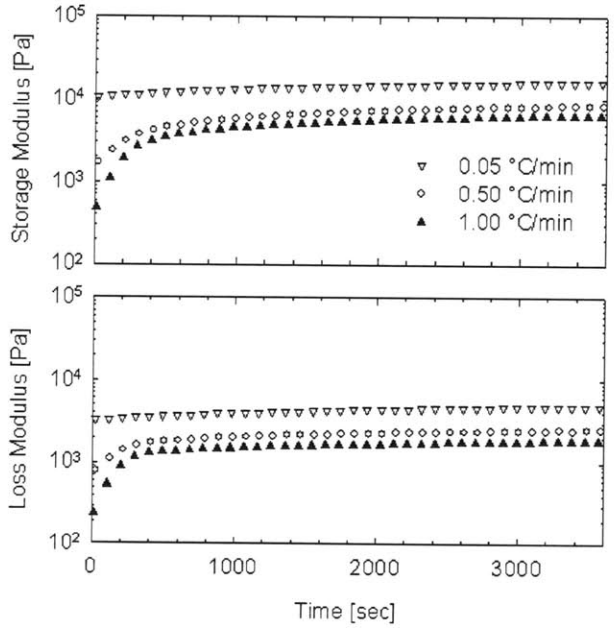

(b) Plot showing change in G' and G'' of the waxy crude oil over time. This change (or aging behavior) can be seen to be different for the samples treated with different cooling rates

Figure 2-5: Data from the work of Visintin [47] showing the effect of cooling rate on the overall strength of the waxy crude oil gel and the aging behavior that it experiences. The effect of cooling rate on the resulting microstructure that develops is shown in Figure 2-5(a).

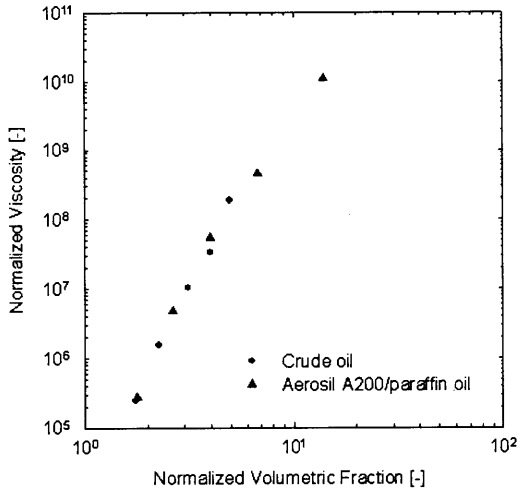

Figure 2-6: Comparison of relative viscosity vs. volume fraction of solids for the waxy crude oil studied by Visintin and a colloidal gel of fused silica in paraffin oil. The volume fraction for the waxy crude oil is normalized by the volume fraction of wax crystallites at the gelation temperature (all of these volume fractions are determined using differential scanning calorimetry).

water. They argued that the mechanism for this is that paraffin crystals precipitate onto water droplets within the emulsion, resulting in a stabilization of the emulsion. The surface of the water droplets act as nucleation points for this precipitation, so that during the process of gelation, precipitates will first form on these surfaces. After more time passes, wax crystallites can completely cover the liquid-liquid interface of the droplets, and prevent them from coalescing. An extended gel network which then forms in the spaces between the droplets results in an even stronger gel strength. This particular process is shown diagramatically in Figure 2-7. The data from this paper, together with the interpretations provided by Visintin and coauthors, indicates that it is preferable to pump crude oil with low water fractions along pipelines. It also emphasizes the importance of accounting for residual water fraction among the standard tests which are carried out on the rheology of waxy crude oils in the field.

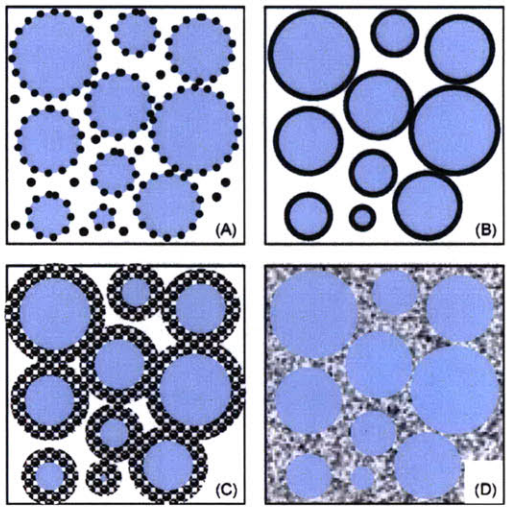

Figure 2-7: Diagram indicating process through which wax precipitates form in a waxy crude oil emulsion. Initially crystals nucleate onto the water droplets (top left), and eventually cover the entire droplet (top right). As more crystallization occurs, the droplets are entrapped by the neighboring droplets. Eventually the wax crystals span the entire volume when gelation has completed (bottom right)

2.2 Developments in Imaging Techniques for Waxy Crude Oils

In recent years there has been considerable progress made in improving the types of imaging techniques used to quantify the morphology of waxy crude oils. A paper published by Gao in 2006 used high resolution micrographs in order to understand the fractal nature of wax precipitates formed in a waxy crude oil[18]. While the experimental setup that was used by Gao was similar to those used by Padgett and Visintin, Gao did conduct an extensive study of the wax structure by using direct fractal characterization. Gao compared three crude oils which were either in their virgin form, or treated by a pour point depressant (PPD) which inhibits wax crystallization. Gao reported fractal dimensions, D, of approximately 1.5, with the value of D being slightly higher for the pour point depressant-treated oil.

While many works in the literature have used a crossed polarizing filter microscope setup, the paper by Kanè published in 2002 took a different approach by using transmission electron microscopy after cryofixation, cryofracture and replica prepara-

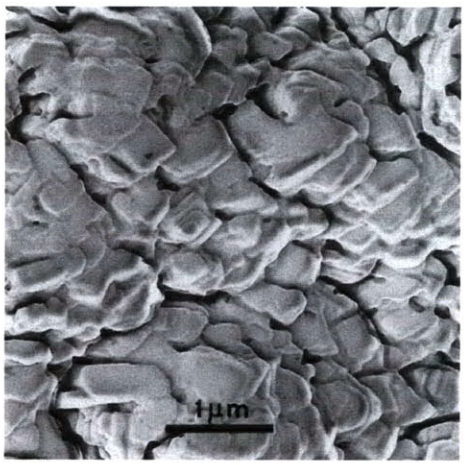

Figure 2-8: TEM image obtained by Kanè showing the morphology of paraffin crystals precipitated in a waxy crude oil. The image shows overlapping platelets of characteristic scale $\ell \sim 1\mu$m. These platelets form a complex 3 dimensional structure

tion. TEM was used to look at the morphology of paraffin crystals in crude oil which have been precipitated under both quiescent conditions and under shear [27]. The use of TEM allows the rather complex 3-Dimensional structure of the wax crystallites to be observed, which in turn provides more insight into potential interactions between these crystal formations. Kanè's results showed that the precipitates formed into overlapping plate like structures, of size $\sim 1\mu$m. This types of shapes cannot be observed using the simple 2D transmission imaging techniques such as those employed by Padgett.

On a more practical note, there are some recent efforts in the literature which have been aimed at understanding the mechanism by which failure of the gel networks formed in waxy crude oils occurrs. A notable example of this is a paper by Lee et. al. [29]. These authors show that thermal history of a waxy crude oil can actually have an effect on whether a gel fails at the interface with some solid surface (an *adhesive failure*) or within its bulk (*cohesive failure*). The difference between these two types of failure is shown diagrammatically in 2-9(b). Lee demonstrates the occurrence of these two types of yielding by showing a delineation point on a plot of failure stress against cooling rate. Lee measures failure stress by imposing a stress ramp on the sample and observing the stress at which the shear rate starts to increase rapidly.

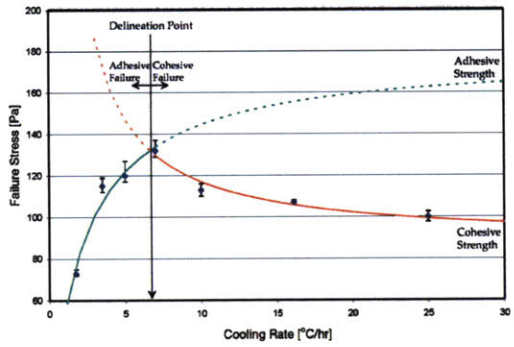

(a) Figure from paper by Lee [29] showing the delineation point observed whereby yielding in the waxy crude oil switches from occurring adhesively to cohesively

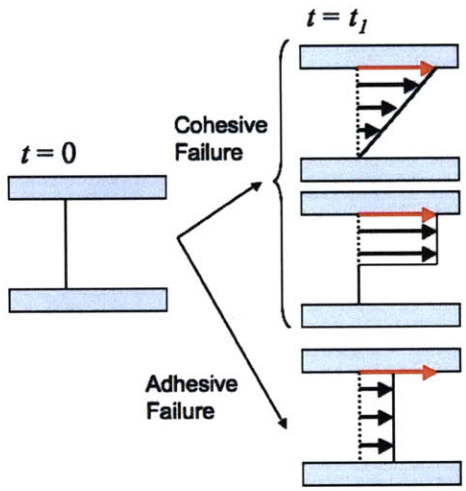

(b) Diagram indicating the difference between a material yielding through the adhesive mechanism and the cohesive mechanism.

Figure 2-9: Influence of cooling rate on yielding mechanism experienced by a waxy-crude oil. The difference between the two mechanisms is shown in Figure 2-9(b), where the displacement field of the material is shown at an initial time and a later time. Movement of the fluid is shown as black arrows, while the red arrow indicates movement of the top shearing surface. For cohesive yielding, the material can actually yield through two different mechanisms - either uniformly or at a localized point within the bulk. To distinguish between these two mechanisms, it is necessary to directly measure strain/strain rate within the material.

For low cooling rates, the failure stress increases, however when the cooling rate goes past the delineation point, the failure stress begins to decrease. This particular data is shown in figure 2-9(a). Lee argues that this is because above a certain cooling rate, the wax crystallites which form are much smaller and hence the gel strength is lower with faster cooling rates. This in turn facilitates failure through the cohesive mechanism. On the other hand, at low cooling rates the bulk strength of the gel is higher (due to larger crystallite formation) and the failure will be due to the wax-oil gel no longer adhering to the solid surface. The delineation point is defined as the cooling rate at which the mode of failure switches from one mechanism to the other.

One of the limitations of Lee's approach is that it does not directly observe the mechanism of failure, but rather infers it indirectly from measurements of the failure stress. One way to build on the work of Lee would be to directly observe the defor-

mation field of the waxy crude oil gel within the rheometer while an imposed stress is being applied. By observing whether or not a slip velocity develops at the gel-surface interface, then it is possible to immediately determine the mechanism of failure. Furthermore, such an approach would also allow one to observe the dynamics of evolution in the flow profile with time, i.e. whether or not the flow continues to manifest as an interfacial slip for long times. At the time of writing, however, there are no examples in the literature of using such a methodology to directly observe this type of behavior in an actual crude oil or a model wax-oil system. This thesis thus seeks to develop an experimental framework which can directly observe the flow profiles of a waxy oil gel undergoing shear as a function of time, temperature and imposed stress.. These observations are used to gain insight into the complex spatiotemporal evolution of the structure of wax precipitates.

2.3 Combining rheology and velocimetry

When conducting experiments in a rheometer certain *a priori* assumptions are made about the flow field within the sample undergoing deformation. For example, if one is to use a steady shear rate test in a cone and plate geometry to measure the viscosity of a sample, the assumption of a uniform shear rate throughout the sample must hold in order to calculate a true viscosity from the measured torque and rotation rate. The viscosity of the fluid can then be calculated from the well known result in Figure 2.2 as given by Bird, Armstrong and Hassager [6].

$$\eta = \frac{\tau_{\theta\phi}}{-\dot{\gamma}_{\theta\phi}} = \frac{3\mathcal{T}\vartheta}{2\pi R^3 W} \tag{2.2}$$

For certain types of non-Newtonian fluids, these assumptions may not hold. For example, some fluids may experience slip at the interface with a solid boundary. Such issues have been well known and documented within the field of rheology for quite some time. A comprehensive summary of the effects of slip on rheological measurements is provided by Barnes [4]. Furthermore, there exist methods by which rheological measurements can be corrected for slip [51]. These methods typically

involve observation of systematic gap dependence in the rheological data, plus the use of a plate-plate geometry so that the gap can be varied. Specifically, torque and rotation rate are measured at different gaps for the same sample at the same shear stress, while a correction factor is applied to the data as given in the equation below. The result given in Equation 2.3 (derived by Yoshimura and Prud'Homme) allows one to determine the shear rate being experienced by the bulk of the fluid ($\dot{\gamma}_R$) at the rim of the parallel plate at a given imposed stress by measuring the apparent shear rate at two different gap heights for a plate plate geometry ($\dot{\gamma}_{aR1}$ and $\dot{\gamma}_{aR2}$) at the same imposed stress.

$$\dot{\gamma}_R(\tau_R) = \frac{H_1\dot{\gamma}_{aR1}(\tau_R) - H_2\dot{\gamma}_{aR2}(\tau_R)}{H_1 - H_2} \tag{2.3}$$

One caveat to this result is that it is based on the assumption that the slip velocity that the fluid experiences on the upper and bottom geometry depends solely on stress, and is the same for both upper and lower surfaces.

The review of Barnes outlines a number of experimental artifacts that may show up in rheological data as a result of slip. However, the only way to directly observe whether or not some type of shear inhomogeneity is occurring within a sample, be it wall slip or internal yielding, is to take measurements of fluid velocity in order to observe the flow field within the sample. One potential method which enables measurement of the flow field in a sample undergoing shear within a rheometer is Particle Image Velocimetry, or PIV for short. PIV, as an experimental method, developed out of Laser Speckle Velocimetry[2]. The basic principle behind both laser speckle velocimetry, and PIV, is to place tracer particles within a fluid and use observations of their movement to compute the velocity field of the fluid. One of the important differences between these two methods is the seed particle concentration - PIV requires a lower seed particle concentration than laser speckle velocimetry, since speckle patterns are undesired in PIV and can only occur with a large amount of seed particles. An important part of any PIV system is that the seed particles are chosen appropriately (namely they are small enough, and can be dispersed evenly) so that

they accurately follow the local deformation field in the fluid. Hence, if it is possible to track these seed particles within a certain domain of the fluid, the velocity field within that domain can be determined [2] [7].

In the PIV approach, the velocity field is obtained by carrying out a cross correlation operation between "interrogation windows" in two subsequent images. Each interrogation window is a grid of $q \times p$ pixels which must contain a minimum number of seed particles. Typically in a dark field image, these particles will show up as bright spots since they are reflecting light which is directed onto them (usually laser light). The procedure is shown diagrammatically in Figure 2-10. The red box in the full image on the left is the interrogation window (size $q \times p$ pixels). The optimum displacement is determined for the window from time t_1 to line up with the window from the next frame (at time t_2) by using the cross correlation operation. Wereley and Meinhart gives the following equation for the cross correlation operation which must be evaluated for each interrogation window [7].

$$\Phi_k(m,n) = \sum_{j=1}^{q} \sum_{i=1}^{p} f_k(i,j) \cdot g_k(i+m, j+n) \tag{2.4}$$

In 2.4 q and p give the size of each interrogation window in pixels, while $f_k(i,j)$ and $g_k(i,j)$ are the grayscale values for each of the pixels in the interrogation windows of the two frames. When the value of Φ_k is calculated for a number of different values of m and n, then a two dimensional intensity field shows Φ_k as a function of m and n. The point at which this is a maximum is the value of m and n which correspond to the displacement which matches up the interrogation windows of the two frames. this displacement can then be computed into a point value of the in-plane velocity, assuming the time spacing between the frames is known.

There are some limitations associated this technique. One of these limitations is that each interrogation window must contain an adequate number of seed particles (typically 10 or more [2]), otherwise the function Φ_k will not give a distinct peak corresponding to the the actual displacement for the region given by that window. It is possible to track individual particles in the flow, however this approach is the basis

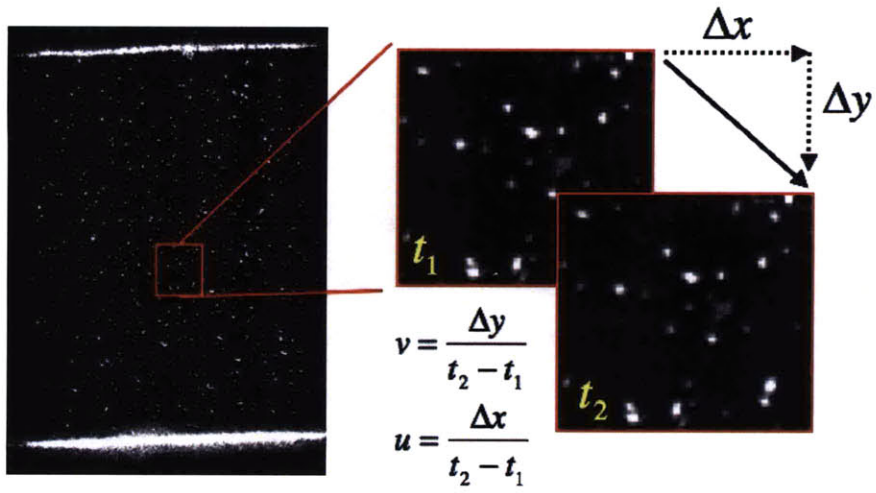

Figure 2-10: Diagram showing how images are divided up into interrogation windows, which are shifted such that they align with the next frame's windows. The displacements Δx and Δy can be used to determine the velocity, given that the time spacing between each frame is known.

of particle tracking velocimetry (or PTV) which is another velocimetric technique. Due to the differences between PTV and PIV, PIV will not give individual velocity measurements corresponding to a single particle - this may be another limitation since it may be necessary to obtain velocity measurements to a greater spatial resolution (the correlation routine only gives one displacement vector per interrogation window). However, the methodology employed by PIV results in an evenly spaced grid of velocity vectors, which makes subsequent analysis of velocimetric data more straightforward. For example, it is easier to calculate velocity gradients (or the components of the velocity gradient tensor $\nabla\vec{v}$) within a fluid due to the even spacing between points at which velocity is measured.

Given the recent developments in PIV and other velocimetric techniques, there are a large number of recently published papers which have used different velocimetric techniques in conjunction with rheometry to observe flow inhomogeneities in rheometric test configurations. Gibaud's work in 2008[19] and 2009[20] used ultrasonic speckle velocimetry (USV) to study the evolution of velocity profiles of laponite dispersions undergoing shear in a Couette cell. Like waxy crude oils, Laponite is a synthetic clay which is comprised of disc shaped particles of thickness ~1nm and diameter ~30nm

[33]. Like waxy crude oils, laponite dispersions exhibits a strong transition from solid like behavior to fluid like behavior when the applied stress exceeds the yield stress for the material. Laponite dispersions also exhibits thixotropic behavior upon shearing - this thixotropic behavior is demonstrated by Gibaud by showing a decrease in the stress over time as a steady shear rate is being imposed on the sample. By using USV, Gibaud et. al. were able to demonstrate that during these steady shear rate experiments, the velocity profile of the laponite dispersion within the couette cell alternated between laminar flow profiles characteristic of steady viscous flow and plug-like flow profiles characteristic of interfacial slip. This type of behavior is shown in Figure 2-11(a).

The authors observed less plug-like flow profiles observed over time, and inferred from this observation that over time large unyielded pieces of laponite break down into smaller pieces due to erosion caused by the surrounding fluid. The progressive change in observed flow profiles is quantified through the use of a dimensionless flow type parameter Φ. The parameter Φ is simply the fraction of plug-like velocity profiles observed to linear like velocity profiles observed, within a 50 second time frame. Hence, large values of Φ indicate many observations of plug-like flow profiles, which indicate more solid fragments and less erosion. Gibaud's plot of Φ as a function of time is shown in 2-11(b). In addition to this work, Gibaud also shows that this plug-like behavior is only present when the material is sheared within the confines of a smooth geometry. When the material is sheared and in contact with a roughened Couette cell surface, shear localization is observed but no wall slip occurs. In the laponite dispersion studied by Gibaud, this shear localization manifests itself as a velocity profile showing a region near the static surface (inner Couette wall) which is exhibiting a high shear rate. On the other hand there is a region near the outer surface which exhibits a low, or close to zero shear rate.

Another spatially-resolved velocimetric technique which has been utilized in the study of yield stress fluids is MRI velocimetry, which was employed by Coussot et. al. to study the yielding behavior of carbopol gels [11]. For their experiments, Coussot and coauthors used a Couette cell geometry to impose a nonuniform shear rate in

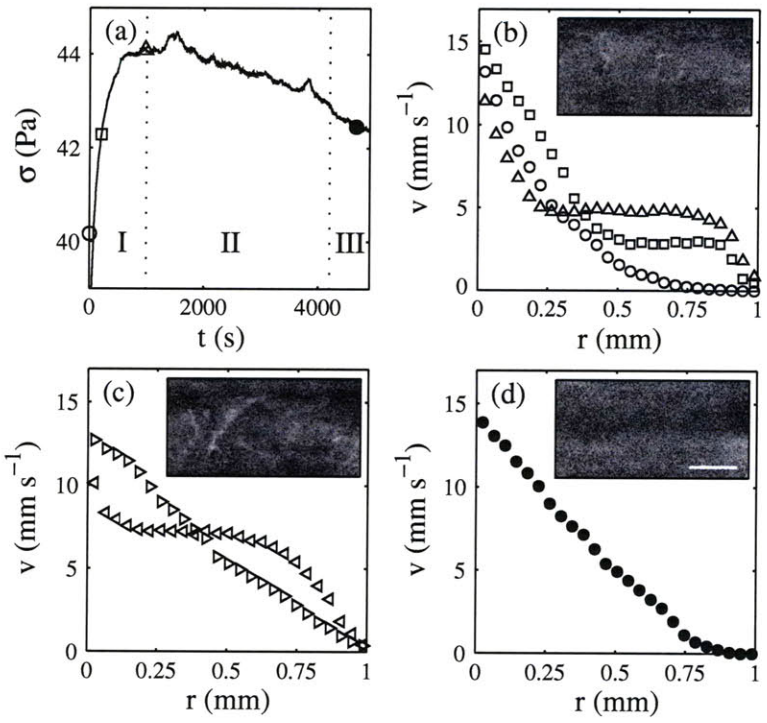

(a) Types of velocity profiles observed for a laponite dispersion under steady shear from Gibaud et. al. [19]. Subwindow (a) is representative of profiles observed in regime I, (b) of regime II and (c) of regime 3.

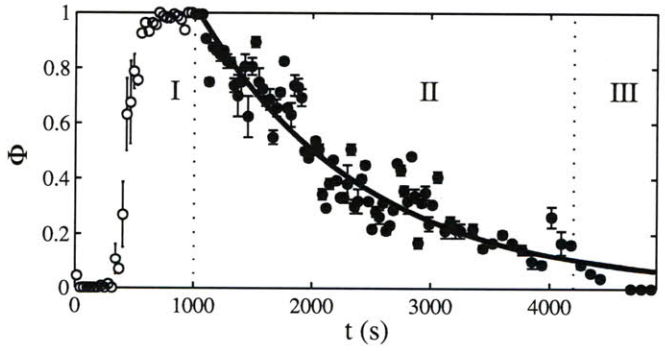

(b) Plot of Φ parameter vs. time for the laponite dispersion undergoing steady shear

Figure 2-11: Data from Gibaud et. al. [19] showing the evolution of the structure of instantaneous velocity profiles for a laponite dispersion undergoing steady shear in a Couette cell geometry. Gibaud and coauthors extract a parameter termed Φ from the data, which is indicative of the erosion of solid laponite fragments. The parameter Φ first rises as yielding begins and then decreases over time as the structure erodes.

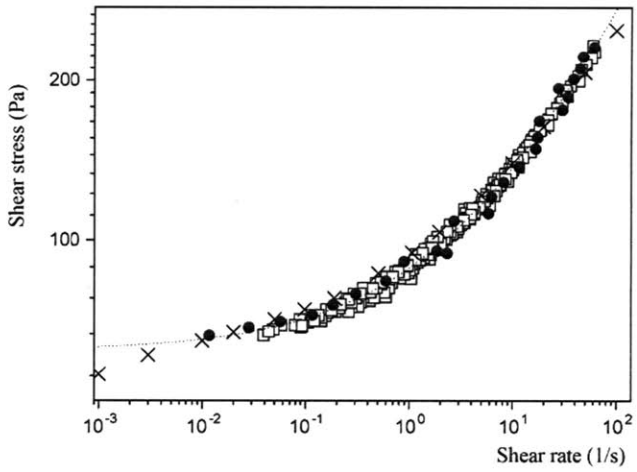

Figure 2-12: Stress vs. shear rate data for a carbopol gel (a hair gel). The data was obtained using 3 different experimental techniques - using a cone-and-plate rheometer, using a Couette cell rheometer, and inferring the stress-strain rate data from the velocimetric measurements. The data was inferred from velocimetric measurements by observing the local velocity gradient at a given point in the gap and then plotting that against the stress at that point (which is determined from the torque applied on the Couette geometry). Dotted line represents fit of this data to the Herschel-Bulkley model

a carbopol gel. By comparing both bulk rheological measurements, and localized velocity data within the Couette cell gap, the authors obtain a flow curve (shear stress vs. shear rate) that is well-represented by a simple Herschel-Bulkley constitutive equation. This data is shown in Figure 2-12 and the Herschel-Bulkley constitutive equation is given in Equation 2.5. One interesting aspect of this work is that wall slip could be prevented entirely from occurring - this was achieved by using roughened solid surfaces (sandpaper with "equivalent roughness" 200μm).

$$\tau = \tau_0 + k\dot{\gamma}^n \tag{2.5}$$

While the two examples mentioned thus far have used velocimetry to study systems which are similar to waxy crude oils (i.e. materials that possess a yield stress), the particular experimental techniques introduced in these papers are unlike those which are utilized in the present thesis. Both the papers by Gibaud and Coussot observed flow in inhomogenous shear fields, due to the use of the Couette cell geometry.

Specifically, the size of the gap used in these two experiments was not negligible compared to the radius of the inner rotating cylinders. For example, in Coussot's work, the inner and outer diameters of the Couette cell were 4.15 and 6 cm respectively. This means that under steady conditions, there is a variation in the shear stress of approximately a factor of 2 across the gap (due to the $\frac{1}{r^2}$ dependence in the shear stress).

Because the work encompassed in this thesis deals with imaging of uniform shear flow in a cone-and-plate rheometer, it is helpful to understand recent developments in imaging flow of non-Newtonian fluids under homogenous shear. Homogenous shear can typically be achieved through the use of a cone and plate geometry, or a thin gap Couette cell geometry, and it implies that there are negligible variations in the shear stress across the gap. The work by Tapadia et. al. [42] [43] utilized particle tracking velocimetry to study shear of entangled polymer melts in a cone-plate configuration, under steady shear and oscillatory shearing deformation. While the experimental setup employed by Tapadia et. al. is identical to what would be required of a PIV system, the image analysis carried out by the authors is different. In particular, all of the velocimetric data obtained by Tapadia is done in the single-particle limit, in which the displacement of individual particles is tracked instead of groups of particles within an interrogation window of the image. Tapadia et. al. use the measurement of the velocity of individual particles to show the result of banding in an entangled polybutadiene polymer solution. Figure 2-13 shows a figure from the paper by Tapadia where shear banding was demonstrated for an entangled polybutadiene melt. An interesting issue with the results shown by Tapadia and coauthors is that they are are inconsistent with the results published by Hayes in 2008 [23]. Specifically, the results from Hayes and coauthors do not show banding occurring in a polymer melt at a similar level of entanglement to that used by Tapadia et. al.. Furthermore, the results from [42] conflict with predictions made by the modified Doi-Edwards theory which do not predict shear banding in entangled polymer melts [24] [1].

Meeker and coauthors [31] use an experimental setup similar to that described by Tapadia et. al., however the fluids studied by Meeker are a dispersion of silicone oil

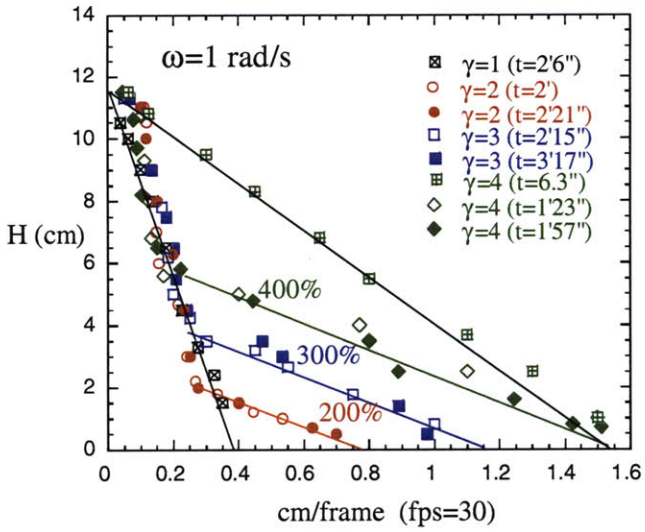

Figure 2-13: Velocity profiles for an entangled polymer melt undergoing oscillatory shear in a cone-plate rheometer (reproduced from paper by Tapadia et. al. [42]). Banding is clearly observed.

in water (an emulsion) and a paste of microgel particles. these authors discuss the experimental issues associated with their imaging system in more detail than Tapadia and Wang. Specifically, the authors mention how a transparent film is placed around the meniscus formed by the fluid at the edge of the cone plate geometry (this is shown in 2-14. The film is used in order to both prevent evaporation of the sample, as well as to prevent distortion of the images of the particles which would result from refraction of light when passing through an irregularly-shaped meniscus. Tapadia's experimental setup employs the same the bounding transparent film which Meeker uses, and in both cases the shear stress experienced by the fluid must be corrected for due to edge effects created by this bounding film. Meeker et. al. further note that it is important to place the imaging plane well within the sample, so that measurements of particle movement are not prone to edge effects created by this film (Meeker and coauthors observed this effect for values of r/r_{max} between 1 and 0.8). The use of flow visualization allows Meeker et. al. to determine how slip velocity depends on the imposed shear stress (i.e. the slip constitutive model). Furthermore, the measurements of slip velocity are used to verify the predictions made by Yoshimura and Prud'Homme[51] concerning the use of gap dependent rheology to determine slip

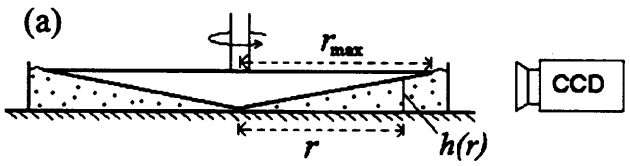

Figure 2-14: Experimental setup employed by Meeker to evaluate velocity profiles for emulsions and pastes of microgel particles.

Table 2.1: Survey of velocimetric measurement techniques used in recent studies of complex fluid rheology

Paper	Velocimetric Technique	Material
P. Coussot [11]	MRI Velocimetry	Carbopol Gel
T. Gibaud [19]	Ultrasonic Speckle Velocimetry (USV)	Laponite Dispersion
P. Ballesta [3]	Confocal Microscopy	PMMA Polydisperse Colloids
P. Tapadia [42]	Particle Tracking Velocimetry (PTV)	Entangled Polymer Solutions
S. P. Meeker [31]	Particle Tracking Velocimetry (PTV)	Pastes of Microgel Particles

velocity and bulk shear rate.

The studies by Meeker et. al. and Tapadia et. al. both use particle tracking velocimetry (PTV) to observe the displacement of seed particles, rather than PIV. As mentioned previously, one of the drawbacks of this method is that it is more difficult to obtain an evenly-spaced, full field grid of velocity vectors from the raw images obtained. Thus, there is a lack of an extensive discussion from these authors about the precision of their velocity measurements. A useful extension to their work would include looking at the statistical distribution of a large number of velocity measurements taken at a given gap height. This is something that can be achieved with the use of a digital imaging/PIV system. A digital PIV system would also be able to calculate local velocity gradients, and explore erosion of the structure of a yield stress fluid, like the laponite dispersions studied by Gibaud.

Chapter 3

Experimental Methods

3.1 The Model Wax-Oil System

3.1.1 Components

The model fluid that was used in this thesis consisted of two components. The first component is a mineral oil (Both a light and heavy version were used, Sigma Aldrich 330779 and 330760 respectively), while the second component is a paraffin wax (Sigma Aldrich 327212) with a melting point specified by the manufacturer between 58°C and 62°C. The light and heavy mineral oils differed by their density. The heavy oil has a higher density because it is composed of larger hydrocarbons. The density and API gravity for both of these components is given in 3.1.1. API gravity can be related to density of oil, ρ_{oil}, through the following formula [15] :

$$\text{API gravity} = \frac{141.5\rho_{\text{water}}}{\rho_{\text{oil}}} - 131.5 \tag{3.1}$$

In addition to this, the chemical composition of the mineral oil and wax was examined through the use of Gas Chromatography, or GC. Figure 3-1 shows the carbon number distribution of n-paraffins for the light mineral oil and the wax. As expected, the wax contains a higher weight percentage of larger n-paraffins. In addition to this, the wax contained only about 60 wt.% n-paraffins while the rest were iso- and cyclo-paraffins.

Oil	Density [kg/m^3]	°API Gravity
Heavy Oil (SA330779)	862	32.7
Light Oil (SA330760)	838	37.4

Table 3.1: Density and API gravity of light and heavy mineral oils. API gravity can be determined through the standard protocol ASTM D287 - 92 [15]. The equation for API gravity in terms of density is given in equation 3.1.

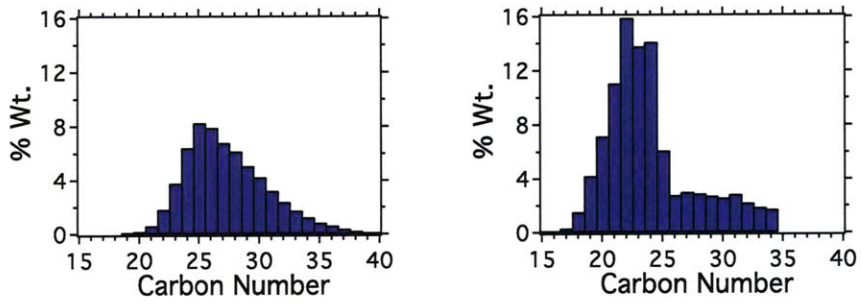

Figure 3-1: Gas chromatography data showing the wt.% distribution of n-paraffin carbon number for the mineral oil (right plot) and paraffin wax (left plot). The wax has a higher per-weight percentage of larger n-paraffins.

The two components are combined into a mixture with varying proportions of mineral oil and wax in order to mimic the key components of a waxy crude oil. The non-polar nature of both the mineral oil and the wax allows small amounts of wax to remain as a solute in the mineral oil. The amount of wax which remains in a solute form, and has not yet precipitated out of the solution, depends on the temperature of the fluid. The strong effect that temperature has on these precipitates, as well as the resulting rheological behavior, is discussed in detail in Section 3.1.2

3.1.2 Thermorheological Behavior of Model System

All of the rheological measurements that were carried out for this work were performed using one of two rheometers available in the lab - an AR-G2 stress controlled rheometer, and an ARES strain rate controlled rheometer. A cone-plate geometry was used in most experiments (except for a certain few where specified otherwise) in order to ensure a uniform imposed strain field throughout the bulk of the sample. In both rheometers temperature control is achieved by using a bottom Peltier plate.

An important component of the work done in this thesis was to first understand the basic thermorheological behavior of the combined model wax-oil system. However, before probing the temperature dependent rheology of the combined wax-oil system, it was necessary to understand how the viscosity of the wax and mineral oil depend on temperature individually. In order to do this, the viscosity of both of the components were measured as a function of their temperature (at a given shear stress, $\sigma = 0.28$Pa). The Newtonian mineral oil exhibits a increase in viscosity as temperature is decreased as shown in Figure 3-2. This behavior can be modeled through the use of a simple Arrhenius equation, as shown in equation 3.2.

$$\eta = \eta_0 e^{\frac{\Delta H}{R}\left(\frac{1}{T}-\frac{1}{T_0}\right)} \tag{3.2}$$

In Equation 3.2, T_0 is a reference temperature for the oil while η_0 is the viscosity of the oil at that temperature. Equation 3.2 can be written in an alternative form which contains only one term in the exponent:

$$\eta = \eta_1 e^{\frac{\Delta H}{RT}} \tag{3.3}$$

Where $\eta_1 = \eta_0 e^{-\frac{\Delta H}{RT_0}}$. The form of equation 3.3 is useful in illustrating the fact that the Arrhenius model is a two-parameter model for viscosity - these parameters are $\frac{\Delta H}{R}$ and η_1. While the Arrhenius relation can be used to describe the dependence of viscosity on temperature for the mineral oil, the wax requires a fit of a different functional form. The wax exhibits a sharp increase in viscosity as it approaches its melting temperature; it does not solidify immediately but rather exhibits a continuous (rapid) change in viscosity as the temperature drops by few degrees. This is due to the fact that the wax consists of a range of n-paraffin components, which tend to crystallize at different temperatures. As a result of this more complex behavior, the viscosity temperature relation of the wax is modeled using a VFT (Vogel-Fulcher-Tammann) fit, as given by Larson [28]:

$$\eta = \eta_{0V} e^{\frac{B}{T-T_\infty}} \tag{3.4}$$

The VFT equation is typically used to model the dependence of viscosity on temperature for glassy materials - it has 3 fitting parameters - these are η_{0V}, B and T_∞. The η_{0V} parameter determines the viscosity of the material at high temperatures, while the T_∞ describes a critical temperature at which the viscosity tends to infinity. The B parameter, on the other hand, determines how fast this increase in viscosity occurs as the temperature is lowered. Larson states that it is usually valid for temperatures as high as 50°C above T_g, which is the glass transition temperature. However, it can be shown that at high temperatures, the behavior given by VFT fit approaches the same behavior which would be given from an Arrhenius fit. In order to do this it is instructive to re-write Equation 3.4 in the following form:

$$\eta = \eta_{0V} e^{\frac{B}{T}\left(1-\frac{T_\infty}{T}\right)^{-1}} \tag{3.5}$$

The $\left(1-\frac{T_\infty}{T}\right)^{-1}$ term in the exponent can actually be expressed using a series expansion. We are interested in expanding this function far above the critical temperature $\frac{T}{T_\infty} \gg 1$ in which case we can expand the term $\left(1-\frac{T_\infty}{T}\right)^{-1}$ using a Taylor series about $\frac{T_\infty}{T} = 0$:

$$\left(1-\frac{T_\infty}{T}\right)^{-1} = 1 + \frac{T_\infty}{T} + \left(\frac{T_\infty}{T}\right)^2 + \left(\frac{T_\infty}{T}\right)^3 + \cdots \tag{3.6}$$

This expanded term can then then be substituted into 3.5 to obtain an expansion of the VFT equation about $\frac{T_\infty}{T} = 0$.

$$\eta = \eta_{0V} e^{\frac{B}{T}\left(1+\frac{T_\infty}{T}+\left(\frac{T_\infty}{T}\right)^2+\cdots\right)} \tag{3.7}$$

For values of $\frac{T_\infty}{T} \ll 1$, the higher order terms in the exponent in equation 3.7 can be neglected. This leaves a viscosity-temperature relationship which is approximately described by the Arrhenius form of equation 3.3, with the parameter equivalencies of $B = \frac{\Delta H}{R}$ and $\eta_{0V} = \eta_1$. A plot of the Arrhenius equation for $\log \eta$ vs $1/T$ results in a straight line, so for large values of T the VFT equation should approach a straight line on such a plot. This can be seen in Figure 3-3, where the equation in 3.7 is plotted with inclusion of up to third order terms.

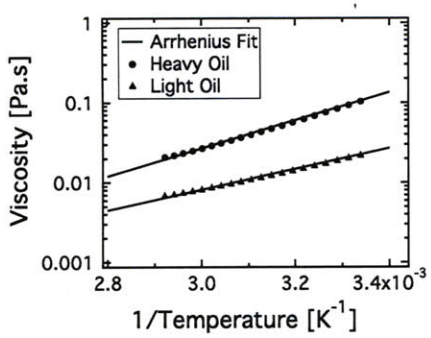

(a) Temperature dependence of the viscosity for the light and heavy mineral oils

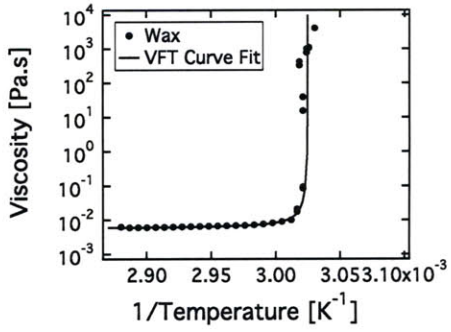

(b) Temperature dependence of the viscosity for the wax

Figure 3-2: Temperature dependence of the viscosity for (a) the two mineral oils and (b) for the pure wax. The fitted value of the Arrhenius parameter, $\frac{\Delta H}{R}$ for the light and heavy oils is 2890 and 3970 K respectively. For the wax VFT fit, $B = 0.5$K, $T_\infty = 330.4$K, and $\eta_{0V} = 0.0056$Pa.s.

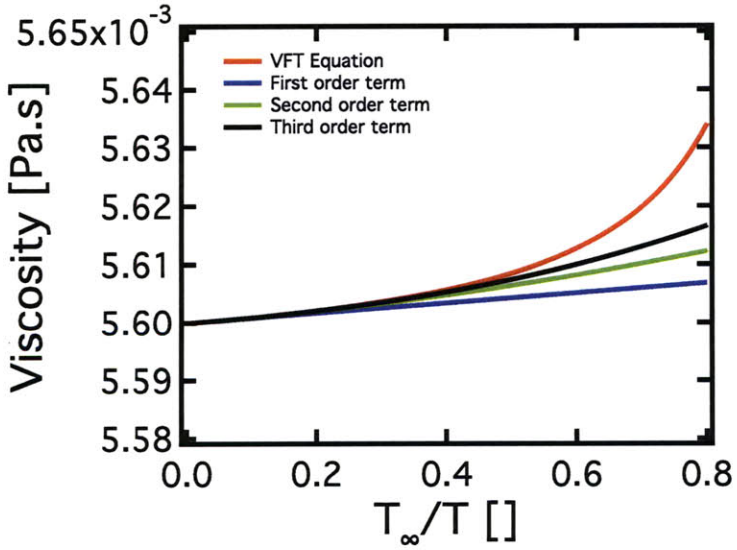

Figure 3-3: Expansion of VFT equation (3.4), up to first, second and third order terms. For values of $\frac{T_\infty}{T} \ll 1$ the behavior of the VFT curve approaches the Arrhenius relationship, which is that given by the first order expansion. The parameters used for the particular VFT curve are the same as those used to describe the wax behavior in Figure 3-2(b)

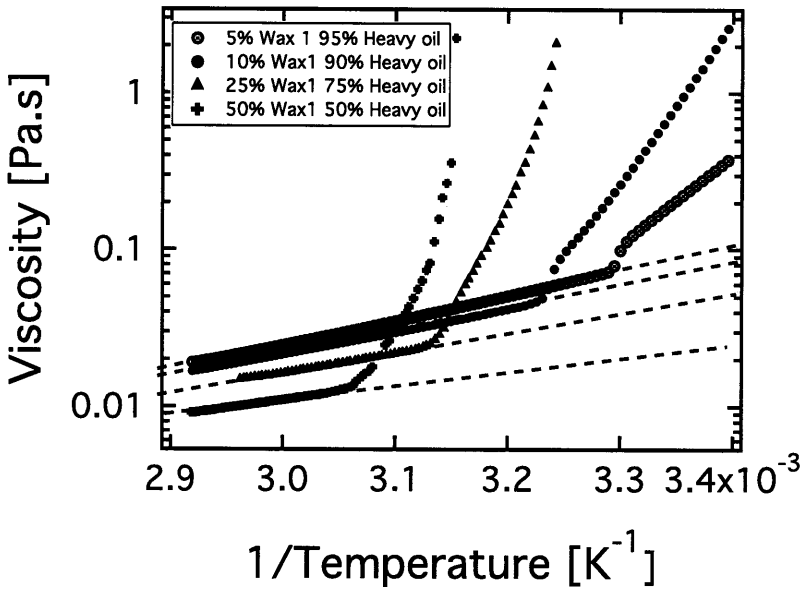

Figure 3-4: Temperature dependence of viscosity for a range of wax-oil mixtures. Straight dashed lines are Arrhenius Fits, with parameters given in Table 3.1.2.

The combined model wax-oil system consists of both the mineral oil and wax components. Thus, one would naturally expect the model wax-oil system to exhibit thermorheological behavior which lies somewhere between the mineral oil and the wax. The dependence of viscosity on temperature for a range of wax-oil systems is shown in Figure 3-4.

As can be seen from this data, the viscosity of these mixtures follows an Arrhenius like behavior for temperatures below a certain value, and above this critical value their viscosity increases at a rate much quicker than that predicted by the Arrhenius relation (but a slower rate than that predicted by the VFT equation for the pure wax). The temperature at which this change in behavior occurs is called the wax appearance temperature, T_{wa} (first discussed in section 2.1). The wax appearance temperature indicates the conditions at which wax precipitates first begin to form in the wax-oil system and also indicates the onset of non-Newtonian behavior in the fluid. The wax appearance temperature, T_{wa}, can also be determined using several different test protocols, which are discussed in more detail in appendix A.1. Table 3.1.2 gives the value of T_{wa} for a variety of wax-oil systems, as well as the values of

	T_{wa} [K]	η_0 [Pa.s]	$\frac{\Delta H}{R}$ [K]
Heavy Oil	N/A	0.027	3970
5% Wax	303.5	0.025	3656
10% Wax	309	.024	3313
25% Wax	321	.020	2882
50% Wax	326	.011	2381

Table 3.2: Parameters for various wax-oil mixtures. For the Arrhenius fit in each case, T_0 is taken as 60°C.

the Arrhenius fit parameters, η_0 and $\frac{\Delta H}{R}$.

The resulting non-newtonian behavior exhibited by these fluids below T_{wa} is due to the appearance and growth of the wax precipitates and the interactions between the individual crystallites. It is possible to directly observe these precipitates in a model wax-oil system by placing a sample which is initially above T_{wa} between glass slides which are located between crossed polarizing filters. The sample is then cooled to below T_{wa} and then illuminated using monochromatic light under a microscope.Figure 3-5 shows an image taken using such a setup. The wax precipitates can be seen as bright rod or needle shaped spots in Figure 3-5. These needle like shapes become larger for systems with higher wax content - as can be seen from figure 3-5, the needles have a characteristic length $\ell \sim 100\mu$m for a 10% system and $\ell \sim 10\mu$m for a 5% system. Furthermore, the size of the needles is highly dependent on cooling rate. However, the shape and size of these precipitates is consistent with what has been observed previously in the literature for other model wax-oil systems [45]. The rod like structures have a rather high aspect ratio ($\sim$ 10) and as a result, interactions between the wax precipitates can occur even at low volume fractions of total wax precipitated (this is because their effective volume is very high). These interactions result in a structure which is similar to the type of "house of cards" structure used by Luckham to describe bentonite suspensions [30]. Luckham described how at high enough concentrations of bentonite, the platelet shaped particles of bentonite *flocculate* into a continuous gel-like structure. This flocculation is a result of Brownian motion arranging the particles into energetically favorable orientations. The behavior of the model wax-oil system is similar to this, in the sense that a similar

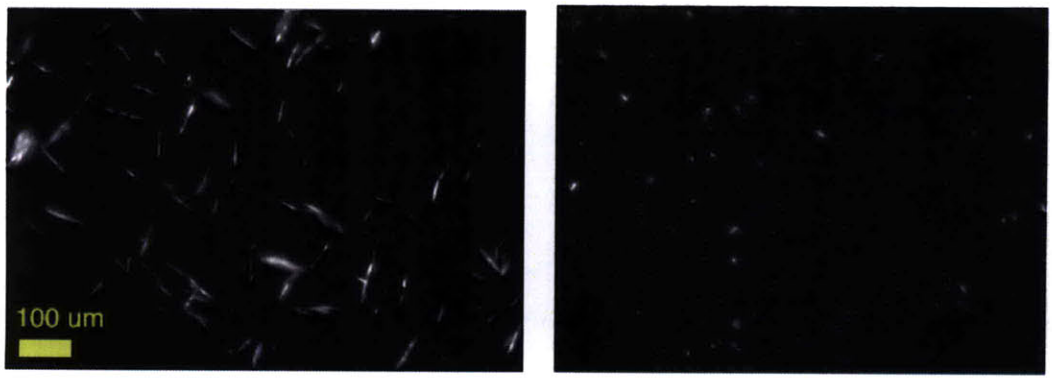

(a) 10% Wax-Oil System (b) 5% Wax-Oil System

Figure 3-5: Image showing the shape and size of wax crystallites formed in a 10% and 5% wax/heavy oil system at 25°C. Horizontal image scale is 100μm

kind of jammed gel structure forms when the sample is brought to below its wax appearance temperature. However, because the wax precipitates are large they are non-Brownian. So, it is the change in temperature which is responsible for the wax precipitates being able to grow and arrange themselves into a configuration where they can interact with each other. These interactions are then the reason why the viscosity-temperature dependence of the wax-oil mixture changes so suddenly at T_{wa} as shown in figure 3-4.

3.2 Velocimetric System for Flow Assurance Rheometry

3.2.1 Instrumentation, Design and Construction

In order to develop a better understanding of the rheological behavior of the wax-oil system below T_{wa} under imposed shear rate or imposed shear stress conditions, an experimental setup was constructed which allows for direct observation of the flow field within a sample undergoing shear in the rheometer. The main objective of the system was to be able to directly observe yielding mechanisms of the model wax oil system, such as those described by Lee [29]. The design of the system is similar

to those implemented by Tapadia and Wang to study flow of entangled polymer melts and Meeker et. al. for the study of soft pastes. In particular, the system works by extracting velocity measurements from displacement of seed particles which are dispersed within a sample undergoing shear in the rheometer. It differs from the schemes employed by Meeker and Tapadia by using a particle seed density high enough such that PIV is utilized instead of PTV. A schematic diagram for the setup is shown in Figure 3-7. The apparatus consists of a CCD camera (MatrixVision BlueFox) with a video zoom lens (Edmund Optics Techspec VZM 600i) that is positioned in front of the sample, such that the imaging plane of the lens/camera is located a few millimeters into the sample beyond the fluid meniscus. The upper (rotating) geometry of the rheometer is a 50 mm diameter quartz plate, which allows illumination of the sample using a collimated laser beam to form an imaging plane in the sample. The particular laser which is used is a focusable 10mW Edmund optics laser diode, with a frequency of 635nm. The sample is seeded with reflective titanium dioxide seed particles from TSI Inc. of average size $3\mu m$, allowing for the velocity profile across the rheometer gap to be measured. Furthermore, a raised Peltier configuration (TA instruments 531052) is utilized such that the lower heated plate is interchangeable - this allows for several different bottom geometries to be used, such as a cone or a flat plate. A photograph of the raised Peltier plate is shown in Figure 3-6(a), while one of the lower cone geometries which was designed for use with the raised Peltier system is shown in Figure 3-6(b).

One of the critical design parameters for the experimental setup was the choice of the VZM lens. The VZM lens which is used in the setup was chosen because it allows for a field of view from 6mm$\times$6mm to 1mm$\times$1mm (depending on the zoom level). Furthermore, at the highest level of zoom for the lens, which is at 6$\times$, the depth of field of the lens is only 20 μm - this prevents the camera from acquiring images which contain significant scattering from particles that are out of the plane of interest. The lens also has a large working distance - about 6cm - this allows the camera to view the plane of interest from a large distance with little distortion. Since the lens has a fixed working distance, focusing is achieved by placing the lens/camera combination on a

(a) Photograph of stepped Peltier plate

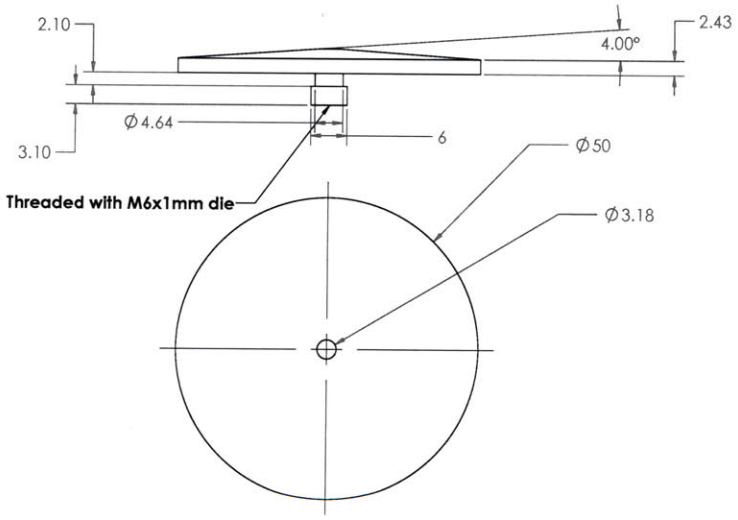

(b) Engineering diagram of lower cone attachment to stepped Peltier plate

Figure 3-6: Photograph of stepped Peltier plate, and engineering drawing of lower cone geometry used in experiments. The cone has a diameter of 50 millimeters and an angle of 4°. The truncation gap is 111μm. The bottom threaded section is M6×1 for compatibility with the stepped Peltier threaded hole. The cone was machined out of 6061 aluminum for a higher thermal conductivity and better thermal response time.

Lens Working Distance	60mm
Camera XYZ travel	25×25×40mm
Beam Path Length	~120mm (adjustable)
Lens Field of View	1×1 mm at 6× zoom
Lens Depth of Field	20μm at 6× zoom
Camera Resolution	640×480 pixels
Seed particles	Reflective titanium dioxide (3μm)

Table 3.3: Design Parameters of Imaging System

3 axis positioning stage which can move the camera into the appropriate position, and bring the image into focus. The seed particles employed were another important design parameter. The 3μm TiO_2 particles were used since they were of a relatively small size compared to the size of the imaging plane. The seeding density is typically $\sim$ 0.01% wt.. With the camera resolution of 640×480 pixels, each seed particle showed up as a spot of about 2-3 pixels in diameter. This allowed each image to have a sufficiently high seed density (usually 10 or more seed particles per interrogation window, as per the recommendations by Adrian [2]). The imaging system design parameters are summarized in Table 3.3.

As stated previously, the lens/camera assembly is placed on a 3 axis stage which allows for the location of the camera focal plane to be fine tuned to coincide with the plane of illumination created by the laser. The entire system is shown in Figure 3-7, both as a simplified schematic diagram in Figure 3-7(a), and as a solid model in Figure 3-7(b). This camera and stage assembly is then attached to an 8 × 4" optical breadboard which is in turn mounted onto an aluminum box frame as shown in Figure 3-7(b). The aluminum box frame is made from 1 inch profile 80/20 slotted aluminum. The laser and reflecting prism are also mounted onto the box frame, at a position above the lens/camera assembly. Specifically, the laser and prism are placed in line with each other on an aluminum square plate, which is attached to the front of the box frame. The laser and prism are oriented in an inverse configuration such that the beam travels along the bottom of the square plate, and when it impinges on the prism it is reflected down to the quartz geometery. In order to allow for fine tuning of the laser beam location, the reflective prism is mounted onto a prism holder (ThorLabs

kinematic prism mount KM100P), which has 2 adjustment knobs that can direct the beam to its desired location. Due to this particular configuration, it is possible to independently vary the location of the camera imaging plane and the location of the plane being illuminated by the laser.

The ensemble aluminum box frame, which consists of both the camera/lens assembly, and the laser/prism assembly, must then be mounted onto the same bench that the rheometer is located on. This is achieved by placing the box frame on bearings which can slide along a lower frame, which is also constructed from 1 inch profile 80/20 slotted aluminum. The lower frame is then clamped onto the table using G-clamps, or it slides along bearings which are themselves clamped to the table using G-clamps. The bearings allow for rough adjustments of the location of the imaging system to be made, while the 3-axis stage setup and the prism holder configuration allow for the user to finely tune location of the imaging plane.

The sequence of images obtained from the CCD camera is typically processed using PIV software (Digiflow from Dalziel Research partners - http://www.dalzielresearch.com/digiflow/) which applies a cross correlation scheme to the images (see section 2.3). This in turn provides a two-dimensional velocity vector field for each image obtained. The resolution of the digital images which are acquired using the CCD camera are 640×480 pixels, while the interrogation windows used by the cross correlation scheme are typically 16×16 pixels. As a result, the output from each image is a 40×30 grid of velocity vectors (or $n_1 \times n_2$). A typical raw image is shown in Figure 3-8(a), which is annotated to indicate the location of the top and bottom surfaces, as well as their relative movement. The image is overlaid with a vector field (green arrows) to indicated the grid of velocity vectors that is obtained with the cross correlation scheme. The 1-direction (x_1) is the direction of flow, with corresponding velocity v_1. The 2-direction (x_2) is the shear direction, or the direction along which there is a velocity gradient. Note from this image that the imposed shear rate for a linear velocity profile should be given by $\dot{\gamma} = \frac{dv_1}{dx_2}$.

The velocity vectors shown in Figure 3-8(a) are typically averaged over the direction of flow (the 1 direction). By carrying out this operation, the spatially averaged

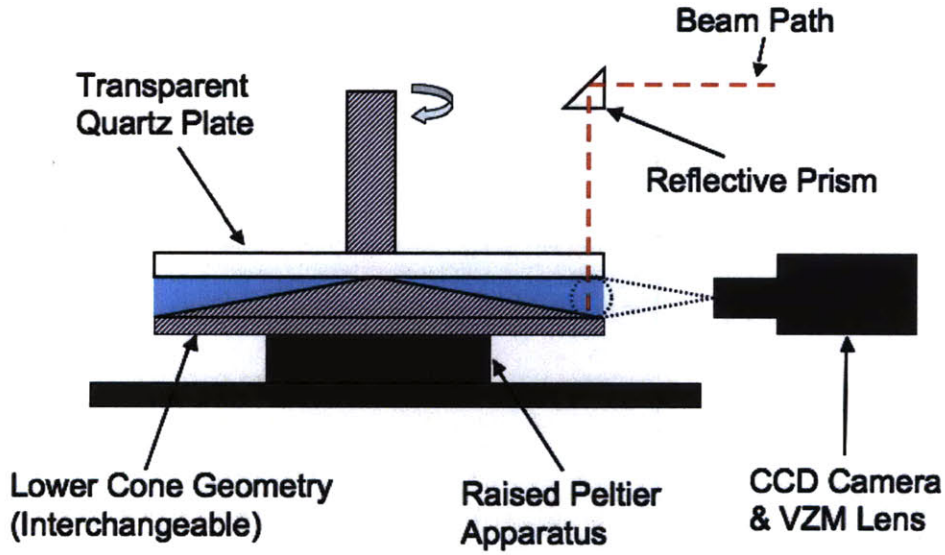

(a) Simplified schematic diagram of velocimetric measurement system

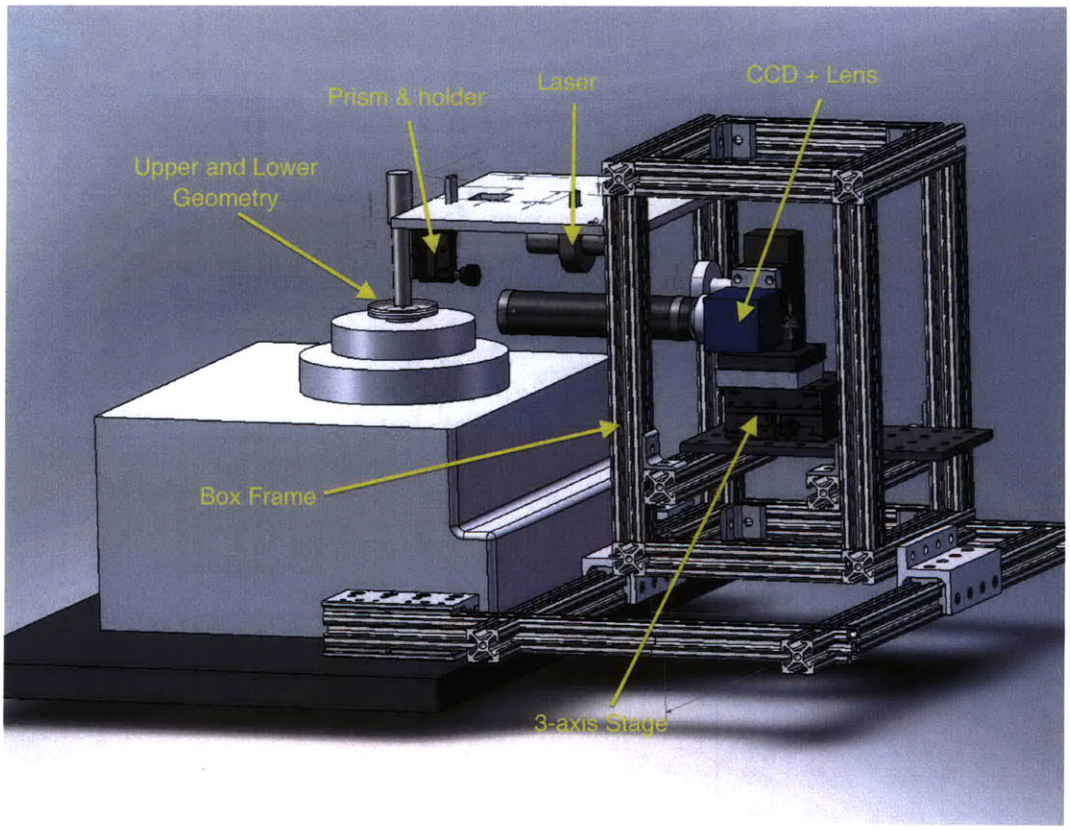

(b) Annotated solid model of velocimetric measurement system

Figure 3-7: Schematic diagram and solid model of velocimetric measurement system. For scale, height of box frame is 12 inches, with a width and length of 8 inches.

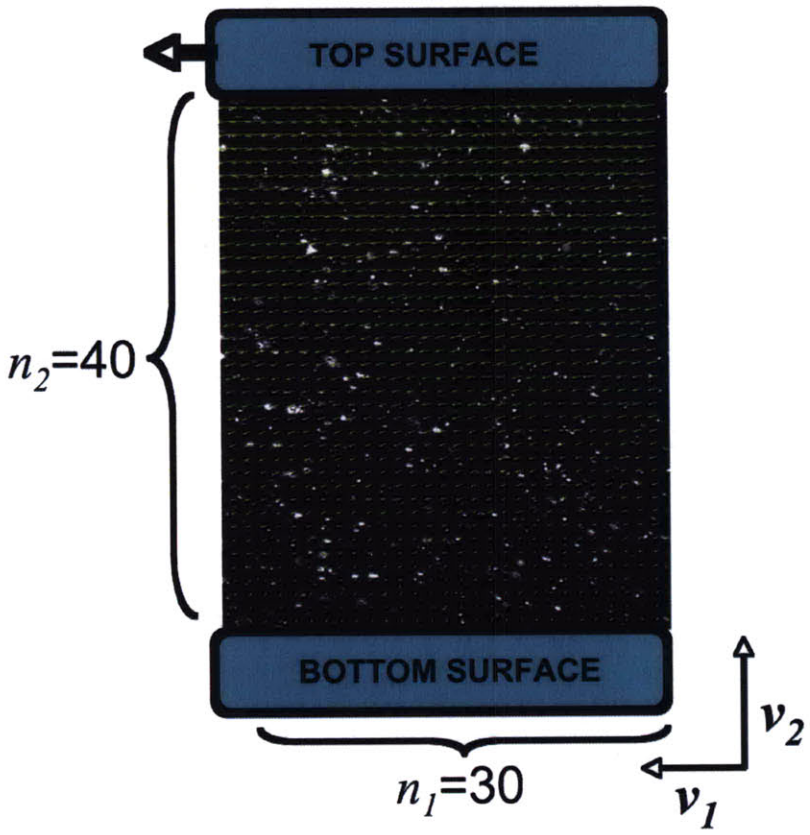

(a) Raw image with velocity vector overlay

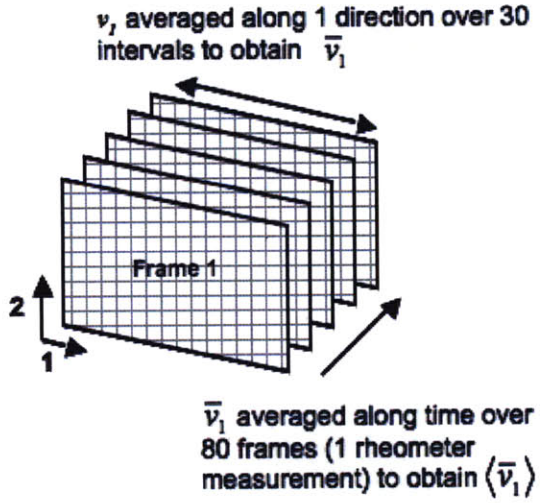

(b) Averaging scheme used to analyze data

Figure 3-8: Diagram showing orientation of 1 and 2 directions relative to fluid experiencing shear in the rheometer, as well as the number of velocity vectors in each direction (n_1 and n_2). Figure 3-8(b) shows how the velocity measurements can be averaged over both time (i.e. several frames) and the 1 direction in order to obtain a velocity profile over a number of frames n_f.

velocity $\bar{v}_1$ is obtained. This value of $\bar{v}_1$ can then be averaged over a number of frames (n_f), so that it is then possible to determine the spatially and time averaged velocity profile across the gap of the rheometer, given by the parameter $\langle \bar{v}_1 \rangle$. In order to demonstrate the accuracy of the setup, Figure 3-9 shows a comparison of a measured velocity profile with the expected profile imposed by the rheometer for the Newtonian mineral oil. The expected profile for a newtonian fluid is just given by the following:

$$v_1 = \dot{\gamma} x_2 \tag{3.8}$$

Figure 3-10(a) gives the probability distribution of velocity values over 180 frames and along the position $x_2 = 0.7$ mm from the bottom plate. As can be seen, the distribution can be fit to the Gaussian form, with a standard deviation, $\sigma_1 = 0.0187$ mm/s, which is 5% of the average velocity $\langle \bar{v}_1 \rangle$ value at that particular point. It is important to realize that the value σ_1 is the standard deviation of the velocity in the 1-direction only, while σ_2 is used to refer to standard deviation of v_2 values. Furthermore, it is only reasonable to compute a value of σ_1 at a particular point along the 2-direction. This is because there is a variation in the value of v_1 along the 2-direction, due to the nature of the simple shear flow which is being observed. The plot in Figure 3-10(b) shows how the value of σ_1 varies along the 2-direction. As can be seen from this plot, there is little variation in this value - this indicates that the sources of error in the PIV/image analysis are a constant. These errors can be attributed to a number of things - although in many cases errors are a result of vibrations in the imaging system.

It is also instructive to understand the limitations that the value of σ_1 imposes on the types of experiments which can be carried out with this experimental apparatus. These limitations are essentially set by an upper and lower bound of velocity which the system is actually capable of measuring. All practical considerations aside, the lower bound of velocity which can be measured is zero. This is because it is possible to increase the time spacing between successive frames to a very large value, so that even a very small velocity will result in a considerable displacement of a particle between

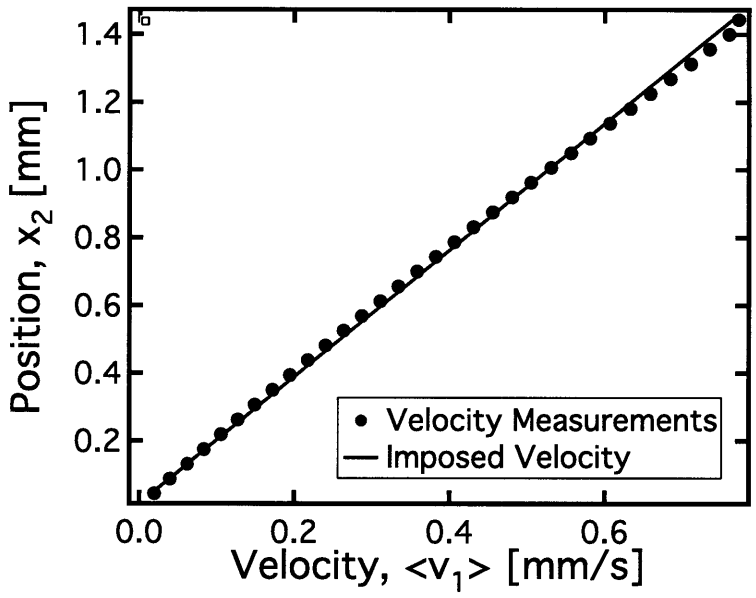

Figure 3-9: Velocity profile showing variation of $\langle \bar{v}_1 \rangle$ along the 2-direction for a 0.01% wt. seeded light mineral oil undergoing steady shear, $\dot{\gamma} = 0.535s^{-1}$.

two frames. However, there is a minimum displacement which the imaging system can register between successive frames, and this is determined by the measured value of σ_1. Given the time spacing between two frames, δt, the lower bound for measurable displacement between two frames is simply given by $(\delta t) \cdot (\sigma_1)$. For the particular value of σ_1 from Figure 3-10(a), with a δt of 0.02 seconds (given by the frame rate images were taken at), this minimum displacement is 0.37μm. This value is actually smaller than the camera resolution, which is 1μm/pixel.

3.2.2 Correcting Image Distortion

One important experimental artifact that presents itself when attempting to track particles behind the fluid meniscus (as shown in Figure 3-7) is a distortion of their position due to the effects of refraction at the curved free surface. If the location of the particles is to be known accurately, then this effect must be corrected for. Two schemes for correcting the effects of refraction are discussed in detail here.

The interface formed due to the shape of the air-fluid meniscus possesses curvature in two directions. One direction is along the circumference of the plate-plate or cone-

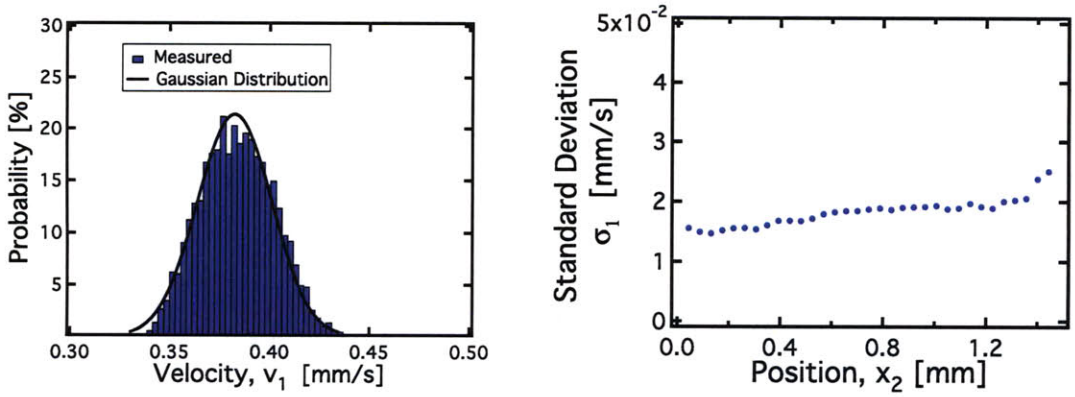

(a) Probability Distribution

(b) Standard Deviation

Figure 3-10: Distribution of velocity vectors at a position of 0.7 mm from the bottom plate, obtained from the data used in 3-9. Figure 3-10(b) shows the standard deviation of the velocity in the 1-direction (σ_1) as a function of position in the 2-direction. The data shows that this value is almost constant everywhere, with a slight increase in uncertainty near the upper plate at $x_2 = 1.3$mm.

plate geometry (ϑ). The other direction is along the gap height (or the 2 direction). It is possible to write the curvature of this meniscus, κ, as a function of two radii of curvature, as given in Equation 3.9.

$$\kappa = \frac{1}{R_i} + \frac{1}{R_\vartheta} \tag{3.9}$$

Since the gap height is much smaller than the circumference of the plate geometry, we have $R_i << R_\vartheta$ so as a result refraction is dominated by curvature of the meniscus in the 2 direction. If the fluid being tested in the rheometer has a contact angle of 90° with the top and bottom surface, then the curvature along this distance would be zero, and distortion due to refraction becomes negligible. However, the model wax-oil system is composed of non-polar hydrocarbons and therefore has a low contact angle ($\sim 10°$). As a result, the meniscus that is formed between the top and bottom surfaces has an axial curvature that is roughly circular. A photograph of the meniscus is shown on the left in Figure 3-11.

By assuming that the meniscus is approximately a circular shape, it is then possible to quantify the change in the observed position of particles which results from the refraction. The effect of the refraction in such a case is shown schematically on

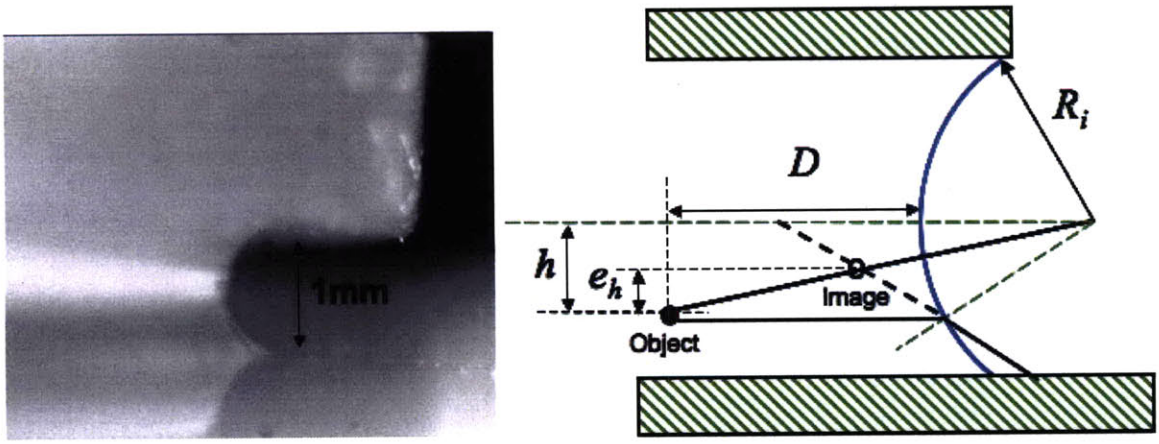

Figure 3-11: Photograph of the meniscus which is typically formed at the air fluid interface in the region between the rheometer plates. Diagram on the right shows the effect distortion has on the perceived location of the tracer particles

the right in Figure 3-11. If one neglects the effect of curvature along the circumference of the plate, then the only effect that the refraction has is to shift the observed location of the tracer particles towards the centerline of the meniscus (i.e., towards the position $x_2 = h/2$, where h is the gap height in the rheometer). This results in the observed gap appearing to be smaller than it actually is. The vertical distance between the observed and actual location of the observed particles is denoted as e_h in Figure 3-11, and it can be determined if the radius of curvature of the meniscus, R_i is given, as well as the distance D of the particle from the meniscus. The refractive indices of the two media must also be given (in this case for oil $n_o = 1.47$ and for air $n_a = 1$). From these parameters, it is possible to determine their relation to e_h. This relation is given in equation 3.10.

$$e_h = \frac{\left(\frac{D}{R_i} + \left[1 - \cos\left(sin^{-1}\frac{h}{R_i}\right)\right]\right)\frac{h}{R_i}}{\frac{D}{R_i} + 1 + \frac{h/R_i}{\tan\left(sin^{-1}\frac{n_o h}{n_a R_i} + sin^{-1}\frac{h}{R_i}\right)}} \tag{3.10}$$

In order to illustrate the effect that different values of R_i, h and D have on e_h, Figure 3-12 shows e_h plotted against h (the vertical distance of the tracer from the meniscus centerline) for different values of R_i and D. As can be seen from the figure, the further away a seed particle is from the centerline, the larger the value of the shift

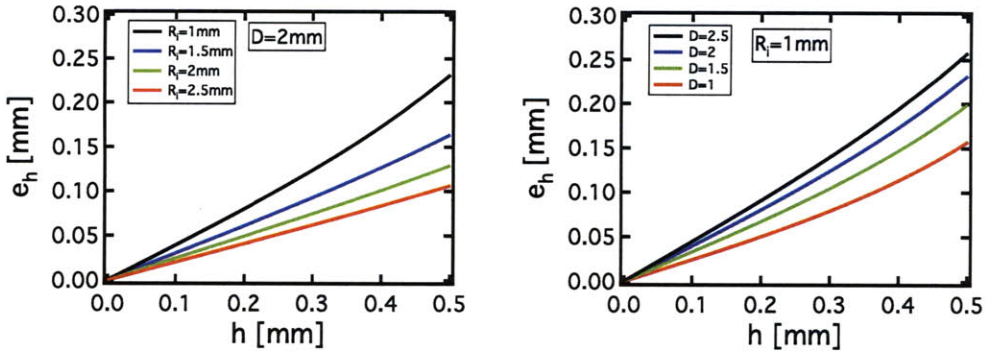

Figure 3-12: Effect of the parameters R_i and D on the distortion as measured by e_h.

e_h. Furthermore, the shift e_h is smaller for larger values of R_i, and smaller for smaller values of D. This suggests that it would be ideal to locate the camera's focal plane closer to the meniscus (have a low value of D) as well as impose a very large value of R_i.

One way to account for the effects of the distortion in the velocity measurements is to use equation 3.10 to determine the real location of particles, and then transform the coordinate axes of a plot such as Figure 3-9 to represent this distortion in the image. One of the drawbacks of this method, however, is that it becomes difficult to observe particles that are very close to the top and bottom walls.This is due to the fact that the value of e_h is very large for these tracer particles. As a result, it is not possible to determine what the velocity of the fluid is close to the solid surface. The ability to determine this velocity is of great importance in these experiments because it provides insight into whether or not there is slip occurring at the solid surfaces, and this is one of the primary reasons why the velocimetric measurement system is used in the first place.

A better methodology which allows one to avoid the effects of distortion altogether is to alter the shape of the fluid meniscus. This can actually be achieved by aligning the top geometry (which is the transparent 50mm quartz plate) with a bottom geometry which is of the same diameter. The stepped Peltier plate makes this possible by allowing interchangeable bottom geometries to be used. If the edges of the top and bottom geometry are aligned, then the fluid placed between the two plates can be

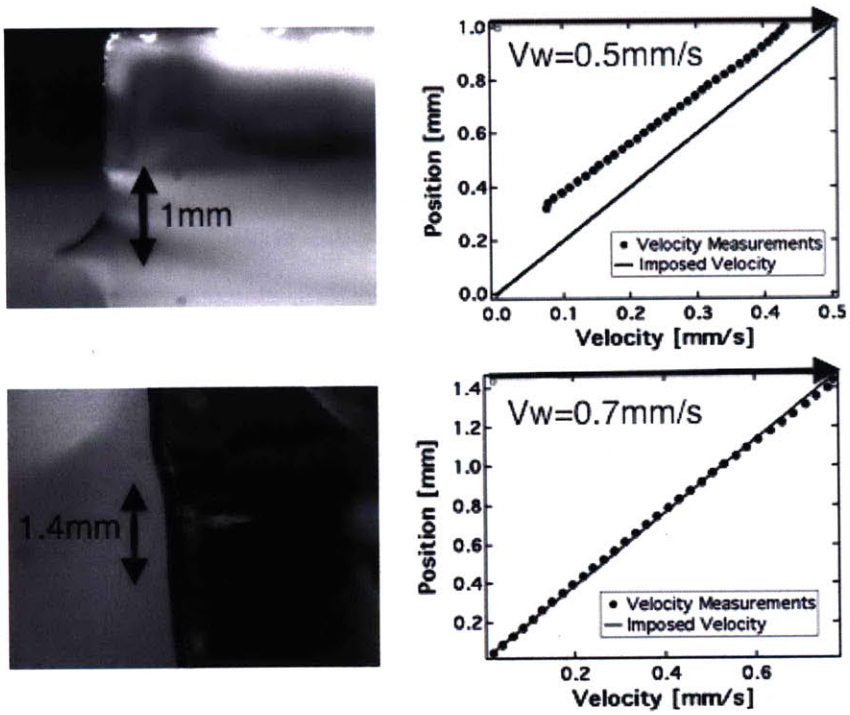

Figure 3-13: Flattening of meniscus shape and improvement in accuracy of velocity profile due to pinning of top and bottom of fluid. Fluid used is a Newtonian mineral oil at 25°C. In both the top and bottom plot of the velocity profile the imposed shear rate is $\dot{\gamma} = 0.5\text{s}^{-1}$, however in the top plot and image the gap height was set to a different value (1mm instead of 1.4mm). Velocity of top plates is annotated in the velocity profiles.

"squeezed out" to the edges of the geometry, becoming pinned at the top and bottom surface. If the gap height is set to the appropriate value, then the value of R_i can be effectively increased to infinity. The effects of distortion are then drastically reduced. The change in the meniscus shape as well as the subsequent improvement this has on the accuracy of the velocity profiles is shown in Figure 3-13

So far, in this chapter, the model wax-oil system has been introduced. The basic thermorheological behavior of the wax-oil system's components has been demonstrated and models have been used to describe the viscosity-temperature dependence of the model fluid constituents. The combined model wax-oil system has also been studied in brief - namely the wax appearance temperature was determined for a number of model systems with varying quantities of wax. In addition to this, the principles of operation of the velocimetric system have been described. In the following chapter,

the rheological behavior of the model wax-oil system will be studied in more detail, while the PIV system will be used in conjunction with rheological measurements to gain further insight into the behavior of the model wax-oil system.

Chapter 4

Results and Discussion

4.1 Yielding Behavior of Model Wax-Oil

4.1.1 Bulk Rheological Behavior

The purpose of developing the particular model wax-oil system described in Chapter 3 was so that the system would accurately represent the rheological behavior of a real waxy crude oil. One defining characteristic of actual waxy crude oils is the existence of a yield stress below the wax appearance temperature [47]. The model wax-oil system described above does in fact exhibit a yield stress, as shown by Figure 4-1. Care was taken in obtaining the data in Figure 4-1 - the gel strength of waxy crude oils such as the one studied by Visintin [47] have been shown to be very sensitive to variations in mechanical and thermal history. It was therefore reasonable to expect that the model wax-oil system would exhibit a similar kind of behavior. Thus, in order to minimize variability in the strength of the gelled system due to cooling rate differences, all systems were presheared at a temperature 20°C higher than T_{wa} and then cooled at a rate of 1°C/min to the test temperature. A subsequent "holding time" of 10mins was then applied. The 10 minute holding time (in which the temperature is held constant and shear rate is kept at zero) was applied to ensure that any temperature gradients within the fluid diffuse, while any aging of the gel structure has ceased. This particular sequence of steps is akin to the "thermal beneficiation" procedures

described by Pedersen [35].

The data in Figure 4-1 shows the dependence of viscosity on applied shear stress, for a 10% and 5% wax-oil system at a range of temperatures below T_{wa}. It is apparent that there exists a critical stress (or range of stress values) over which the viscosity of the fluid drops suddenly by several orders of magnitudes. This stress increases with decreasing temperature, and the drop in viscosity becomes more sudden at lower temperatures. The behavior of the wax-oil systems can be fit to the Cross model, which is given in equation 4.1

$$\eta = \eta_\infty + \frac{\eta_0 - \eta_\infty}{1 + (C\dot{\gamma})^m} \tag{4.1}$$

In addition to this, the yield stress, σ_y can be tabulated as a function of temperature for the 10% and 5% systems. The values of σ_y are given below:

Temperature [°C]	5% Wax-oil σ_y [Pa]	10% Wax-oil σ_y [Pa]
23	4	560
27	0.2	260
29	0.1	80
32	N/A	10

Table 4.1: Values of the yield stress, σ_y, for the 5% and 10% model wax-oil system at a range of temperatures.

It is important to realize that the data shown in Figure 4-1 is representative of the behavior within the bulk of the sample, and does not hinge on any type of slip interaction which may be occurring between the fluid and the solid surface of the cone-plate geometry. The no slip condition (which often does not hold for this particular type of fluid) was ensured by using a roughened cone-plate geometry. By directly observing the flow field using the velocimetric system, it was possible to show that this roughened geometry consistently prevented slip from occurring. The effect of surface roughness on the rheology of the fluid is discussed in more detail in section 4.3

Another important aspect of this yielding behavior is that it is an irreversible transition. The irreversibility inherent in the material can be demonstrated by measuring

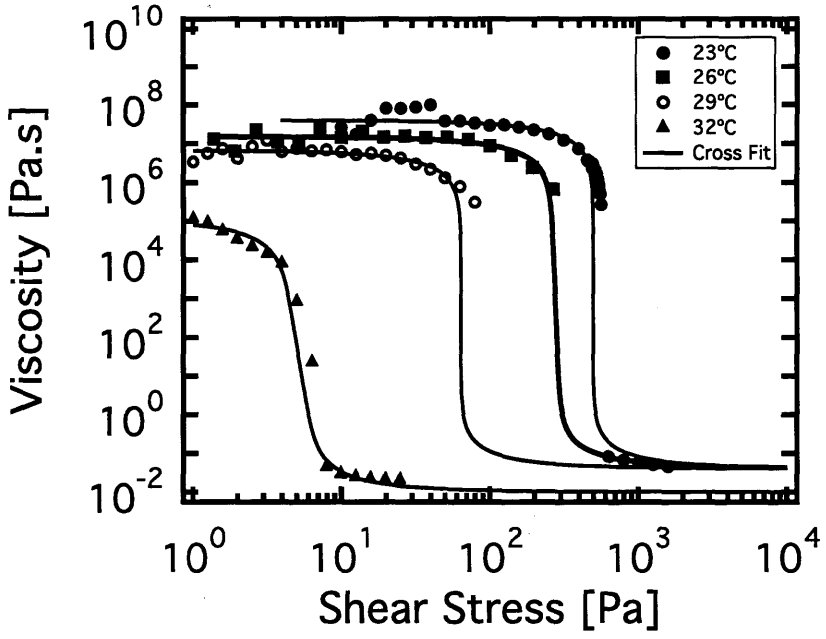

(a) The 10% Wax-oil System

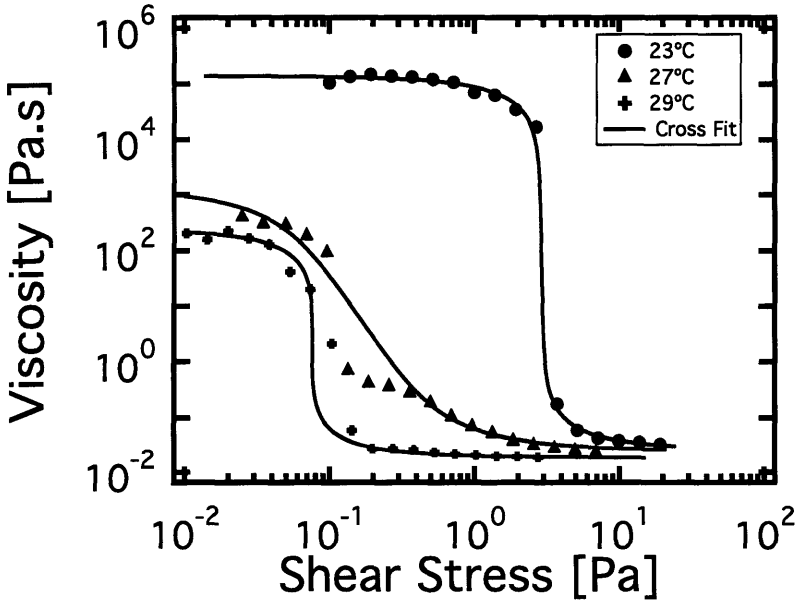

(b) The 5% Wax-Oil System

Figure 4-1: Flow curves for 10% and 5% wax-oil system at a range of temperatures below T_{wa}. For each sequence of viscosity measurements at a given temperature, the wax-oil system was treated with a 1°C/min thermal beneficiation step where it was brought from 20° above T_{wa} to the test temperature. In order to measure viscosity, a creep test is carried out (where a fixed stress is imposed) and the steady state viscosity is determined 5 minutes after the imposition of the stress. Each set of points is fit to the cross model for viscosity, which is given in equation 4.1

the viscosity of the sample at incrementally higher values of shear stress (starting from below the yield stress). Eventually, when the yield stress is exceeded, the viscosity of the material drops drastically. Then, if the imposed shear stress is lowered incrementally, the measured viscosity at a stress below the yield stress is observed to be lower than it was in the pre-yielded state. This type of behavior is illustrating in Figure 4-2. For the data shown in Figure 4-2, a 5% wax oil system was cooled to 23°C at a rate of 1°C/minute. A subsequent 10 minute holding time was then applied. Then, a series of stress steps was applied to the system, and the strain was measured over this period of time. The instantaneous viscosity of the sample is determined by computing the *strain rate* at each point in time, and then dividing the applied stress by this instantaneous strain rate.

The data in Figure 4-2 shows the 5% system undergoing a stress step of 0.7 Pa for the first 15 minutes, then a stress step of 7 Pa for the next 15 minutes. A third stress step of 0.7 Pa is then applied for the next hour of the test. These values of the stress were chosen by determining the yield stress for the 5% system at 23°C (this can be obtained from Figure 4-1). The 0.7 Pa stress is below the yield stress of the 5% system at 23°C. Thus, in Figure 4-2, during the first 15 minutes of the experiment the system is in its pre-yielded state. When the 7 Pa stress is applied, the system yields and the viscosity drops by several orders of magnitude, down to a value of ~0.05 Pa.s. During the third stress step, the viscosity increases again, however it does not increase to the same value that it held in the pre-yielded state. Furthermore, even though the viscosity is measured over a period of 1 hour, it does not show any considerable increase over this period of time. The viscosity appears to level out to a constant value. Thus, the yielding behavior of the wax oil system is irreversible.

This behavior is similar to "thixotropic loops" that have been observed for other systems in the literature, such as the bentonite suspensions studied by Moller [32]. Moller classifies the bentonite suspension as a "thixotropic yield stress fluid", and states that these systems exhibit an *aging* behavior whereby their viscosity increases over time if a stress below the yield stress is applied. Furthermore, these fluids exhibit *shear rejuvenation* whereby their viscosity can decrease over time when a

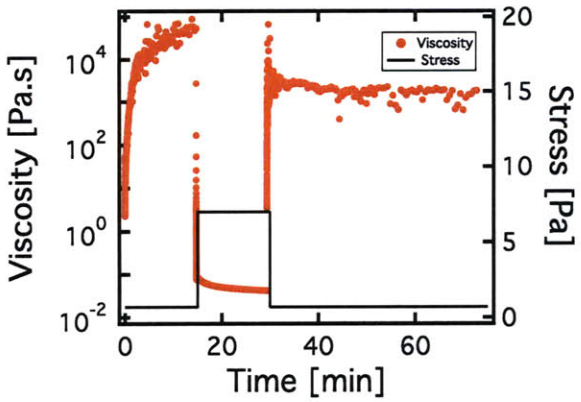

Figure 4-2: Viscosity vs. time plot for a 5% wax-oil system at 23°C. For the particular experiment, 3 stress steps are imposed: an initial step below the yield stress, a second step above it and a third step again below the yield stress. The viscosity does not exhibit an increase back to the pre-yielded value during the third step.

shear stress above the yield stress is applied. The model wax-oil system does exhibit shear rejuvenation - during the second stress step shown in Figure 4-2, the viscosity of the sample decreases over time. However, the model wax oil system lacks the aging behavior described by Moller - during the third stress step, there is no observed increase in the viscosity towards the pre-yielded value. Thus, the behavior of this particular material differs from a true thixotropic behavior because it does not age, and the microstructure does not rearrange itself into its pre-yielded state after waiting long periods of time. The only way to obtain the pre-yielded state again is by going through another process of thermal benficiation, whereby the material is heated up to above T_{wa}, and then cooled down again (at the prescribed cooling rate) so that the precipitates can reform into their pre-yielded arrangement.

The data in Figure 4-1 is obtained by imposing a steady stress and monitoring the strain of the sample over time. These type of tests are also referred to as creep tests. A representative set of creep curves for the 10% wax oil system is shown in Figure 4-3. In an ideal situation, these creep curves allows one to measure the steady state viscosity of the sample after a long period of time, when any initial transients of the material have died out. This is accomplished by determining the slope of the creep curve at a particular point in time. The slope of the creep curve is equal to the instantaneous shear rate of the system, and because the applied stress is known

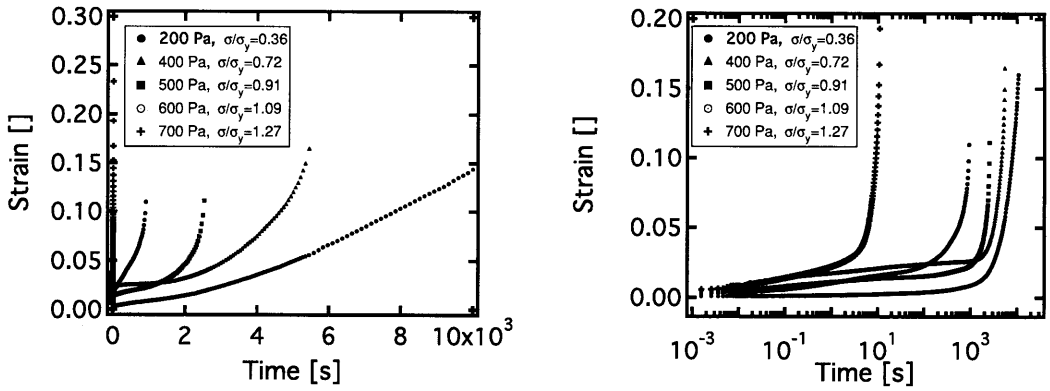

(a) Family of creep curves on a linear time scale (b) Family of creep curves on a logarithmic time scale

Figure 4-3: Family of creep curves for the 10% wax oil system thermally beneficiated to a temperature of 23°C. As can be seen, the material exhibits a sudden yielding behavior after long periods of time. For reference, the viscosity values in Figure 4-1 were obtained by measuring the slope of such curves at the 5 minute mark, and using that strain rate to compute the viscosity.

the viscosity can be determined. For all of the data in Figure 4-1, the steady state viscosity is determined after a period of 5 minutes. One of the drawbacks in using this approach to acquire viscosity-stress plots for the wax-oil system is that the wax-oil is known to experience a sudden yielding behavior after a long period of imposed steady stress, at relatively low stress values. This behavior is illustrated in Figure 4-3. As can be seen from this figure, the 10% wax oil system can actually experience yielding at stresses apparently below σ_y if the imposed stress is held for a long period of time, that is, on the order of several hours.

The data in Figure 4-3 implies that the viscosity-stress measurements are in fact path dependent - the measured viscosity will depend on the specific parameters of the test. It is therefore important to realize what limitations this places on the interpretation of data from Figure 4-1. For example, if the time period to determine steady state viscosity was longer than the stated value of 5 minutes, it is likely that a lower value of the yield stress would be measured for all of the wax oil systems at all temperatures. This is a result of the irreversible behavior exhibited by these systems - they do exhibit shear rejuvenation, however they lack the aging behavior

described by Moller, which is the driving force behind reformation of a material into its pre-yielded state.

The irreversibility of a gelled wax-oil system can be understood by considering the forces which might drive a rearrangement of the wax microstructure. Visintin draws an analogy between waxy crude oils and a colloidal gel [47]. Following this analogy, it is possible to quantify the time scale required for brownian forces to cause sufficient diffusion of the wax crystallites such that they rearrange into a pre-yielded state. This time scale is estimated using equation 4.2, which is described by Sharma et. al. in their study of colloidal dispersions of gold nanorods [39].

$$\tau = \frac{a^3 \mu}{k_b T} \tag{4.2}$$

In equation 4.2, μ is the viscosity of the mineral oil ($\sim 0.1 Pa.s$), T is the temperature of the wax-oil gel, and a is the characteristic size of the wax crystallites ($\sim 30 \mu m$ from Figure 3-5). The value a used here is the characteristic length scale of the crystallites because we are interested in the time required for the crystallites to diffuse a distance on the order of their own size. From equation 4.2, we obtain a time scale of 7×10^5s, which is on the order of weeks. Thus, the wax microstructure is unable to rearrange itself into the pre-yielded state through the action of Brownian motion alone.

4.1.2 Effect of Thermal History on Bulk Rheological Behavior

The data presented in section 4.1.1 was for systems which had undergone a specific thermal beneficiation step in order to form their initial gelled state. This beneficiation step involved cooling the sample at a rate of 1°C/min to the test temperature, and then applying a 10 minute holding time. It was stated in section 4.1.1 that for some types of waxy crude oils, bulk rheological behavior can be highly sensitive to changes in the thermal history of the system [47]. The sensitivity to thermal history on the model system that was used in this thesis was studied. This was accomplished by

measuring viscosity at varying values of stress for a representative model system that had different cooling histories. This data is shown in Figure 4-4. For the data in this particular figure, the effect of cooling rate on the yield strength of a 5% wax oil system at 23°C can be seen.

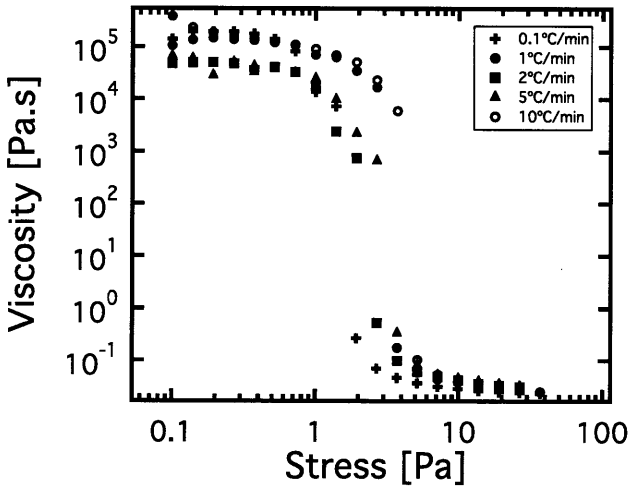

Figure 4-4: Viscosity vs. stress for the 5 % wax-oil system at 23°C having undergone a thermal beneficiation step at a number of different cooling rates. The yield stress of the material is the stress at which the viscosity drops by several orders of magnitude. For this particular plot the change in cooling rate over 2 orders of magnitude does not have a considerable effect on the change in yield stress.

The data in Figure 4-4 was obtained in precisely the same manner as the data shown in 4-1, with the caveat that each set of points was obtained for the 5% system at 23°C having undergone a different cooling rate. Cooling rates within the range of 0.1°C/min to 10°C/min were probed (thus spanning two orders of magnitude). As the plot shows, there is no general trend showing a shift the yield stress of the material in a particular direction. Variations in the value of the yield stress are due to experimental errors alone, and the yield stress varied by a factor of 2 at most. Unlike actual waxy crude oils such as those studied by Visintin, the model system has been engineered to exhibit little sensitivity towards cooling rate. This behavior is ideal for a model system because it is desired that such a system exhibits bulk rheology that can be probed in a reproducible manner.

4.2 Characterizing the Model System through Oscillatory Shear

4.2.1 Small Amplitude Oscillatory Shear

The rheological behavior of the model wax-oil system was also probed through the use of small amplitude oscillatory shear tests (or SAOS). These experiments were carried out in order to understand the effect temperature has on the viscoelastic moduli (G' and G'') of the wax-oil system when it is at a temperature below its wax appearance temperature, T_{wa}. For these particular experiments, the 5% wax-oil system was studied at three distinct temperatures: 23°C, 27°C and 29°C.

For small amplitude oscillatory shear the material response to a sinusoidally oscillating strain of frequency ω ($\gamma(t) = \gamma_0 \sin \omega t$) is a sinusoidally oscillating torque of frequency ω. However, the torque is out of phase with the strain and it is this phase difference, δ, together with the amplitude of the stress signal, A, which is used to calculate the viscoelastic moduli G' and G''. The viscoelastic moduli are calculated from the following formulae.

$$\tan \delta = \frac{G''}{G'} \tag{4.3}$$

$$A = \sqrt{G'^2 + G''^2} \tag{4.4}$$

Where G' and G'' are based on a decomposition of the stress into two parts, a component which is in phase with the strain, and a component which is $\pi/2$ radians out of phase with the strain (the elastic and viscous components respectively). This decomposition can be written as follows.

$$\sigma = G'(\omega)\gamma_0 \sin \omega t + G''(\omega)\gamma_0 \cos \omega t \tag{4.5}$$

It is important to realize that the equations above assume that the oscillatory strain amplitude (γ_0) is small enough such that the material is being perturbed within the linear regime. The consequences of being in the linear regime are that an sinusoidally oscillating strain "input" will have a sinusoidally oscillating stress "output", which

differs from the input by a phase difference and a scaling parameter. When the material is perturbed at large amplitudes, and is no longer within its linear regime, then the stress "output" may no longer vary sinusoidally over time. It can also be shown that for small amplitude oscillatory shear, whenever the stress is plotted against the strain for a particular period (a Lissajous curve); the curve which forms will always be an ellipse. Equation 4.5 can be rearranged to make this apparent. From equation 4.5:

$$(\sigma - G'\gamma)^2 = (\gamma_0 G'' \cos\omega t)^2 \tag{4.6}$$

$$= (G'')^2(1 - \sin^2\omega t) \tag{4.7}$$

Equation 4.7 can then be rewritten as follows:

$$\sigma^2 - 2G'\sigma\gamma + \gamma^2(G'^2 + G''^2) = G''^2\gamma_0^2 \tag{4.8}$$

Which is the general equation for an ellipse tilted about the ordinate and abscissa (in this case the γ and σ axes respectively).

Figure 4-5 shows the values of G' and G'' at different values of oscillation frequency for the 5% wax oil system (at 3 different temperatures, having undergone a 1°C/min thermal beneficiation step in each case). For these particular experiments, the material was submitted to a sinusoidal strain oscillation of amplitude $\gamma_0 = 0.1\%$ - this is sufficiently low such that the material response is within the linear regime, i.e. the stress also forms an oscillating sinusoid in time. As can be seen from the figure, the 5% system acts as a linear viscoelastic solid, with the value of G' being consistently larger than G''. Not much variation is seen in the viscoelastic moduli as the frequency changes. However, the phase angle δ appears to reach a minimum in each case at a value of ω approximately equal to 1 rad/s.

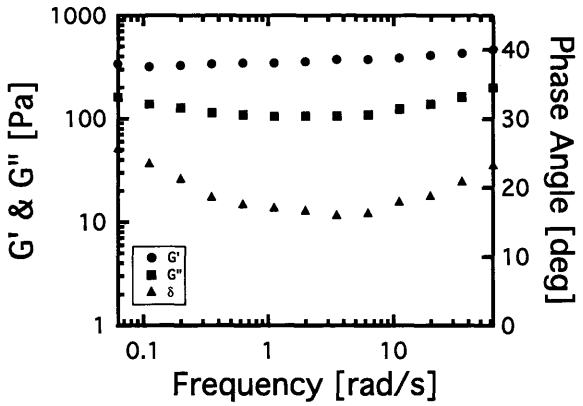

(a) 5% wax-oil at 23°C

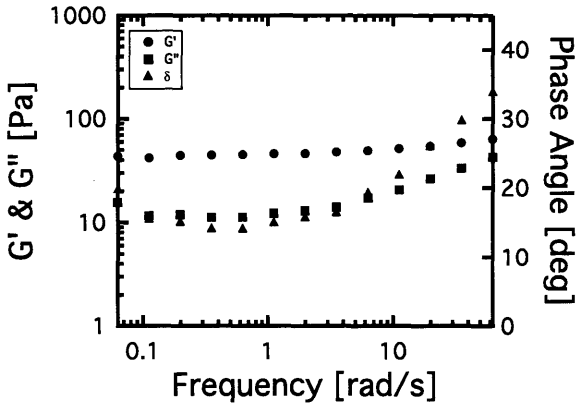

(b) 5% wax-oil at 27°C

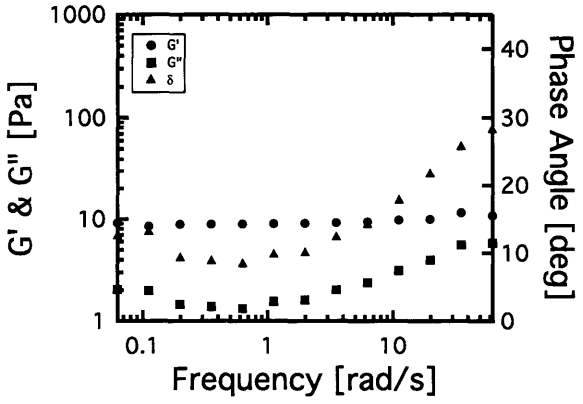

(c) 5% wax-oil at 29°C

Figure 4-5: Small amplitude oscillatory shear for the 5% wax oil system at a number of temperatures below T_{wa}. Each plot shows that the value of G' is consistently larger than the value of G'', implying that the material behaves as a viscoelastic solid below the wax appearance temperature.

4.2.2 Large Amplitude Oscillatory Shear - Framework

One additional way to gain insight into the bulk rheology of the model wax-oil system is through measuring its response to large amplitude oscillatory shear (or LAOS). The reason why LAOS provides a greater utility than SAOS in characterizing the rheology of the wax-oil system is because the linear regime for the model wax-oil system can only be probed at amplitudes that are typically below a fraction of a percent. Experiments such as those shown in Figure 4-3 are quite clearly dealing with strain amplitudes that are far outside the linear regime. Thus, some understanding of the system's behavior at strains which are outside of the linear regime is helpful.

LAOS is a technique whereby the material is deformed beyond its linear regime in an oscillatory fashion, and the resulting stress required for this deformation is measured over time. In the instance where a large enough deformation is imposed on the material, the resulting stress experienced by the material (or the material response) will oscillate with the same period as the oscillating strain, but will exhibit higher harmonics. It is the existence of these higher harmonics which distinguishes the linear deformation regime from the non-linear regime. LAOS generalizes the representation given by equation 4.5 by including these higher harmonics in the decomposed stress response. Ewoldt [13] gives the following stress decomposition for large amplitude oscillations:

$$\begin{aligned} \sigma' &= \gamma_0 \sum_{n\,\text{odd}} G'_n(\omega, \gamma_0) \sin n\omega t \\ \sigma'' &= \gamma_0 \sum_{n\,\text{odd}} G''_n(\omega, \gamma_0) \cos n\omega t \end{aligned} \tag{4.9}$$

Where σ' is the elastic stress component and σ'' is the viscous stress component. The framework which is developed by Ewoldt goes further than this simple decomposition by writing the sums given in 4.9 as sums of nth order Chebyshev polynomials. When

these sums are rewritten the following equations are obtained.

$$\sigma' = \gamma_0 \sum_{n\,\text{odd}} e_n(\omega, \gamma_0) T_n(x)$$
$$\sigma'' = \dot{\gamma}_0 \sum_{n\,\text{odd}} v_n(\omega, \gamma_0) T_n(y) \tag{4.10}$$

Where T_n are the nth order Chebyshev polynomials of the first kind, $x(t) = \gamma(t)/\gamma_0$ is a scaled strain and $y(t) = \dot{\gamma}(t)/\dot{\gamma}_0$ is a scaled strain rate. By writing the decomposed stress response in this way, the viscous and elastic Chebyshev coefficients, v_n and e_n respectively, can be used as a metric for the non-linear behavior of the system. In most instances, the even-harmonic terms of the series representation given in equation 4.9 are zero - this is based on the assumption that the stress response is of odd-symmetry and cannot be changed if the coordinates system is reversed [6]. As a result, the general response of a system to an large amplitude oscillatory deformation has non-zero values of e_{2n-1} and v_{2n-1} where n is an integer value from 1 to infinity. In the case of SAOS in the linear regime, the only non-zero Chebyshev coefficients are e_1 and v_1. Since the first order Chebyshev polynomial $T_1(x)$ is simply equal to x, we have the following stress response of the material.

$$\sigma' = \gamma_0 e_1(\omega) x = e_1(\omega)\gamma(t)$$
$$\sigma'' = \dot{\gamma}_0 v_1(\omega) x = v_1(\omega)\dot{\gamma}(t) \tag{4.11}$$

Because $\sigma = \sigma' + \sigma''$, $\gamma(t) = \sin\omega t$, and $\dot{\gamma}(t) = \omega\cos\omega t$ it is clear that equation 4.11 is the same representation given in equation 4.5, where e_1 and v_1 are related to G' and G''. Thus, the representation for LAOS collapses into the stress decomposition for SAOS when the Chebyshev coefficients of order 3 and larger are zero, while large values of the higher order Chebyshev coefficients imply a system which is exhibiting a non-linear response. It is therefore instructive to consider the ratios e_3/e_1 and v_3/v_1 as numbers that quantify how non-linear the behavior of a system is. In the limit of these ratios being equal to zero, the linear response for SAOS is recovered. When the higher order Chebyshev coefficients are non-zero, they can be related to the values of

G'_n and G''_n which are given in equation 4.9. These values are easy to calculate from a discrete Fourier transform of a series of stress values measured over a period of time [14]. Ewoldt argues that for most non-Newtonian fluids, the material stress response to a large sinusoidal deformation can be well approximated by a summation up to the third Chebyshev coefficients, v_3 and e_3. The values of e_3 and v_3 for a particular stress response can thus adequately describe the nonlinear behavior of most materials. The specific effect that the sign of v_3 and e_3 have on the elastic and viscous components of the stress response is as follows:

$$e_3 \begin{cases} < 0 & \text{Strain softening material} \\ > 0 & \text{Strain stiffening material} \end{cases}$$

$$v_3 \begin{cases} < 0 & \text{Shear thinning material} \\ > 0 & \text{Shear thickening material} \end{cases}$$

Furthermore, as stated previously, the relative magnitude of e_3 and v_3 with respect to e_1 and v_1 provides a measure of how pronounced these types of non-linear of behavior are compared to the linear elastic and viscous behavior (which is quantified using G' and G'' for SAOS). The following large amplitude oscillatory data for the wax-oil system is presented using this framework. The Chebyshev coefficients e_n and v_n are used to gain insight into the non-linear rheology of the model system.

4.2.3 LAOS Results

For all of the LAOS measurements that were carried out on the model wax-oil system, the strain rate controlled ARES rheometer was used, with a roughened cone and plate geometry (diameter 50mm, cone angle 0.0402 radians). LAOS measurements were carried out on the 5% and 10% wax-oil system at a temperature of 23°C. This particular temperature was chosen because at low temperatures the wax oil gel is strong enough to exhibit a large stress signal when it undergoes small oscillating strains. At higher temperatures (especially for the 5% system), the stress signal is often too small for the instrument to extract meaningful data at strain amplitudes

on the order of a percent.

The 5% and 10% samples were cooled down to this specific temperature at a cooling rate of 1°C/minute, and then a 10 minute holding time was applied to the sample. The stress and strain data from an imposed oscillatory shear of a given value of ω and γ_0 is typically illustrated in the form of a Lissajous curve, $\sigma(t)$ vs. $\gamma(t)$. However, because it is useful to probe the behavior of the material over a wide range of amplitudes and frequencies, these Lissajous curves can be more conveniently represented in the form of a Pipkin diagram, as shown in 4-6

In Figure 4-6 we show the response of the 5% wax oil system to a range of strain amplitudes and frequencies. As can be seen from the plot, at low strains the behavior of the material is linear, and can be represented by simple ellipses. However, non-linear behavior becomes evident at just a fraction of a percent, as is evident from the change in shape of the Lissajous curves. These curves change from ellipse-like at low strain amplitudes, to non-ellipsoid at higher amplitudes. As discussed in section 4.2.2, an ellipse shaped Lissajous curve implies that the material is being perturbed in its linear regime, and the stress decomposition described in equation 4.5 is sufficient to explain the behavior of the material. Another thing to notice about the Lissajous curves is that they go through an initial transient behavior which eventually settles into a steady state after several oscillations.

Within the pipkin plot, the amplitude of the stress is given for each Lissajous curve. One thing to notice about Figure 4-6 is that for strain amplitudes less than 0.5% this stress amplitude is generally less than the yield strength of the material at that particular temperature (determined to be 4 Pa from Table 4.1.1). Thus, it appears that the material exhibits a yielding behavior at strains larger than this value.

Figure 4-7 shows the response of the 10% wax-oil system to large amplitude oscillations at a range of strains and frequencies. At first sight the behavior seems qualitatively similar to what is observed for the 5% system, however this particular system's stress response becomes weaker as frequency is increased, instead of a stronger stress response which is the case for the 5% system.

In order to further understand the behavior of the model wax oil system below the

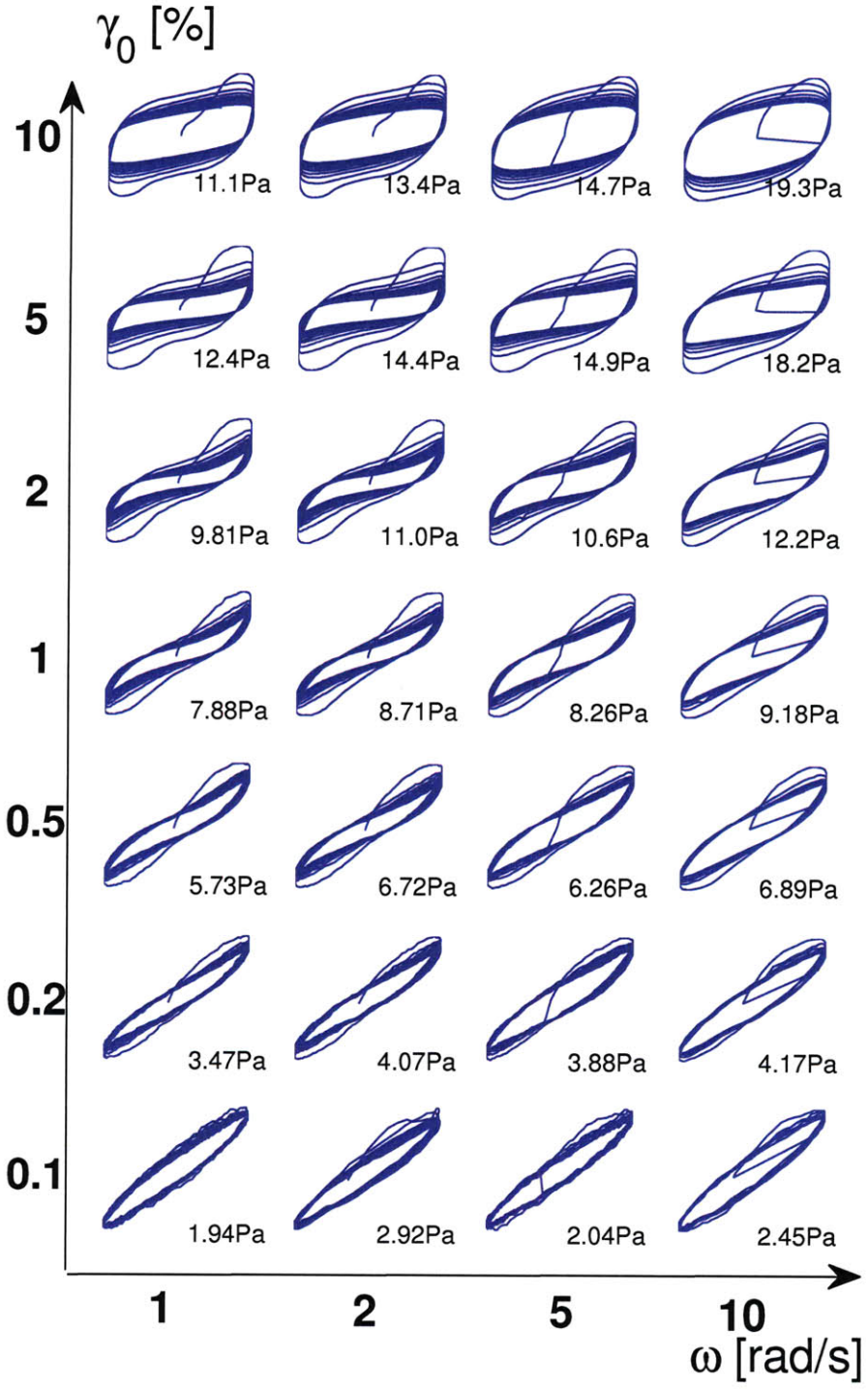

Figure 4-6: Pipkin Diagram of 5% wax oil system at 23°C. Each Lissajous curve shows a total of 12 cycles of oscillation. As can be seen from the curves, the material tends to exhibit an initial transient behavior where higher stress amplitudes are reached, however this behavior eventually settles in to a steady state (typically after about 4 cycles). The maximum stress experienced during each set of cycles is also indicated.

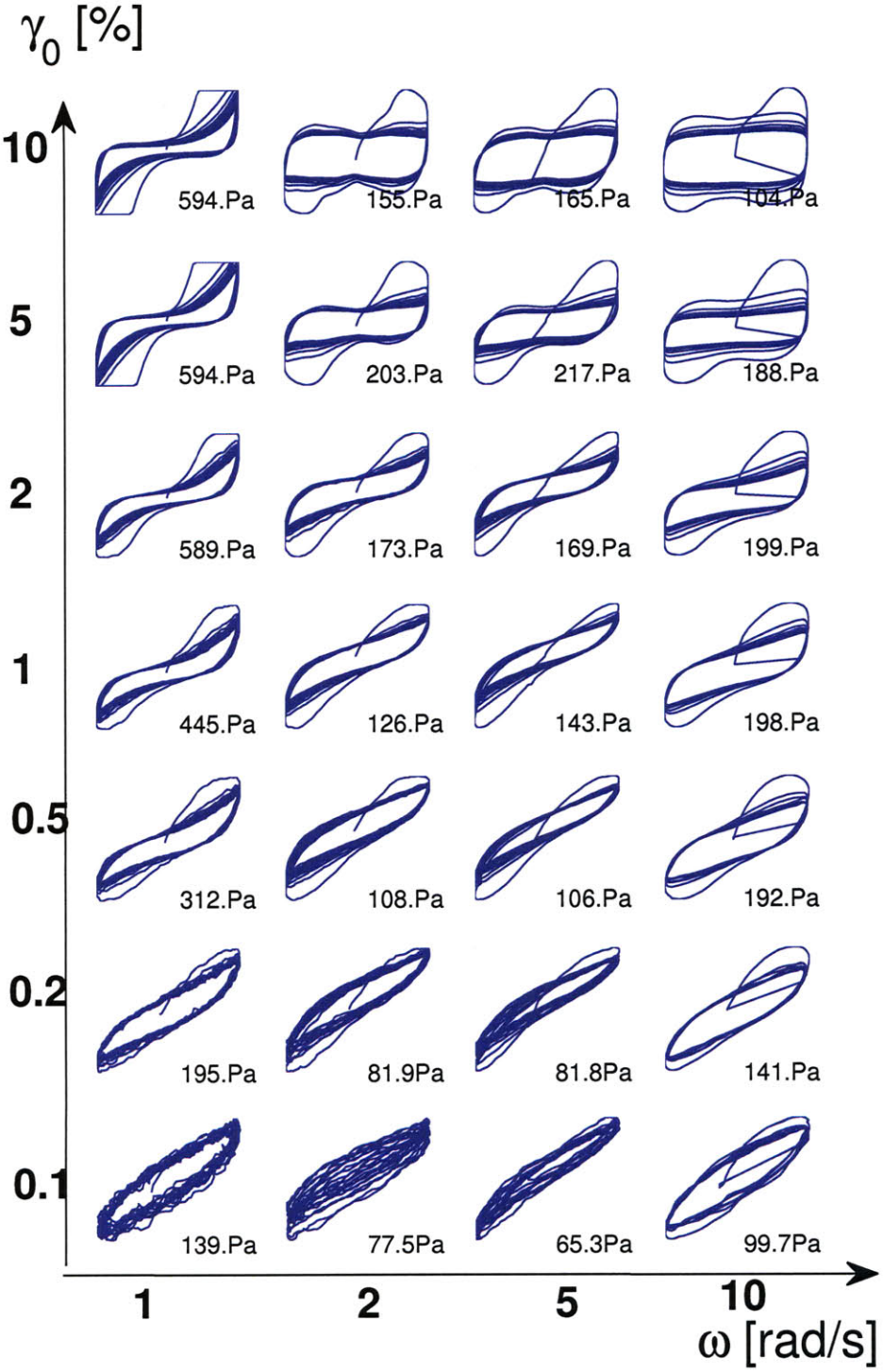

Figure 4-7: Pipkin Diagram of 10% wax oil system at 23°C. Each Lissajous curve shows a total of 12 cycles of oscillation. As can be seen from the curves, the material tends to exhibit an initial transient behavior where higher stress amplitudes are reached, however this behavior eventually settles in to a steady state (typically after about 4 cycles). The maximum stress experienced during each set of cycles is also indicated.

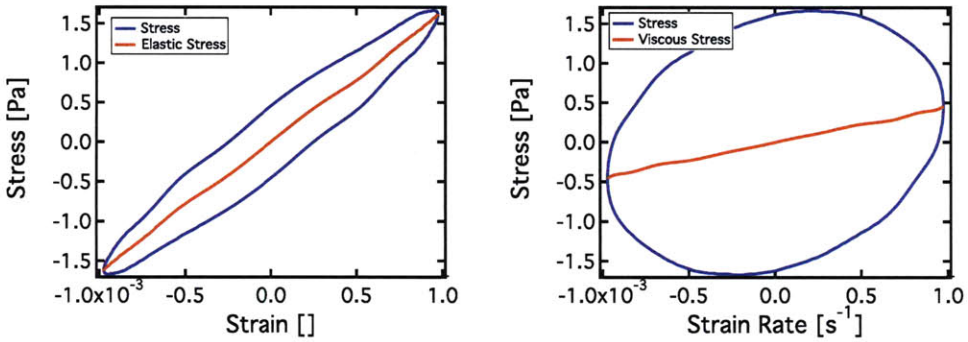

(a) Decomposed stresses at $\gamma_0 = 0.1\%$ and $\omega = 1\text{rad/s}$

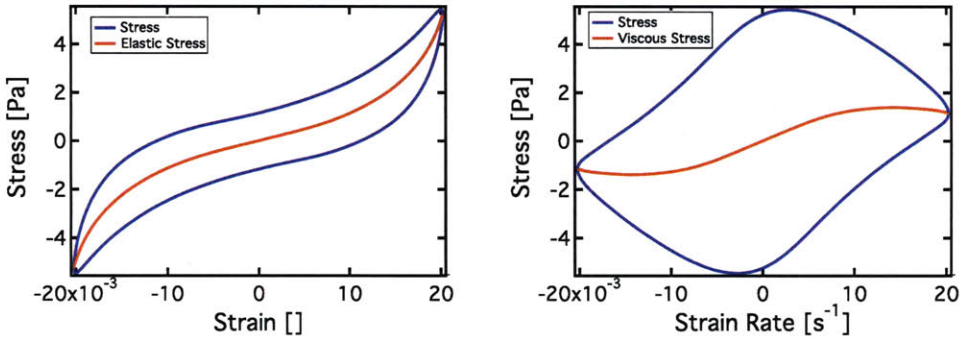

(b) Decomposed stresses at $\gamma_0 = 2\%$ and $\omega = 1\text{rad/s}$

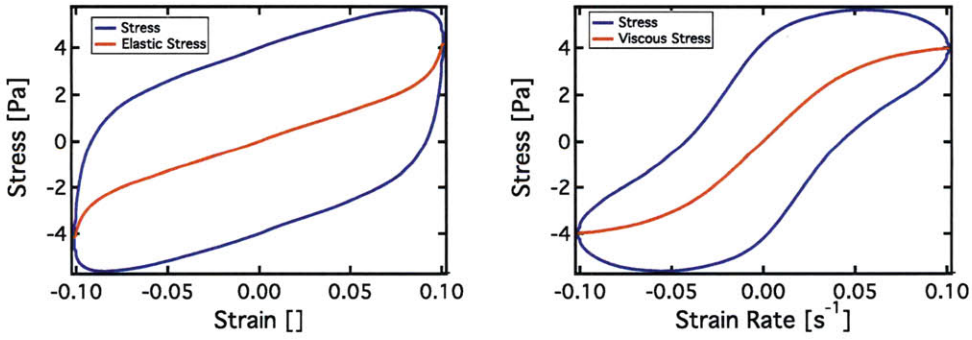

(c) Decomposed stresses at $\gamma_0 = 10\%$ and $\omega = 1\text{rad/s}$

Figure 4-8: Decomposed stresses for the 5% wax oil system at 23°C at 3 different imposed strain amplitudes, with a frequency of 1 rad/s. Stress curves are formed by averaging and smoothing 5 periods of oscillation (after transients have died out in the response). Progression of the material is seen from a linear viscoelastic solid at low strains, to a strain stiffening viscoelastic solid at intermediate strains. At the highest strain amplitudes, the behavior of the system appears to act as a viscoelastic liquid.

wax appearance temperature, it is helpful to decompose several of the stress response curves into their elastic and viscous components and determine the values of the Chebyshev coefficients, e_3 and e_1, v_3 and v_1. The plots show in Figure 4-8 show the stress decompositions for the 5% system at 23°C at a number of strain amplitudes. It is important to realize that this is done for the steady state response, i.e. after any transients have died out. The transients for this particular system typically last for 5 cycles. The decomposed stress components are given by the red curves, while the blue curves give the total stress. Each of these decomposed curves are determined using the following equations [13]:

$$\sigma' = \frac{\sigma(\gamma,\dot{\gamma}) - \sigma(-\gamma,\dot{\gamma})}{2} = \gamma_0 \sum_{n\,\text{odd}} G'_n(\omega,\gamma_0)\sin n\omega t$$
$$\sigma'' = \frac{\sigma(\gamma,\dot{\gamma}) - \sigma(\gamma,-\dot{\gamma})}{2} = \gamma_0 \sum_{n\,\text{odd}} G''_n(\omega,\gamma_0)\cos n\omega t \tag{4.12}$$

The values of G'_1, G''_1, e_3 and v_3 can be calculated from the decomposed curves which are obtained using equation 4.12 above. Table 4.2.3 summarizes the values of the Chebyshev coefficients, and other relevant quantities for the plots shown in Figure 4-8. One quantity in table 4.2.3 which has yet to be introduced is the value ϕ, which represents the ratio between energy dissipated per cycle for the system and energy dissipated per cycle for a perfectly plastic material. It ranges between 0 (elastic material) and 1 (perfectly plastic material) and Ewoldt provides the following formula for its calculation [14]:

$$\phi = \frac{\pi\gamma_0 G''_1}{4\sigma_{\max}} \tag{4.13}$$

The values shown in table 4.2.3 give a good summary of how the behavior of a wax oil system depends on the strain that is imposed on it. For low strains (0.1% or lower) the material acts as a viscoelastic solid, with a large storage modulus and a loss modulus which is smaller than G' by a factor of 3. The values of e_3 and v_3 are small compared to the values of G' and G'', so the system is not exhibiting non-linear behavior at this amplitude. At the higher amplitude of 2%, the system exhibits a more pronounced non-linear behavior, given by the much larger value of e_3/e_1. Furthermore, this non-

Strain Amplitude (γ_0)	G_1' [Pa]	G_1'' [Pa]	e_3 [Pa]	v_3 [Pa]	e_3/e_1	ϕ
0.1%	1637	448	18.7	5.14	0.011	0.18
2%	198	79.3	46.8	-23.0	0.1416	0.2273
10%	32.2	45.6	4.56	-7.35	0.14	0.6373

Table 4.2: Summary of extracted parameters from the decomposed stress curves shown in Figure 4-8. Parameters are for the 5% wax system at a temperature of 23°C undergoing oscillations at a frequency of 1 rad/s.

linear behavior is characterized by a strain stiffening (positive value of e_3) and a shear thinning (negative value of v_3). The system now dissipates a slightly larger amount of energy at this amplitude (larger value of ϕ), but generally it is appropriate to refer to the material as a "strain stiffening solid" at these intermediate strain ranges. At the highest strain ranges, the value of G' drops dramatically, indicating that the material has moved towards more of a liquid state (and this indeed is reasonable since the stress has now far exceeded the yield stress). The material still exhibits a slight strain stiffening and shear thinning response, however the most interesting change that occurs at this higher strain is the considerable increase in the value of ϕ. This large value of ϕ and lower value of G' indicates that the material has now yielded and behaves mostly as a viscoelastic liquid.

4.3 Dependence of Material Response on Surface Conditions

As mentioned previously, the rheological behavior described so far has assumed that the no slip condition holds for the model-wax oil system under flow. This was ensured by using a roughened geometry for all rheological measurements. Specifically, the solid surfaces were covered with 320 grit adhesive backed sandpaper with a root mean squared roughness, $R_q \sim 30\mu m$. When the wax-oil system is solidified in contact with a smoother surface (in this case a machined aluminum surface, $R_q \sim 0.1\mu m$) the rheological behavior changes drastically due to the presence of wall slip [4].

One artifact of this slip presents itself in the shape of the viscosity vs. stress curves

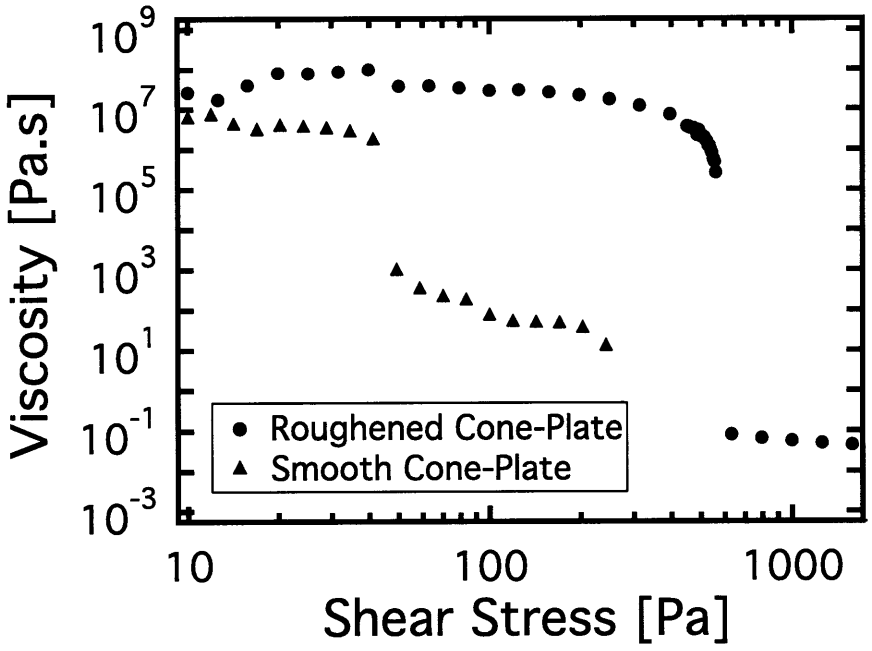

Figure 4-9: Steady state viscosity-stress curve for a 10% wax-oil system at 23°C measured using the roughened cone plate geometry and a smooth cone plate geometry

for a model system experiencing a steady shear stress at $T < T_{wa}$ within the confines of a roughened geometry in one case, and a smooth geometry in the other. Figure 4-9 illustrates the difference for these two cases for a 10% wax-oil system at a temperature of 23°C (the value of T_{wa} for this particular system is 36°C). The particular system went through a thermal beneficiation step for each set of measurements, i.e. a 1°C/min cooling rate was imposed down to the test temperature, with a subsequent 10 min holding time following this step. Furthermore, whenever a stress was imposed on the system, the steady state shear rate was determined after a period of 5 minutes, and the viscosity was calculated from this steady shear rate value.

The data shows that at low stresses, below σ_y, the measured viscosity for the sample placed between the smooth geometry is much lower than expected. Barnes [4] shows a similar type of behavior for a printing ink, explaining that the lower viscosity in the case of the smooth surface is the result of slip at the fluid-solid boundary. One might expect the same type of behavior to be present in the model wax-oil system. However, in the case of the model wax-oil, the only way to be certain that slip occurs

is by directly visualizing the flow field within the fluid while it is under shear.

This flow visualization was carried out using the velocimetric system described in section 3.2.1. In particular, a sequence of creep tests was carried out on a wax-oil system cooled to below T_{wa}, in which the imposed stress is incrementally stepped (in a logarithmic fashion) from a value below the yield stress to a value above it. For each of the creep steps, the imposed stress is held for a period of 60s and a video recording was acquired for later analysis to determine the flow field within the sample. This sequence of creep tests was carried out for the wax-oil system in contact with a roughened lower geometry (again achieved using adhesive backed sandpaper), and for a smooth lower geometry. In both cases the top geometry was a quartz glass plate, which was necessary to allow a path for the laser beam. In this experiment, a 5% wax-oil model fluid was used at a higher test temperature (29°C), such that the sample did not become too opaque and imaging through the fluid was still possible. However, the 5% wax-oil system at 29°C is still below the wax appearance temperature. Table 3.1.2 shows that for this particular system the wax appearance temperature is $T_{wa} = 30.5$°C.

The bulk rheological data from this particular experiment is shown in Figure 4-10. From this data, it is apparent that the system exhibits both larger strains and larger strain rates when it is in contact with a smooth bottom surface. Hence, the measured viscosity is generally lower. This behavior is consistent with the data shown in Figure 4-9. Once again, one might anticipate this behavior to be a result of slip. This hypothesis can be verified through an analysis of the corresponding PIV data. For each sequence of creep tests, we are interested in the time period over which the material experiences considerable flow, such that it is possible to register a large enough displacement of the seed particles using the imaging system. For the sample in contact with the smooth lower fixture, this time period occurs beginning at the 180s mark, when the imposed stress is $\sigma = 0.2$ Pa. On the other hand, the velocimetric system only registers a displacement large enough for the roughened case when the imposed stress reaches $\sigma = 0.5$ Pa. Two representative velocity profiles are also shown in Figure 4-11 for the wax oil system during each of these steps. These velocity profiles

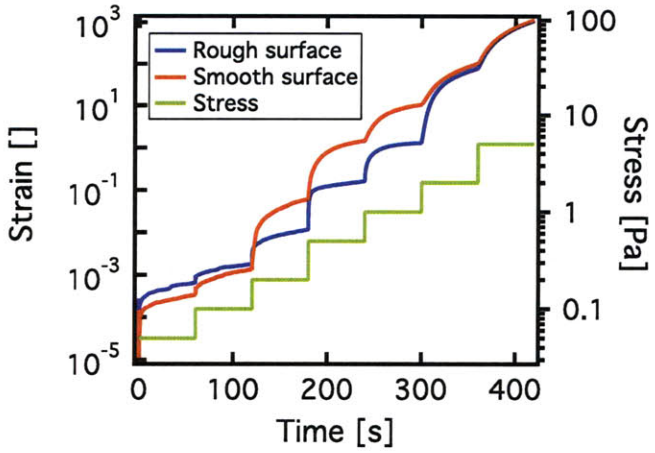

Figure 4-10: Bulk rheological data obtained from the rheometer during the sequence of creep tests that were imposed on the 5% wax oil system at 29°C. Red curve corresponds to the smooth lower surface, while the blue curve corresponds to the rough surface. On the smooth surface, the system exhibits a higher accumulated strain at the intermediate stress steps - this is a result of slip.

show that the mechanism through which the material yields is different in both cases.

For this particular set of experiments, the imaging system acquired video at a frame rate of 18 fps. As a result, approximately 1000 velocity profiles were acquired over the course of each 60s creep step. In order to illustrate the spatial and temporal evolution of these profiles using one image, the profiles can also be plotted in the form of a "space-time diagram". These diagrams allow one to easily discern the form of the velocity profile within the rheometer gap over a long period of time - they are identical to the plots used by Gibaud et. al. to observe velocity profiles in Laponite dispersions [19] under steady shear rates. Figure 4-12 shows spatiotemporal diagrams for the roughened creep test beginning at 240s, and the smooth creep test beginning at 180s.

These figures show a dramatic difference between the flow profiles. When the sample is in contact with the smooth geometry and the stress is increased to 0.2 Pa (at the 180s mark), there is a sudden appearance of a bulk-flow like profile within the rheometer gap. In particular, there is a constant velocity through the gap, with a small region near the bottom plate which quickly drops to a velocity of zero. This

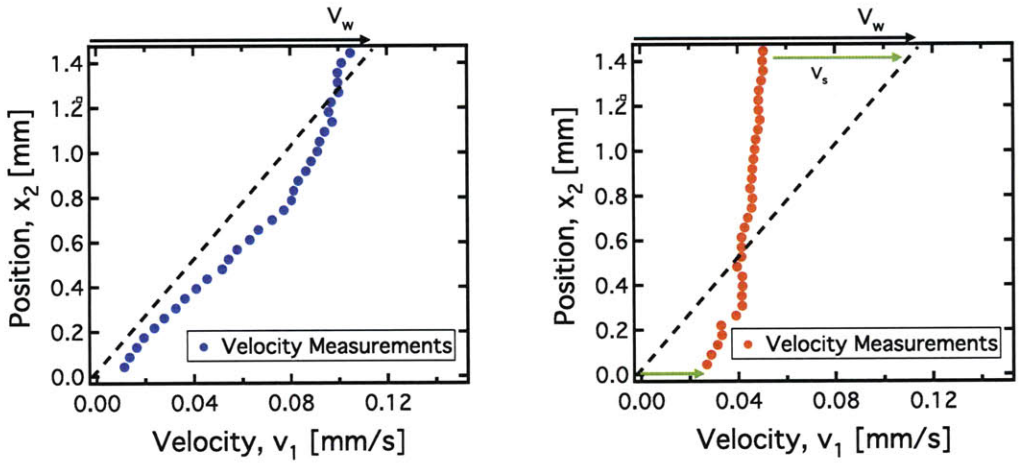

Figure 4-11: Representative velocity profiles extracted from the velocimetric system during the 0.2 Pa stress step on the smooth surface at 183 seconds (left), and during the 0.5 Pa stress step on the rough surface at 245 seconds (right). Slip velocity v_s and wall velocity v_w is annotated in each figure. As can be seen from the two plots, the system clearly exhibits a plug like flow at a lower shear stress when it is in contact with the smooth geometry. On the other hand the roughened geometry results in a linear velocity profile within the sample.

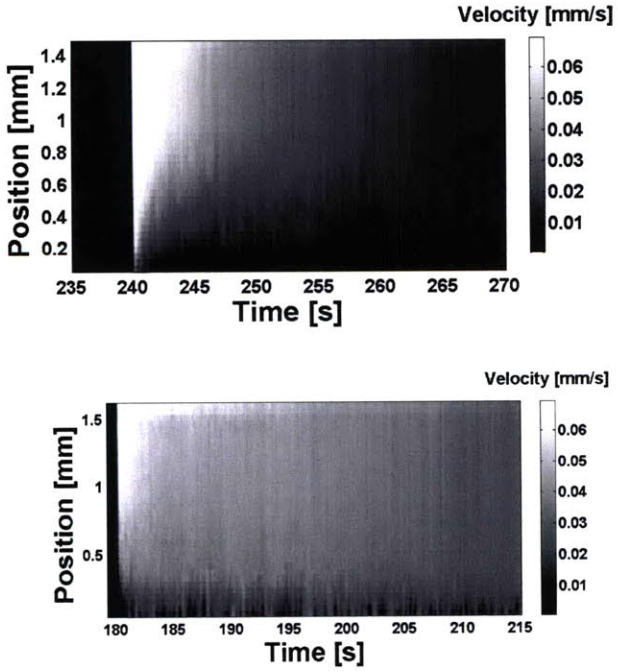

Figure 4-12: Spatiotemporal diagrams for roughened (top plot) and smooth (bottom plot) instances. The stress imposed at the 240 second mark in the top plot is 0.5 Pa, while the stress imposed at the 180 second mark in the bottom plot is 0.2 Pa.

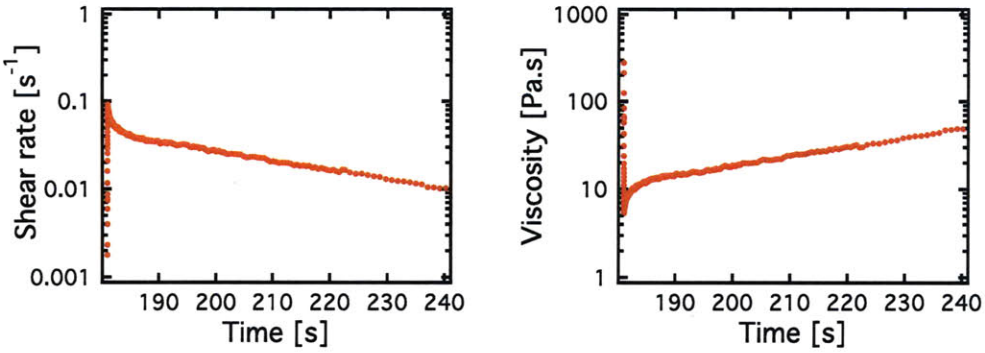

(a) Strain rate and viscosity for the smooth instance beginning at 180 seconds

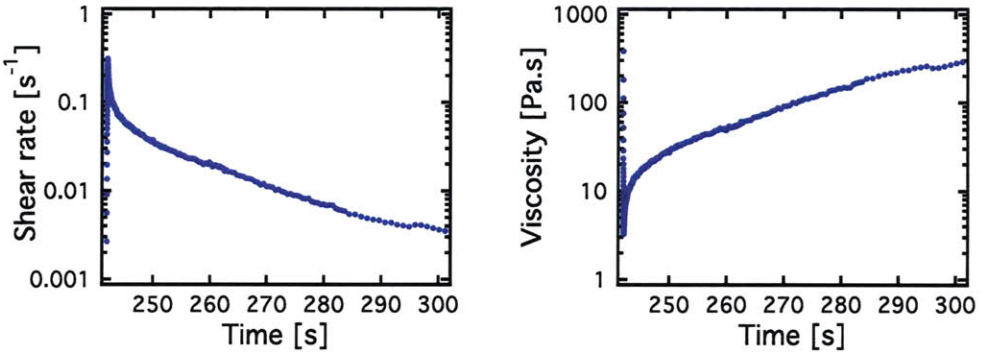

(b) Strain rate and viscosity for the rough instance beginning at 240 seconds

Figure 4-13: Strain rate and viscosity vs. time obtained from the bulk measurements of the rheometer. For the roughened instance, the time axis begins at the 240 second mark (when the 0.5 Pa stress is imposed), while the time axis begins at the 180 second mark for the smooth instance, when a 0.2 Pa stress step is imposed.

thin region near the bottom plate experiences a higher shear rate than the rest of the fluid, and its thickness is approximately 0.25mm. For the sample in contact with the roughened lower geometry, this type of plug-flow like profile is never observed. Instead, a more uniform shear rate is observed throughout the gap during the period of observation (this is also supported by the plot in Figure 4-11). In the space time diagram, this uniform shear rate can be discerned because of the gradual color variation along the position axis, for any given period of time. In addition to this, the shear rate within the gap decreases in time - this is consistent with the bulk measurements taken by the rheometer (which are showed in more detail in Figure 4-13). Hence, slip no longer occurs on the bottom surface when the sample is in contact with the a roughened surface.

The spatiotemporal diagrams in Figure 4-12 essentially verify that the wax-oil system can flow at lower shear stresses through the mechanism of slip on the solid surface. However, this behavior should not preclude bulk yielding at higher shear stresses. In fact, when the velocimetric data from the 0.5 Pa creep step (beginning at 240s) for the smooth surface case is analyzed, the shear rate within the bulk of the sample appears to be non zero. Some slip still occurrs, however the flow of the material is due to a combined effect of both slip and shearing in the bulk. Furthermore, the shear rate within the bulk should be roughly equal to the shear rate within the bulk for the roughened case - this is because they are the same sample, with the same thermal history and roughly the same shear history (the effect of thermal history on these samples was documented in section 4.1.2).

Eventually, at high enough shear stress, the creep curves for the two different test configurations converge, indicating that at high enough shear stresses the contribution of flow due to slip is negligible, and the bulk material has broken down enough in both instances such that they are able to both experience a uniform shear rate across the gap. At these high shear stresses, surface characteristics have no effect on the flow. The viscosity value which is measured at these high stresses is approximately 0.02 Pa.s, which is roughly the same viscosity that is measured for the 5% wax oil system at a temperature of 29°C in Figure 4-1. The specific time-dependent behavior of the gelled model wax-oil system will be discussed in the following section, in which the changes in velocity profiles over time are observed for a sample undergoing a steady shear rate.

4.3.1 Dynamics of Velocity Field Under a Constant Apparent Shear Rate

The experiment in Figure 4-12 shows that it is possible for the model wax-oil system to experience a plug-like flow profile within the rheometer gap, provided that the sample is in contact with a smooth surface. An interesting question that one might pose after witnessing this type of behavior is whether or not this flow configuration is

stable over long periods of time. As shown previously, the model wax-oil system can experience an irreversible yielding transition which results in a dramatic drop in its viscosity, and this high viscosity cannot be recovered unless the sample goes through a thermal rejuvenation step. It thus seems natural to expect some type of irreversible change in the flow profile over time.

In order to address this question, the 5% wax-oil system was prepared to a temperature of 27°C through the same preparation protocol as described in section 4.1. Then, instead of imposing a sequence of steady stress steps, and observing the samples deformation in time, a steady shear rate is immediately imposed on the sample. For this particular experiment, the 50mm cone and plate geometry was used with smooth lower and upper surfaces. During the experiment two complementary measurements to be taken over the course of several minutes while the sample is undergoing steady shearing deformation at $\dot{\gamma} = 0.1\text{s}^{-1}$. The first is the applied torque which is imposed by the rheometer on the sample, and the second in the velocity profile recorded within the geometry gap.

Both of these sets of measurements are shown in Figure 4-14. As can be seen from the data, the stress imposed by the rheometer goes through an initial transient phase, during which the shear stress increases from zero. This transient phase results in a peak shear stress being reached after a period of approximately 20 seconds (the peak shear stress value at this point is 0.68 Pa, which corresponds to an instantaneous viscosity of 6.8 Pa.s). After the peak shear stress is reached, the stress begins a slow decline toward what appears to be a steady value.

The data in Figure 4-14(b) is somewhat more difficult to interpret. However, after looking closely, it is apparent that there is an initial time period where the flow profile within the sample is of the form of a plug-like profile. In addition to this, the velocity within the bulk of the material is approximately half of the velocity of the top surface that the sample is in contact with. This implies that there is an almost equal slip velocity on the top and bottom surfaces. Figure 4-14(c) shows the velocity profiles at 3 different points in time during the steady shear test. The middle velocity profile coincides with the time period where a plug-like flow profile is observed.

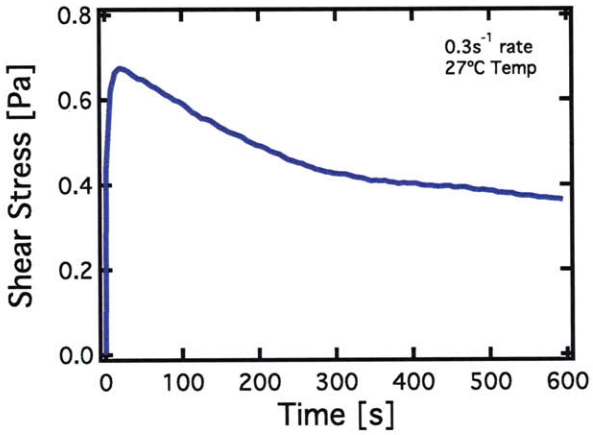

(a) Stress imposed on the 5% wax-oil sample over a period of 10 minutes. The shear rate is held constant at $\dot{\gamma} = 0.3\text{s}^{-1}$. Both rheometer surfaces are smooth.

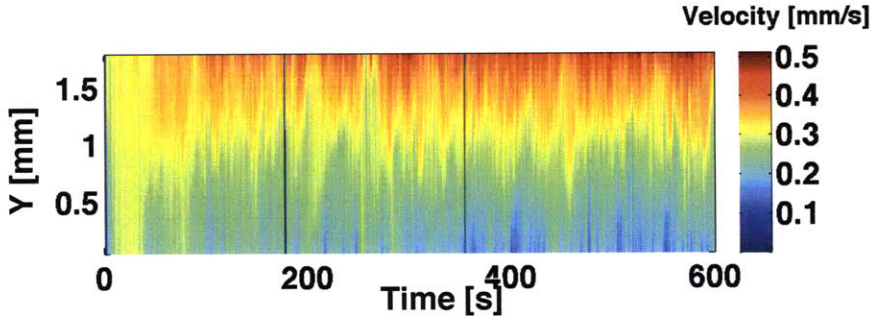

(b) Space-time diagram of the velocity within the sample while undergoing a shear rate of 0.3s^{-1}. Time axis corresponds to time axis in stress plot

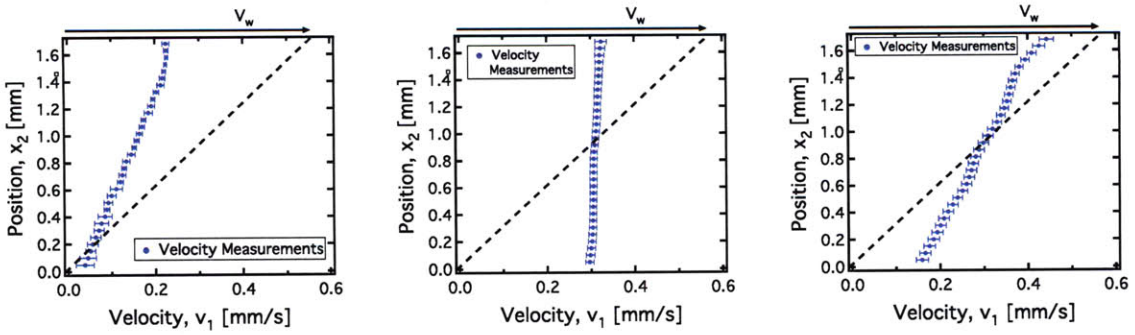

(c) Velocity profiles at time period of 2 seconds (left), at a time period of 20 seconds averaged over 30 frames (middle) and at a time period of 600 seconds also averaged over 30 frames (right). Error bars are standard deviations in the measurement.

Figure 4-14: Spatiotemporal plot, velocity profiles and rheological data for a 5% wax oil sample undergoing steady shear, $\dot{\gamma} = 0.3s^{-1}$ System was kept at a constant temperature of 27°C ($T_{wa} = 31$°C for this system)

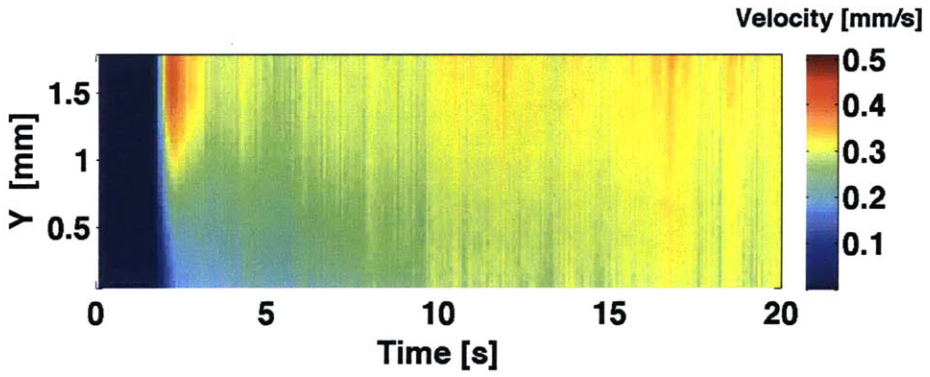

Figure 4-15: First 20 seconds of the data shown in Figure 4-14(b)

In order to make the initial behavior of the flow profile clearer, Figure 4-15 shows the initial 20 seconds of the data given in Figure 4-14(b). For this particular plot, the beginning of steady shearing of the top geometry occurs approximately at the 2 second mark. One interesting feature of this plot is that for the first second when the steady rotation rate of the upper geometry is imposed, there is an almost uniform shear rate within bulk of the sample. This can be distinguished because of the gradual color variation along the position (or Y) axis for the initial period when the flow begins. It can also be observed in the velocity profile for the 2 second mark in Figure **??** After these first few seconds, the shear rate within the bulk of the sample drops to zero and the flow is almost entirely due to slip. This slip, which results in a plug-like flow profile, occurs for a period of approximately 40 seconds. At the 40 second mark, the velocity near the bottom plate decreases, while the velocity near the top plate increases. Hence, the plug-like profile changes to something that more closely resembles a linear profile.

However, this change is neither a fast, nor a smooth transition. When looking closely at the data shown in Figure 4-14(b), it becomes apparent that over the entire period of the experiment, there are considerable variations over time in the velocity along the same position within the rheometer gap. There are also periods of time when the flow profile seems to switch from plug-like to linear, and then back to plug-like. This suggests that the material is spatially heterogenous, consisting of localized regions which contain fluid elements experiencing high shear rates, and other regions

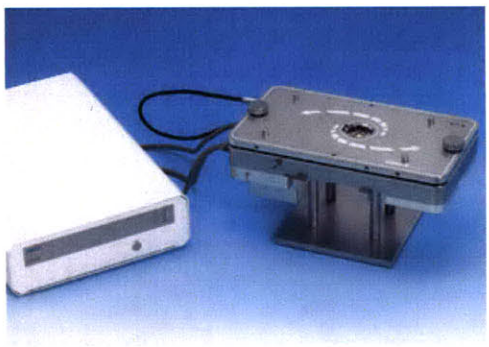

(a) Photograph of the Linkam Shear cell

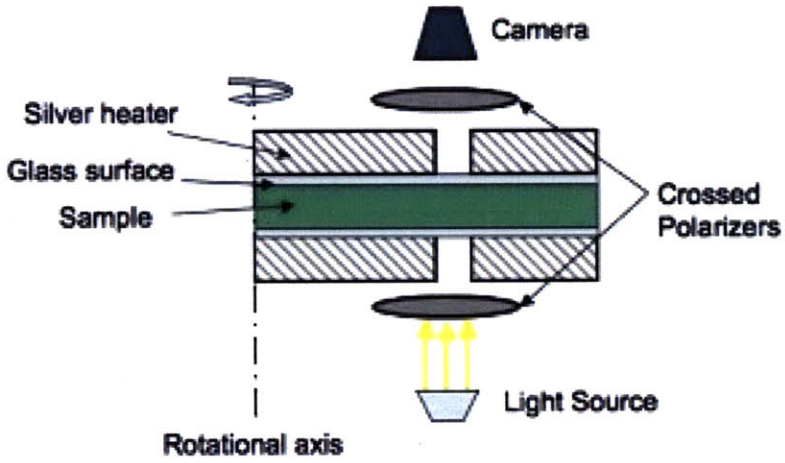

(b) Schematic Diagram of Linkam Shear cell

Figure 4-16: Photograph and schematic diagram of the Linkam CSS450 Shear cell

where the sample is almost rigid and experiences little or no deformation. Such observations are consistent with what has been seen for wax oils under shear using a rather different imaging system - the Linkam shear cell.

The Linkam Shear cell is a device which consists of two parallel, concentric, transparent plates between which a fluid sample is placed. One of the plates is actuated by a motor, and is able to rotate about its axis such that the fluid experiences a deformation identical to what it would experience in a parallel plate rheometer. The Linkam shear cell allows for optical access through the plates, such that the movement of the fluid can be imaged using a microscope or a camera. A schematic diagram of the Linkam shear cell is show in Figure 4-16(b), while a photograph of the system is shown in Figure 4-16(a).

The Linkam shear cell was used to gain further insight into the evolution of the

microstructure formed by the wax precipitates under shear. Since the motor on the Linkam is able to impose a steady rotation rate on one of the plates, it is possible to obtain a different perspective on the type of flow behavior shown in Figure 4-14(b). Instead of seeing the how the velocity of the fluid varies along the gap height, a "top down" view of the flow can be observed. This essentially means that images obtained using the Linkam shear cell are oriented in the "1-3" plane instead of the "1-2" plane.

Figure 4-17 is an image showing a 10% wax oil system experiencing steady shear in the Linkam cell. The image looks very similar to those shown in Figure 3-5, and this is because the setup is placed between crossed polarizing filters - this allows the wax precipitates to show up as bright spots. In Figure 4-17 there are two regions of the image which are encircled by bounding boxes. The yellow region is dark, and thus contains no precipitates within it. It is therefore expected that this region will behave as a newtonian fluid. On the other hand the red region is a solid clump of wax crystallites which essentially acts as a rigid body i.e. it does not deform over time (but it does translate linearly and rotate). The arrangement of these clumps of crystallites is somewhat random, however over time they will break down and the average size of them will decrease. One would thus expect instances of plug-like flow profiles (which are due to the large clumps) to decrease over time as these fragments become smaller and smaller. This is consistent with what was observed for the 5% wax oil system undergoing a steady shear rate in Figures 4-14(c) and 4-14(b). Figure 4-14(c) in particular shows an initial plug-like flow at the 20 second mark, however at the 600 second mark the flow observed more closely resembles a linear profile (with some slip still present however).

The behavior described above is completely consistent with what is shown by Figure 4-14(b). Initially, flow of the gelled wax-oil starts out as pure slip - at this point the wax-oil sample located within the imaging plane consists of one very large solid piece of material. As time passes this piece of solid material breaks apart and forms smaller fragments. Therefore the velocity profile that is measured within the gap should approach a linear profile. The point at which it becomes a perfectly linear profile is the point at which the rigid fragments have become small enough

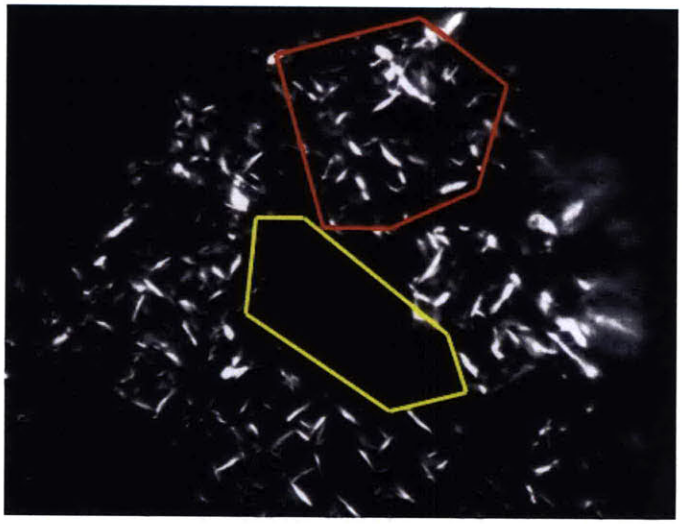

Figure 4-17: 10% wax-oil system experiencing shear in Linkam cell

such that the imaging system cannot resolve the motion of two different points on a single fragment. This cutoff size will be determined by image resolution and PIV interrogation window size. It should roughly scale as the size of one interrogation window, which for this particular system is typically 40 μm in size. In order to further the argument that the behavior shown by Figure 4-14(b) is due to breakdown of rigid fragments of wax precipitates, a metric was devised which quantifies how "fragmented" the flow is. This metric is represented by the letter Φ. Φ is determined by calculating the area between a linear velocity profile (which is given by $v_1 = \dot{\gamma} x_1$) and the measured velocity profile at a given moment in time. For a linear velocity profile, this area would be zero. The maximum area occurs when there is a plug-like flow profile. Φ is scaled by the maximum area so that it is a dimensionless parameter that spans the range $0 \leq \Phi \leq 1$. When $\Phi = 1$, we have a plug-like flow profile, and the material thus consists of one, or a few very large clumps. As Φ approaches zero, the flow profile approaches a linear profile, which corresponds to the point at which the clumps have become very small. The parameter Φ therefore behaves as a measure of the size of the fragments and of the flow heterogeneity. One interesting note to make is that the units of the unscaled value of Φ give a volumetric flow rate per unit depth. The way Φ is determined is shown in detail in Figure 4-18.

The computed value of Φ over time for the data in Figure 4-14(b) is shown in

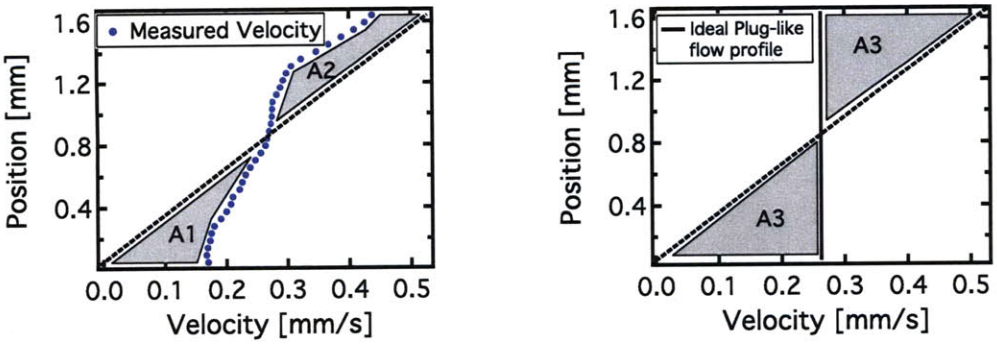

Figure 4-18: Diagrams that show how Φ is determined. For the velocity profile on the left hand side, Φ is given by $\frac{A1+A2}{2(A3)}$

Figure 4-19. As can be seen from the figure, the value of Φ actually fluctuates a large amount over short periods of time. However, the long term trend of the plot shows that Φ decreases in time. This measure of flow heterogeneity thus accurately represents what is occurring in the wax-oil sample. Some interesting things to note about the plot of Φ against time is that there is an initial time period where Φ is actually increasing. This is due to the fact that the sample initially experiences a uniform deformation within the bulk for a period of a second or so (as shown in Figure 4-15 and Figure 4-14(c)). The short term fluctuations of Φ can be attributed to the spatial heterogeneity of the sample. Since the imaging system is only observing a small portion of the entire sample, the overall heterogeneity of the entire sample is difficult to determine at a given particular time. Another interesting feature of this plot is that the peak value of Φ actually occurs at the same time when the stress imposed by the rheometer on the sample is at its maximum (at approximately 20s as shown in Figure 4-14(a)). The decrease in Φ following this first time period of 20 seconds indicates that the material fractures into smaller fragments. So, the material first experiences a finite strain within its bulk leading up to the maximum in Φ, followed by flow through slip and a fracturing behavior. This indicates that the wax-oil system goes through an elasto-plastic yielding transition in which the stress stops building up in the system and the strain continues to increase, up to the point where the material fractures.

In order to have a basis for comparison for plots such as those shown in Figure

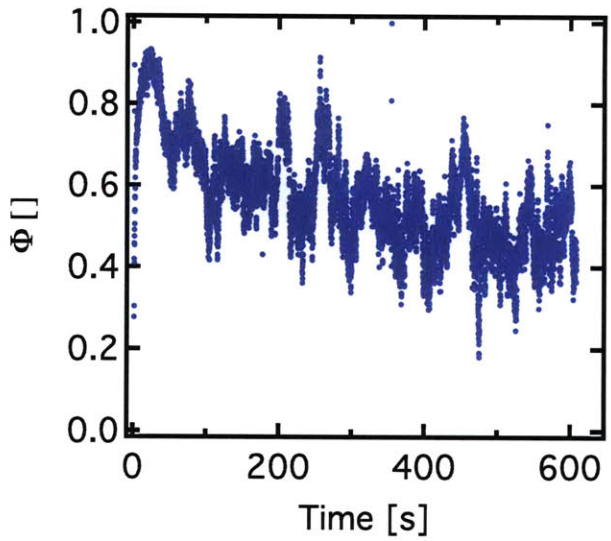

Figure 4-19: $\Phi(t)$ for the 5% wax oil system under steady shear rate ($\dot{\gamma} = 0.3\text{s}^{-1}$). Temperature was held constant at 27°C ($T_{wa} = 31$°C for this system).

4-19, it was important to carry out a control experiment in which the value of Φ is measured for a newtonian fluid undergoing steady shear. Following the definition for Φ that was given previously in this section, one would expect the measured value of Φ to be consistently equal to zero for the duration of the experiment. In order to show this, the heavy mineral oil (at a temperature of 27°C) was seeded with TiO_2 seed particles and a steady shear rate of $\dot{\gamma} = 0.3\text{s}^{-1}$ was imposed on the fluid for a period of 10 minutes (600 seconds).

The results shown in Figure 4-20 show that the measured value of Φ is zero for all times during the period of an imposed steady shear. Furthermore, as expected, the imposed stress is always constant. There are some points in the bottom plot where a non zero value of Φ is measured, however these arise due to the PIV software (Digiflow) producing bad velocity measurements for a particular frame. Also of significance is the space time diagram shown in Figure 4-20, which shows no changes in time and a gradual color variation along the vertical axis - this is characteristic of steady linear velocity profile.

In Figure 4-19 the value of Φ that was measured for the wax-oil system was during a period of a steady imposed shear rate. It is reasonable to expect the value of Φ over

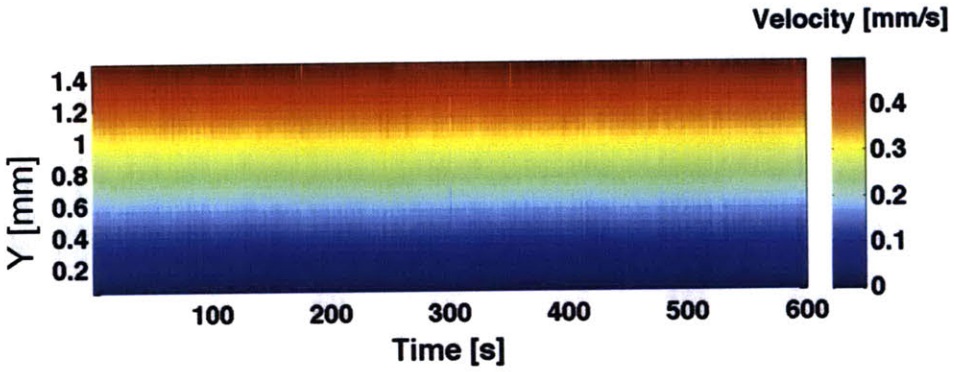

(a) Space-time diagram for the heavy oil under a steady shear rate

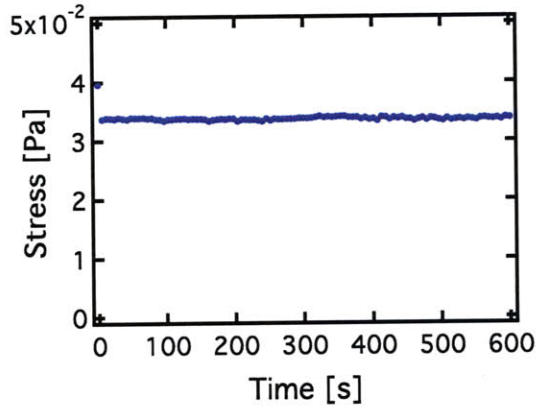

(b) Stress measurements from rheometer during steady shear imposed on the newtonian oil

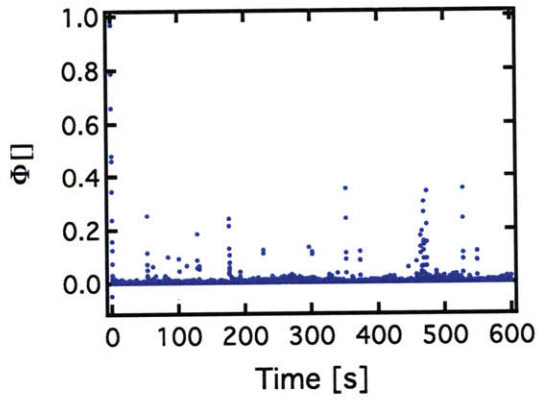

(c) Measured value of Φ for the newtonian oil during imposed steady shear

Figure 4-20: Control experiment showing the measured value of Φ for a Newtonian fluid undergoing steady shear. As expected, the measured value is consistently zero, with some fluctuations due to erroneous velocity profiles produced by the PIV software.

a given period of time to change depending on the value of the imposed shear rate. Observations made using the Linkam shear cell indicated that the clumps of wax precipitates break down faster when the rotation speed of the plate is increased. For this reason it is instructive to investigate how the value of the shear rate, $\dot{\gamma}$, influences the variations of the velocity profiles, as well as variations in Φ. In Figure 4-21, the bulk rheological data, space time diagram, and plot of $\Phi(t)$ are given for a 5% wax oil system undergoing steady shear, $\dot{\gamma} = 0.1s^{-1}$ over a period of 10 minutes. This experiment was done at a temperature of 27°C and the wax-oil system was treated with a thermal beneficiation step identical to the step used for the system represented by the data shown in Figure 4-19.

Once again, the space-time plot given in Figure 4-21(b) is difficult to interpret on its own. One thing that is clear from the plot is that the initial profiles which appear for the first 50 seconds are plug-like. There is also an initial deformation of the sample within its bulk during the first second, which looks similar to what was shown in Figure 4-15. This deformation is an initial elastic loading which occurs in the material, resulting in a total accumulated strain $\gamma \sim 0.1$. After this initial deformation and the slip behavior that follows it, the shear rate within the bulk begins to increase - this is even more apparent when looking at the decrease in the value of Φ between 100s and 200s. However, after 300 seconds the flow behavior in the space-time plot appears to take on an erratic behavior.

Figure 4-21(c) is helpful in understanding the erratic behavior shown by Figure 4-21(b). At the 300 second mark, there is a sudden jump in the value of Φ, which indicates that the profile has suddenly shifted to a plug-like profile. The value of Φ then fluctuates by decreasing, and increasing to almost 1 at the 400 second mark. These fluctuations appear to be occurring at a frequency much lower than the fluctuations which were observed in Figure 4-19. The reason for this is that at this lower apparent shear rate the material is moving at slower velocity, and hence the clumps of precipitates pass by the imaging window of the PIV system at a slower speed. Thus, it is possible to observe plug-like flow profiles, or linear velocity profiles for longer periods of time. Overall, these fluctuations are consistent with a slower break down,

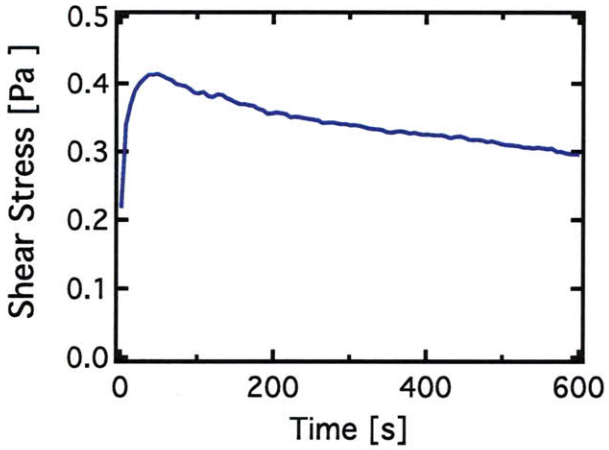

(a) Stress imposed on the 5% wax-oil sample over a period of 10 minutes. The shear rate is held constant at 0.1s^{-1}

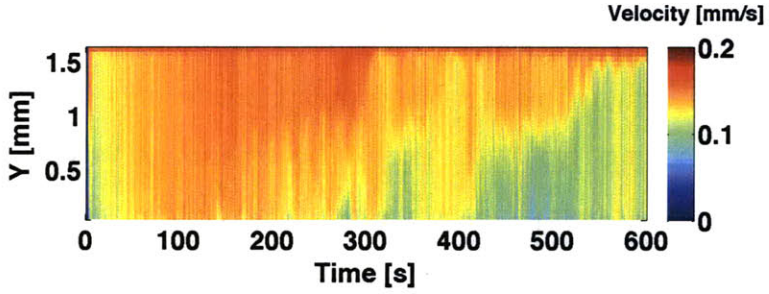

(b) Space-time diagram of the velocity within the sample while undergoing a shear rate of 0.1s^{-1}. Time axis corresponds to time axis in stress plot

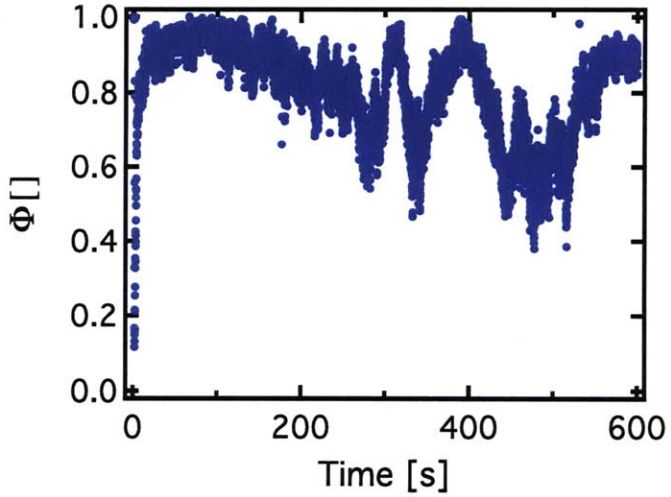

(c) Plot of $\Phi(t)$ over period of 10 minutes

Figure 4-21: Spatiotemporal plot, rheological data and plot of $\Phi(t)$ for a 5% wax oil sample undergoing steady shear, $\dot{\gamma} = 0.1s^{-1}$. Temperature was held constant at 27°C ($T_{wa} = 31$°C for this system).

or erosion of the rigid fragments of wax precipitates at lower shear rates.

Another observation which can be made about the data shown in Figure 4-21(c) is that at the end of the experiment, the value of Φ is very close to 1. This might initially seem surprising, however if we consider the average speed of the wax-oil fragments, it is clear that we have yet to observe these fragments make a complete revolution about the axis of rotation of the cone and plate geometry. At the imaging plane, the size of the gap is 1.75mm. An imposed shear rate of 0.1s^{-1}, will therefore cause the top plate to move at a speed of $V_w = 0.175\text{mm/s}$. Because the imaging plane is at the edge of the 50mm cone and plate geometry, the solid fragments must travel a distance of $\pi \times 50\text{mm}$ in order to make a complete revolution and re-enter the imaging plane. The solid fragments on average travel at a speed that is approximately half the speed of the moving wall, V_w. Therefore, they require a time period of 1,800 seconds in order to re-enter the imaging plane. The full experiment only lasts a third of this time, so it is not surprising that at the end of the experiment we are still witnessing regions containing very large fragments passing in front of the imaging window.

4.3.2 Effect of Surface Roughness on Dynamics of Velocity Fields

So far, the data showing the evolution of flow profiles have been for the model wax oil system within a cone plate geometry, where the bottom surface is a smooth machined aluminum surface (root mean squared roughness $R_q \sim 0.1\mu\text{m}$), and the top surface is the quartz plate. In section 4.3 it was shown that the type of surface that the gelled system is in contact with can have a considerable effect on the behavior of the flow profile. For this reason, an experiment was conducted in which a steady shear rate ($\dot{\gamma} = 0.1s^{-1}$) was imposed on a gelled wax oil system cooled 27°C, just as in Figure 4.3.1. However, in this instance the bottom machined aluminum surface was replaced with a sandpaper coated surface. The sandpaper grains result in a root mean squared roughness $R_q \sim 30\mu\text{m}$, which is an order of magnitude larger than the roughness of the machined aluminum plate.

The data from this experiment is shown in Figure 4-23. This figure shows the bulk rheological data output from the rheometer, as well as the space time plot illustrating evolution of the velocity profile. The value of Φ determined from this space time plot is also shown in Figure 4-23(c). One thing to note about Figure 4-23(a), is that the peak value of the stress attained at the 25 second mark, is close to being double the applied stress peak shown in Figure 4-21(a). This is consistent with the data shown in Figure 4.3, where the roughened bottom surface resulted in the same applied stress leading to a smaller deformation. This factor of two can be rationalized when the space time plot for the period of increasing stress is studied. The space time plot in Figure 4-23(b) shows that initially the velocity within the bulk of the fluid is uniformly zero. Thus, the deformation that the rheometer is registering is only due to slip on the top surface! Now that the bottom surface is roughened, the gelled wax-oil sticks to this surface and slips against the top smooth surface. As a result, the slip velocity at the top surface is now larger than it was determined to be in Figure 4-21(b). While the detailed slip constitutive law for this type of fluid is unknown, it is reasonable to suggest that the slip law describing flow of the fluid over the top surface follows a roughly linear relationship to shear stress. Hence, a larger stress is required for the rheometer to impose the same apparent deformation. In fact, this shear stress would need to be larger by a factor of about two to impose the same apparent deformation if all of the slip was happening on the top surface, instead of it being distributed among the top and bottom surface. The effect of roughening the bottom surface on the slip velocities is also shown schematically in Figure 4-22. A velocity profile where slip only occurs at the top surface is also shown in Figure 4-24.

The bottom surface is successful in preventing slip for the entirety of the experiment. Figure 4-23(b) shows that the velocity near the bottom surface is always zero, while there are considerable fluctuations in the velocity far from this surface. Once again, these velocity variations are erratic, resulting in the flow profile alternating between plug-like and linear like profile. For this reason it is helpful to turn to the plot of Φ versus time in order to understand these variations. This plot (Figure 4-23(c)) shows that the value of Φ initially jumps to a value which is almost equal to

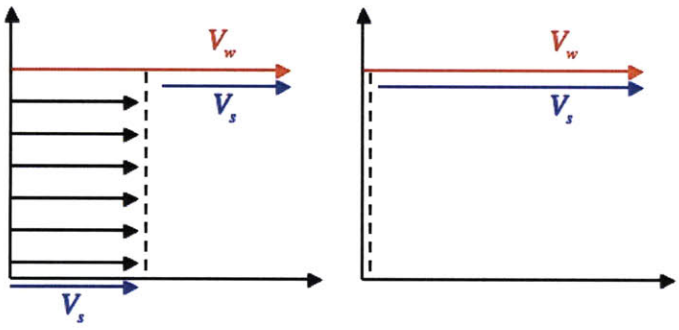

Figure 4-22: Schematic diagram showing the difference between two types of plug-like flow. In the diagram shown on the left, the material moves at a bulk velocity which is half of the wall velocity, V_w. In such an instance, the slip velocities at the top and bottom surface are the same. In the diagram on the right, the bottom surface is roughened and this prevents any slip from occurring on that surface. Since the wall velocity is the same (V_w), the slip velocity at the top surface must now be twice what it was before.

1 at short times. Then, over a period of approximately 200 seconds, this measure of heterogeneity drops to a value around $\Phi \approx 0.4$. The local flow behavior at this point has approached a linear profile. After the 200 second mark, Φ appears to increase, and then starts to drop again at the 450 second mark.

This fluctuating behavior of Φ over time again points to a limitation in our imaging system - which is that it only observes flow profiles at a small region within the entire sample. As a result, these fluctuations are due to regions of gelled and ungelled material passing in front of the imaging plane. However, one thing that is clear from the Figure 4-23(c) is that the average vale of Φ over this period of time is smaller than the average value of Φ for Figure 4-21(c). This suggests size of gelled fragments, as determined from Φ, actually decreases faster for when the sample is in contact with this roughened surface. Thus, it appears that the rigid fragments of wax precipitates break down quicker for roughened surfaces. The effect of boundary roughness on the "erosion" of a gelled system is similar to what was observed by Gibaud studying laponite dispersions [19]. This may not be very surprising when one considers the energy that is dissipated into the system over the period of time that spans the experiment. As stated previously, the different slip characteristics at the surfaces resulted in a larger stress being required to impose the same apparent deformation.

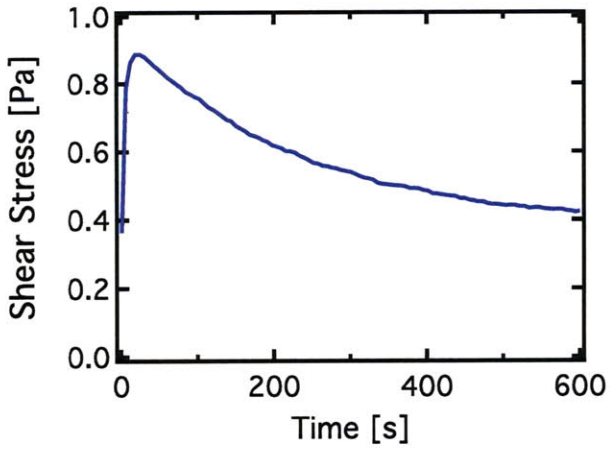

(a) Stress imposed on the 5% wax-oil sample over a period of 10 minutes. The shear rate is held constant at $0.1s^{-1}$

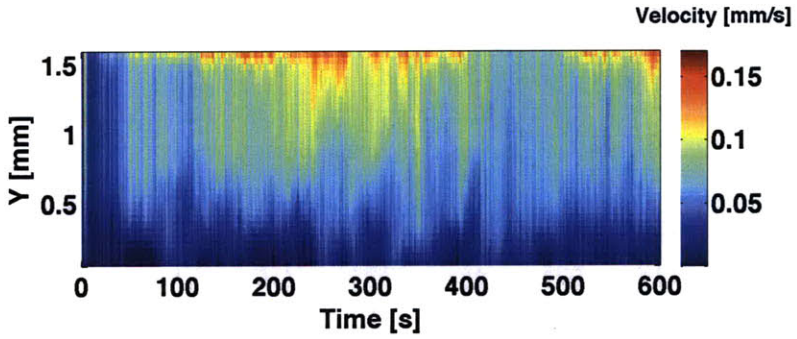

(b) Space-time diagram of the velocity within the sample while undergoing a shear rate of $0.1s^{-1}$. Time axis corresponds to time axis in stress plot

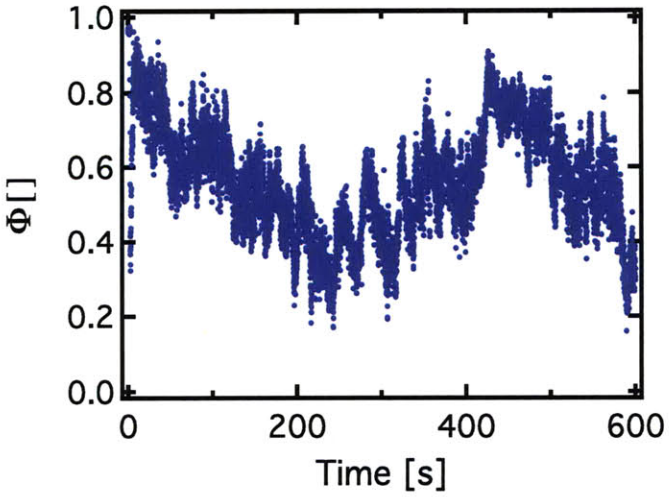

(c) Plot of $\Phi(t)$ over period of 10 minutes

Figure 4-23: Spatiotemporal plot, rheological data and plot of $\Phi(t)$ for a 5% wax oil sample undergoing steady shear, $\dot{\gamma} = 0.1s^{-1}$. In this case the bottom surface is roughened (sandpaper with grain size $\sim 30\mu$m). Temperature was held constant at 27°C ($T_{wa} = 31$°C for this system)

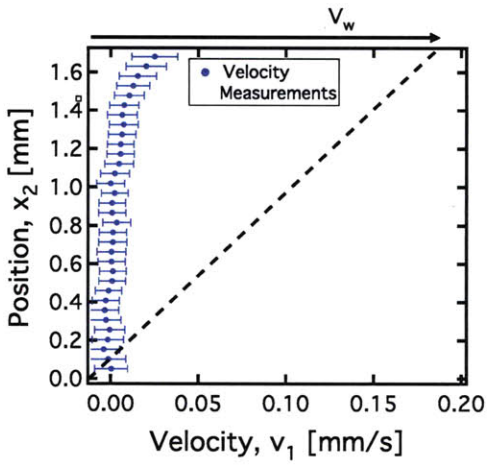

Figure 4-24: Velocity profile within wax-oil system 10 seconds after the initial steady shear rate is imposed by the top plate. As can be seen from the plot, the velocity within the bulk is generally zero, and there is a slip velocity equal to the wall velocity (V_w) on the top surface. There is no slip on the bottom surface

If one calculates the volumetric rate of energy being dissipated for these two cases, then it turns out that more energy is dissipated into the sample which is in contact with the bottom roughened surface (this is because $\dot{\gamma}$ is the same in both cases, but for one instance τ is higher than the in other). The volumetric rate of energy dissipation $\dot{E}$, as well as the total energy dissipated into the system, E is given in the equations below.

$$\begin{aligned} \dot{E} &= \sigma(t)\dot{\gamma}(t) \\ E &= \int_0^t \sigma(t)\dot{\gamma}(t)dt \end{aligned} \tag{4.14}$$

Another interesting observation to make is that while the imposed stress shown in Figure 4-23(a) is larger than the imposed stress shown in Figure 4-21(a), the stress actually drops faster in the case of Figure 4-23(a) (and the two look as if they are approaching the same value). This suggests that as time progresses, the end state of the wax-oil system is very similar in the two cases and has values of viscosity which are close to each other. A comparison of the stress-time curves for the two experiments is shown in Figure 4-25. In addition to this, the cumulative amount of energy dissipated into the two systems as a function of time is shown in Figure 4-26.

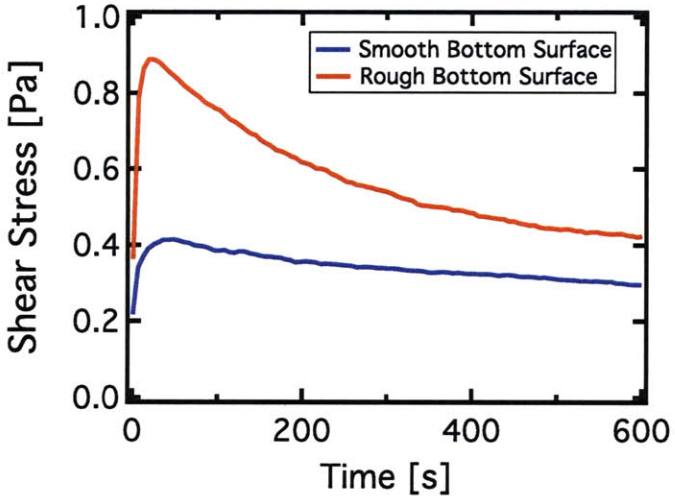

Figure 4-25: Comparison of rheometer stress data for $\dot{\gamma} = 0.1s^{-1}$ experiment on roughened and smooth bottom surface. Both experiments are done at a constant temperature of 27°C ($T_{wa} = 31$°C for this system)

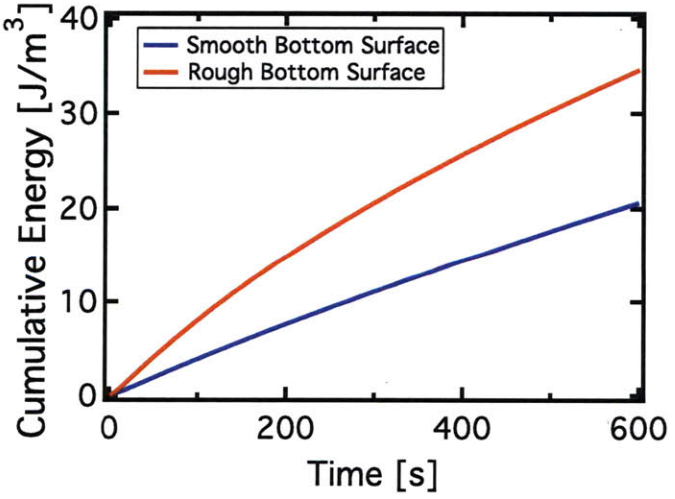

Figure 4-26: Cumulative energy dissipated (E) for the 5% wax oil system under a steady imposed shear rate of $\dot{\gamma} = 0.1s^{-1}$. As can be seen from the data, when the system is in contact with the lower roughened geometry, the total amount of energy that is dissipated into the system is higher. This is the cause for the faster drop in Φ.

In this section, the effects of surface roughness on the yielding behavior of the model wax oil system have been discussed. It was shown that the wax oil system can exhibit two distinct types of yielding behavior - yielding through interfacial wall slip and yielding within the bulk of the material. Which one of these behaviors that the system exhibits depends on the type of surface that it is in contact with. Furthermore, the evolving dynamics of velocity profiles for the wax-oil system under steady shear were studied. The parameter Φ was developed which serves as a means to quantify heterogeneity in the flow, as well as the overall size of the solid-like gelled fragments. It was shown that generally the size of these fragments decrease in time under a steady imposed shear, and the rate of decrease is faster for higher shear rates. This was related to the rate of volumetric energy dissipation and it was shown that when the system is in contact with a roughened surface, a higher stress is required to impose the same apparent shear rate, resulting in a higher energy dissipation. This higher rate of dissipation leads to a faster drop in the value of Φ.

Chapter 5

Conclusion

To summarize the work done in this thesis, a model wax-oil system was introduced in order to understand a class of yielding materials that exhibits rheological behavior similar to actual waxy crude oils. The rheology of this system was studied through a combined application of traditional rheological measurements, as well as through the use of direct measurements which can determine the local kinematics of the model fluid. The use of this combined Rheo-PIV approach to study the model waxy crude oil is termed "Flow Assurance Rheometry".

The bulk rheology of the fluid was shown to agree well with some of the qualitative behavior shown for actual waxy crude oils in the literature. Specifically, the model system exhibits a sudden change in its viscosity below the temperature at which wax precipitates form (T_{wa}), and the fluid can be described as a yield stress fluid when its temperature is below T_{wa}. The value of the yield stress was shown to depend on temperature, i.e. $\sigma_y = \sigma_y \left(\frac{T}{T_{wa}}\right)$. These values were quantified in Chapter 4 in Table 4.1.1 and in Chapter 3 in Table 3.1.2. In addition to this, the model system was shown to exhibit irreversible changes in the microstructure when the yield stress, σ_y is exceeded. Birefringence Imaging of the microstructure formed by wax crystallites was able to provide insight into the causes of this irreversible behavior. Large amplitude oscillatory shear (LAOS) has also been used to characterize the model wax-oil system. A framework previously developed by Ewoldt [13] was used that relates higher order Chebyshev/Fourier coefficients in the material stress response to non-linear behavior

such as strain stiffening/softening and shear thickening/thinning. The data from the LAOS experiments indicated that the model fluid's behavior transitions from linear viscoelastic solid at low strains ($\gamma_0 \sim 0.1\%$), to a strain stiffening viscoelastic solid at intermediate strains ($\gamma_0 \sim 2\%$), and then the fluid exhibits viscoplastic behavior at large strains ($\gamma_0 > 10\%$)

Further insight was gained into the effective rheology of the model fluid and its role in controlling flow assurance through the use of the velocimetric measurement system. This system was developed in order to directly observe deformation within a sample undergoing shear in the rheometer. The design of this system was described in detail in Chapter 3, as well as how certain artifacts such as image distortion were corrected for. It was also shown that this apparatus was able to determine the velocity profile of a Newtonian fluid undergoing homogenous steady shear flow within the rheometer. The minimum resolvable displacement between frames for the system was shown to be 0.37μm, which indicates the precision of these measurements. Also, the temporal resolution of velocity measurements were typically 40μm. The new capabilities gained with the Rheo-PIV system were used to study the flow of the gelled wax-oil system at $\frac{T}{T_{wa}} < 1$ within the confines of the rheometer geometry.

The gelled wax oil system was shown to exhibit a complex spatiotemporal response to an imposed apparent shear rate. The system initially exhibits a plug-like flow profile, which is the result of interfacial slip on the solid surfaces that it is in contact with. However, this behavior changes over the course of time - the flow profile begins to more closely resemble a homogenous shearing profile which increases linearly across the gap (or along the x_2 direction). By devising a global metric which quantifies the degree of heterogeneity of gelled fragments within the sample (Φ), it was possible to show that this complex behavior agreed with previous observations made using the Linkam shear cell, which shows progressive fragmentation of rigid gelled sections into smaller clumps. We have also documented the dependence of this response to the surface roughness of the solid surface the gel is in contact with. By using a roughened geometry, it was possible to prevent slip on one of the surfaces. This had the effect of a resulting faster drop in Φ, and thus a quicker fragmentation process. The root

mean squared roughness (R_q) of the two types of surfaces were measured $\sim 0.1\mu$m for the smooth surface, and $\sim 30\mu$m for the rough surface. The rougher surface has a value of of $R_q \sim \ell$, where ℓ is the characteristic size of wax precipitates observed for the particular wax oil system. It was thus shown that slip can be avoided by utilizing surfaces for which $R_q \gtrsim \ell$. These results have an immediate bearing on pipeline design for the transportation of waxy-crude, and emphasize the importance of accounting for surface interactions in models which describe the rheology of waxy crude oil.

These results have elucidated several new types of thermorheological behavior that these wax-oil systems exhibit under flow. At temperatures below their wax appearance temperature ($T < T_{wa}$), these systems can now be understood as consisting of initially large, solid-like fragments which are able to experience a small elastic deformation before breaking apart and undergoing plastic flow. If the material undergoes a continuous shearing, these fragments break down into progressively smaller pieces over time. Furthermore, there are no strong attractive or repulsive forces between the fragments, because their size is large enough such that they are non-Brownian. The timescale for brownian diffusion, based on $\tau = \frac{a^3\mu}{k_bT}$, was shown to be on the order of weeks in Chapter 3. The crystallites in the fluid therefore do not reform into larger fragments after they have been broken down, so any yielding transition that they experience is irreversible.

Future work that would build on the results in this thesis will likely involve developing a new model fluid that is more representative of actual crude oils encountered in production scenarios. There are three possible routes which could be taken for developing a new model fluid. The first would involve the formulation of a wax-oil mixture which contains a different distribution of n-paraffins in the wax part. This distribution would have a wider range of n-paraffins, such that the temperature difference between the wax appearance temperature (T_{wa}) and the gelation temperature (T_{gel}) is much larger than it is for the current model fluid. With such a model system it would be possible to probe the rheology of a precipitate containing fluid that is between these two temperatures. This temperature regime is of interest because

waxy-crude is often transported in pipelines at these temperatures.

The second route for formulating a new model fluid would involve the development of a wax-oil-water emulsion. Such an emulsion would be similar to the crude oil emulsions studied by Visintin [48], and the work would be focused on understanding how wax can stabilize oil-water emulsions, as well as the effects this may have on the bulk rheology of the fluid. The third and final type of model fluid for which there is interest studying would be a model fluid containing gas hydrates. Gas hydrates typically form at high pressures in crude-oils, so rheological experiments would either involve a high-pressure test cell or develop a hydrate system that would be able to form at atmospheric pressures.

The current set of experimental results can provide a sufficient basis for development of a new constitutive model that will be capable of describing the complex thermorheological behavior of waxy crude oils. The experiments in this thesis have also shown that wall slip and interactions between the wax-oil gel and solid surfaces play an important role in transport scenarios. It is therefore important that these new constitutive models account for this behavior. Current constitutive equations such as those introduced by Pedersen [35] are certainly lacking in this aspect.

One last future step would be to transition the methodologies developed in this thesis for Flow Assurance Rheometry to industrial scale laboratory facilities. The Rheo-PIV approach used in this thesis has uncovered behavior exhibited by the simple model fluid that was previously difficult to observe. As a result of this, it the application of the methodologies of Flow Assurance Rheometry to more complicated fluids would likely be a fruitful endeavor.

Appendix A

Supplementary Data

A.1 Determining T_{wa} Using DSC

The hydrophobic nature of both the mineral oil and the wax allows small amounts of wax to remain as a solute in the mineral oil. The amount of wax which remains in a solute form, and has not yet precipitated out of the solution, depends on the temperature of the fluid. Hence, it is possible to use DSC (Differential Scanning Calorimetry) to determine the percentage of wax precipitated for a model wax-oil system. A DSC curve showing wax precipitated vs. temperature for a 10% wax oil system is shown in A-1. As can be seen, at temperatures above 34°C no wax is precipitated. Furthermore, the entire amount of wax that is initially mixed in with the mineral oil does not precipitate even at rather low temperatures (< 10°C). The temperature at which wax precipitates first begin to form is denoted as the wax appearance temperature, or T_{wa}. Obtaining a DSC curve is another method through which T_{wa} can be determined. The particular DSC curve shown in Figure A-1 gives a value of $T_{wa} = 35$°C, which is 1°C lower than the value determined from Figure 3-4 and shown in Table 3.1.2

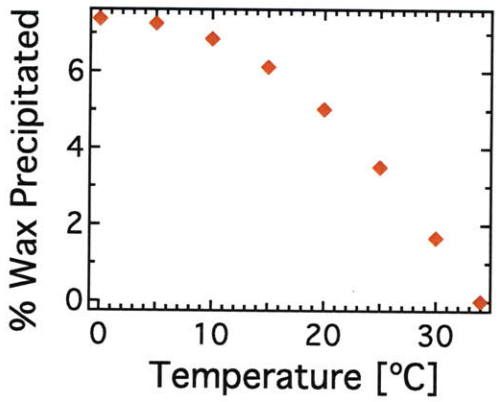

Figure A-1: Gas chromatography data showing the wt.% distribution of n-paraffin carbon number for the mineral oil (top plot) and paraffin wax (lower plot). The wax has a higher per-weight percentage of larger n-paraffins.

A.2 Roughness measurements using Zygo Interferometer

In order to accurately quantify the difference in roughness between the "roughened" and "smooth" surfaces which were utilized in the steady shear rate experiments in section 4.3, a Zygo interferometer was used to measure the roughness of the machined bottom aluminum cone. Figure A-2 shows the topography of the machined cone for a 0.9mm×0.7mm section (which is the "smooth" surface used in experiments). As can be seen from the figure, there are alternating circular grooves, which are a result of the fabrication process which was used to produce the bottom cone (namely turning the piece in a lathe). This topography was used to calculate the roughness values R_a and R_q along two different directions.

The roughness value R_q is simply the arithmetic average of absolute values of height relative to the average for each point along a particular line. The parameter R_a is one particular method which can be used to quantify roughness of a surface. Another parameter is R_q, which is the root mean squared of the height values. The values of R_a and R_q naturally depend on the line which is used to draw a surface profile, especially since topographies such as those shown in A-2 can be irregular. Due to this reason, the values of R_q and R_a were measured both along a line which

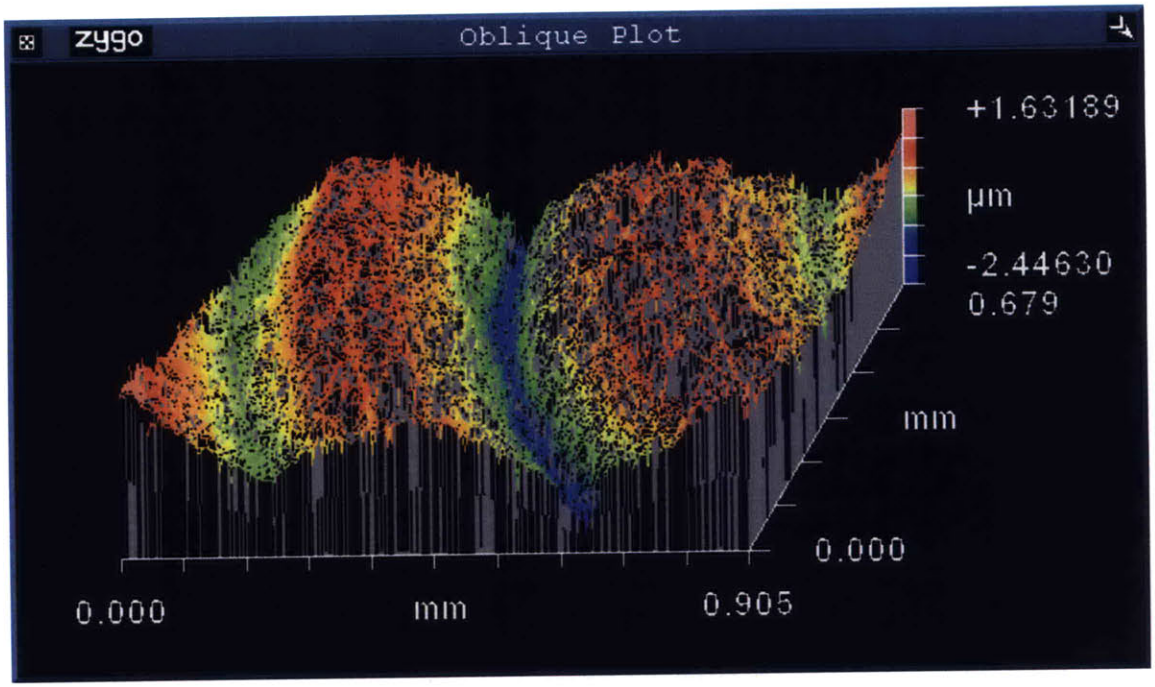

Figure A-2: Topography of machined aluminum cone for a 0.9mm×0.7mm area. Alternating circular grooves (or peaks and troughs) can be seen - these are a result of the machining process, where the geometry is cut on a lathe.

was taken going *across* the peaks and troughs, and along a line going *along* a peak. The values of R_q and R_a are 0.109μm and 0.063μm respectively for a line taken along a peak. On the other hand, these values are somewhat larger when they are determined for a line going across the peak - they are measured as $R_q = 0.605\mu$m and $R_a = 2.727\mu$m in this particular instance. Figures A-3 and A-4 show the surface profiles along each of these lines and where these lines are on the surface topography.

The "roughened" surface which was used in the experiments was a 320 grit sandpaper surface. Due to the nature of this surface, it was not possible to use the Zygo interferometer to obtain an accurate measure of the R_a and R_q parameters. However, the manufacturer specifies an average grain size of 46.2μm for this particular grit. While the exact topography of the surface was not measured or imaged, it is possible to assume a topography which varies sinusoidally along a line, with an average amplitude of 46.2μm. This idealized surface would have an R_a value of 29.4 μm and an R_q value of 32.7 μm

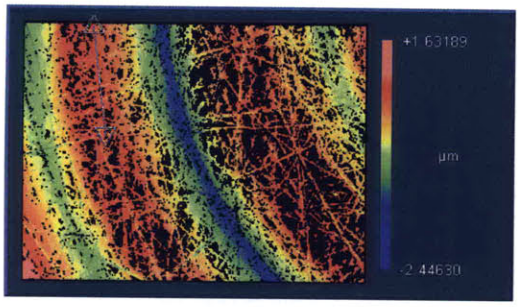

(a) Surface plot

(b) Line plot

Figure A-3: Surface roughness of the machined aluminum bottom cone which was fabricated for use with the PIV system. Figure A-3(a) indicates where a line is drawn in order to obtain the data plotted in figure A-3(b). In this particular instance the line is drawn along a peak. From the plot in figure A-3(b), it is possible to determine the values of R_q and R_a, which are 0.109μm and 0.063μm respectively

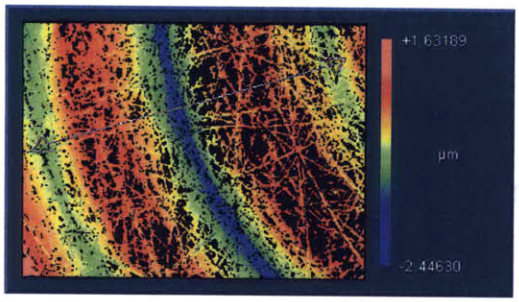

(a) Surface plot

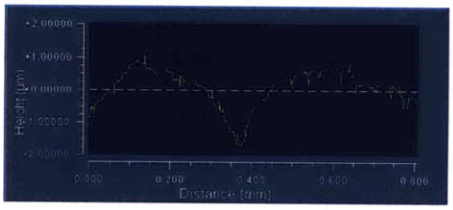

(b) Line plot

Figure A-4: Surface roughness of the machined aluminum bottom cone which was fabricated for use with the PIV system. Figure A-3(a) indicates where a line is drawn in order to obtain the data plotted in figure A-3(b). In this particular instance the line is drawn across the peaks and troughs. From the plot in figure A-3(b), it is possible to determine the values of R_q and R_a, which are 0.605μm and 2.727μm respectively

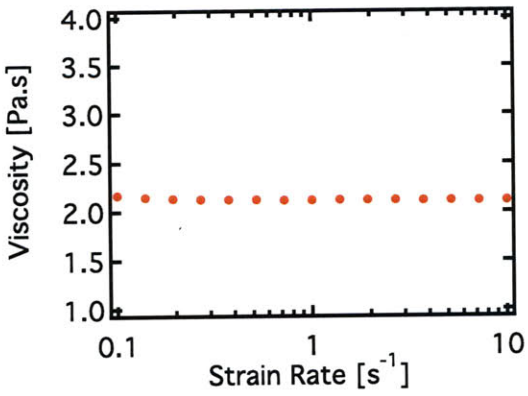

Figure A-5: Viscosity measurement of the N1000 calibration oil at a range of shear rates, using the custom fabricated 50mm lower cone geometry. As expected, viscosity is constant at a value of 2.1Pa.s

A.3 Calibration Experiments for Lower Cone Geometry

In section 3.2.1 the design for a lower cone geometry was described. This lower cone was custom fabricated to be compatible with the 50mm upper quartz plate which was used for all experiments involving the PIV system. In order to verify that the cone was fabricated to the correct specifications, a series of experiments were carried which measured the rheology of a newtonian calibration oil. The calibration oil that was used was a N1000 high viscosity calibration oil, from Cannon Instruments. The viscosity (specified by the manufacturer) of the oil is 2.008 Pa.s at 25°C. The 50mm upper quartz/lower cone geometry combination was used to measure this viscosity at a range of shear rates from $0.1s^{-1}$ to $10s^{-1}$. The viscosity measurements are given in figure A-5. The plot shows that the viscosity measured is the same for all shear rates, and was measured as 2.1Pa.s. This is within 5% of the manufacturer's specified viscosity.

Small amplitude oscillatory shear (SAOS) measurements were also carried out on the calibration oil using the particular cone-plate geometry configuration. The value of G'' was probed for angular frequencies ranging from $\omega = 0.1s^{-1}$ to $\omega = 10s^{-1}$ - this data is shown in figure A-6. Another possible method to determine the viscosity of a

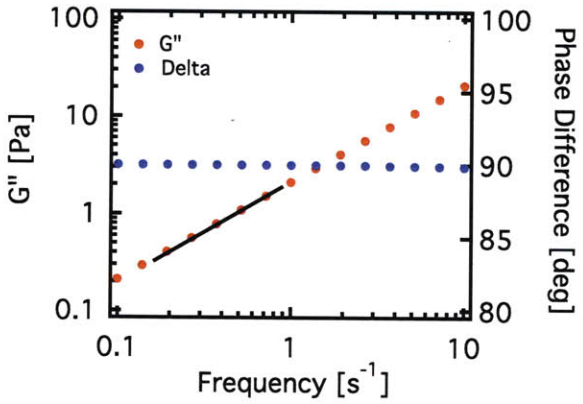

Figure A-6: Measurement of $G''(\omega)$ for a range of frequencies for the N1000 calibration oil. On a log-log scale the G'' data form a straight line, with a slope equal to the viscosity of the fluid - this is as expected for a Newtonian fluid. The slope is indicated by the thick black line. Phase angle of measurements is shown, which is measured as 90°.

newtonian fluid is to measure the slope of the $G''(\omega)$ curve. This was carried out for the particular data and it was found that the viscosity agreed with the measurements in A-5 - it was measured as 2.1Pa.s.

The viscosity measured in these calibration experiments was 5% larger than the value specified by the manufacturer. There are several possible sources for this error. One possible source is the lower geometry not being fabricated to the exact specifications of the design. The diameter of the lower geometry is machined to within 10μm, so this is not a source of error which would cause the 5% offset. However, since the angle specified in the cone design is small (only 4°), any deviation from this specification could result in a considerable error in measurements. For a cone-plate rheometer, viscosity is determined from torque measurements and angular velocity using the following equation.

$$\eta = \frac{\tau_{\theta\phi}}{-\dot{\gamma}_{\theta\phi}} = \frac{3\mathcal{T}\Theta}{2\pi R^3 W} \tag{A.1}$$

From equation A.1 it is apparent that any errors in the cone angle Θ are propagated into the measurements of viscosity. Using this equation it is possible to calculate the "corrected" cone angle from the measurements of viscosity which are given in figure A-5. For this calculation the viscosity of the calibration oil is assumed to be what

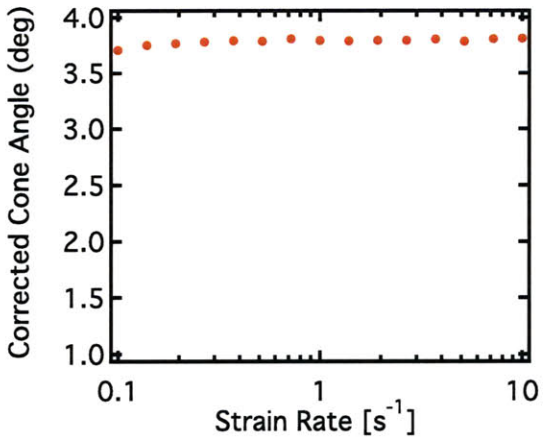

Figure A-7: Plot showing the corrected cone angle as a function of shear rate. This corrected angle is determined by assuming that the viscosity of the calibration oil is exactly that specified by the manufacturer, and then using equation A.1 to calculate the value Θ.

is specified by the manufacturer (2.008 Pa.s), while the torque $\mathcal{T}$ and angular velocity W are those measured for the plot in A-5. A plot of the corrected cone angle vs. the shear rate can then be obtained. This plot is shown in A-7.

The data in figure A-7 shows that the corrected cone angle is actually less (5% less than 4°) than the specified angle in the design. It is reasonable to expect this type of error in the angle machined into the cone, since it was not manufactured on a CNC lathe.

Bibliography

[1] J. M. Adams and P. D. Olmsted. Nonmonotonic Models are Not Necessary to Obtain Shear Banding Phenomena in Entangled Polymer Solutions. *Physical Review Letters*, 102(6), Feb 2009.

[2] R. J. Adrian. Particle-Imaging techniques for experimental fluid-mechanics. *Annual Review of Fluid Mechanics*, 23:261–304, 1991.

[3] P. Ballesta, R. Besseling, L. Isa, G. Petekidis, and W. C. K. Poon. Slip and Flow of Hard-Sphere Colloidal Glasses. *Physical Review Letters*, 101(25), DEC 19 2008.

[4] H. A. Barnes. A review of the slip (wall depletion) of polymer solutions, emulsions and particle suspensions in viscometers: its cause, character, and cure. *Journal of Non-Newtonian Fluid Mechanics*, 56(3):221–251, 1995.

[5] H. A. Barnes. Thixotropy - A review. *Journal of Non-Newtonian Fluid Mechanics*, 70(1-2):1–33, May 1997.

[6] R. B. Bird, R. C. Armstrong, and O. Hassager. *Dynamics of Polymeric Liquids Vol. 1.* John Wiley and Sons, second edition, 1987.

[7] K. Breuer. *Microscale Diagnostic Techniques*, section 2.5.3, pages 70–73. Springer, 2005.

[8] C. J. Campbell and J. H. Laherrere. The end of cheap oil. *Scientific American*, 278(6), 1998.

[9] C. Chang and D. V. Boger. Yielding of waxy crude oils. *Industrial and Engineering Chemistry*, 37:1551–1559, 1998.

[10] W. C. Chin. Modern flow assurance methods: clogged pipelines, wax deposition, hydrate plugs. *Offshore*, 60(9):92, 2000.

[11] P. Coussot, L. Tocquer, C. Lanos, and G. Ovarlez. Macroscopic vs. local rheology of yield stress fluids. *Journal of Non-Newtonian Fluid Mechanics*, 158(1-3, Sp. Iss. SI):85–90, May 2009.

[12] MR Davidson, QD Nguyen, C Chang, and HP Ronningsen. A model for restart of a pipeline with compressible gelled waxy crude oil. *Journal of Non-Newtonian Fluid Mechanics*, 123(2-3):269–280, Nov 10 2004.

[13] R. H. Ewoldt, A. E. Hosoi, and G. H. McKinley. New measures for characterizing nonlinear viscoelasticity in large amplitude oscillatory shear. *Journal of Rheology*, 52(6):1427–1458, Nov 2008.

[14] Randy H. Ewoldt, Peter Winter, Jason Maxey, and Gareth H. McKinley. Large amplitude oscillatory shear of pseudoplastic and elastoviscoplastic materials. *Rheological Acta*, 49(2):191–212, FEB 2010.

[15] American Society for Testing Materials. ASTM Standard D287-92, Standard Test Method for API Gravity of Crude Petroleum and Petroleum Products (Hydrometer Method), 2006.

[16] American Society for Testing Materials. ASTM Standard D97-09, Standard Test Method for Pour Point of Petroleum Products, 2009.

[17] G. G. Fuller. *Optical Rheometry.* Oxford University Press, 1995.

[18] P. Gao, J. Zhang, and G. Ma. Direct image-based fractal characterization of morphologies and structures of wax crystals in waxy crude oils. *Journal of Physics - Condensed Matter*, 18(50):11487–11506, Dec 2006.

[19] T. Gibaud, C. Barentin, and S. Manneville. Influence of boundary conditions on yielding in a soft glassy material. *Phys. Rev. Lett.*, 101(25):258302, Dec 2008.

[20] T. Gibaud, C. Barentin, N. Taberlet, and S. Manneville. Shear-induced fragmentation of laponite suspensions. *Soft Matter*, 5(16):3026–3037, 2009.

[21] F. Gill and R. J. Russell. Pumpability of residual fuel oils. *Industrial and Engineering Chemistry*, 46(6):1264–1278, 1954.

[22] Ahmed Hammami and John Ratulowski. Precipitation and deposition of asphaltenes in production systems: A flow assurance overview. In *Asphaltenes, Heavy Oils, and Petroleomics*, pages 617–660. Springer New York, 2007.

[23] K. A. Hayes, M. R. Buckley, I. Cohen, and L. A. Archer. High Resolution Shear Profile Measurements in Entangled Polymers. *Physical Review Letters*, 101(21), Nov 2008.

[24] K. A. Hayes, M. R. Buckley, I. Cohen, and L. A. Archer. Nonlinear rheology of entangled polymer solutions in narrow gaps probed by confocal microscopy. In Co, A and Leal, LG and Colby, RH and Giacomin, AJ, editor, *XVTH International Congress on Rheology - The Society of Rheology 80th Annual Meetings, Pts 1 and 2*, volume 1027 of *AIP Conference Proceedings*, pages 394–396, 2 Huntington Quadrangle, STE 1NO1, Melville, NY 11747-4501 USA, 2008. Soc Rheol, Amer Inst Physics. 15th International Congress on Rheology/80th Annual Meeting of the Society-of-Rheology, Monterey, CA, AUG 03-08, 2008.

[25] M. K. Hubbert. Energy From Fossil Fuels. *Science*, 109(2823):103–109, 1949.

[26] N. B. Joshi, M. Muhammad, Creek J., and J. McFadden. Flow assurance: A challenging path to well completions and productivity. In *Offshore Technology Conference, 5 May-8 May 2003, Houston, Texas*, Offshore Technology Conference, 2003.

[27] M. Kanè, M. Djabourov, J.-L. Volle, J.-P. Lechaire, and G. Frebourg. Morphology of paraffin crystals in waxy crude oils cooled in quiescent conditions and under flow. *Fuel*, 82:127–135, 2002.

[28] R. G. Larson. *The Structure and Rheology of Complex Fluids.* Oxford University Press, ninth edition, 1999.

[29] H. S. Lee, P. Singh, W. H. Thomason, and H. S. Fogler. Waxy oil gel breaking mechanisms: Adhesive versus cohesive failure. *Energy and Fuels*, 22(1):480–487, 2008.

[30] PF Luckham and S Rossi. The colloidal and rheological properties of bentonite suspensions. *Advances in Colloid and Interface Science*, 82(1-3):43–92, Oct 1999.

[31] S. P. Meeker, R. T. Bonnecaze, and M. Cloitre. Slip and flow in pastes of soft particles: Direct observation and rheology. *Journal of Rheology*, 48(6):1295–1320, 2004.

[32] P. Moller, A. Fall, V. Chikkadi, D. Derks, and D. Bonn. An attempt to categorize yield stress fluid behavior. *Phil. Trans. R. Soc. A*, 367(1909):5139–5155, 2009.

[33] A. Mourchid, A. Delville, Lambard J., E. Lecolier, and P. Levitz. Phase-diagram of colloidal dispersions of anisotropic charged-particles - equilibrium properties, structure, and rheology of laponite suspensions. *Langmuir*, 11(6):1942–1950, Jun 1995.

[34] F. W. Padgett, D. G. Hefley, and A. Henriksen. Wax crystallization - a preliminary report. *Industrial and Engineering Chemistry*, 18(8):832–835, 1926.

[35] K. S. Pedersen and H. P. Ronningsen. Effect of precipitated wax on viscosity - A model for predicting non-Newtonian viscosity of crude oils. *Energy & Fuels*, 14(1):43–51, Jan-Feb 2000.

[36] T. K. Perkins and J. B. Turner. Starting behavior of gathering lines and pipelines filled with gelled prudhoe bay oil. *Journal of Petroleum Technology*, 23(3):301–308, 1971.

[37] J. Ratulowski, A. Amin, A. Hammami, M Muhammad, M. Riding, and Schlumberger. Flow assurance and subsea productivity: Closing the loop with connectivity and measurements. In *SPE Annual Technical Conference and Exhibition, 26-29 September 2004, Houston, Texas*, AIP Conference Proceedings. Society of Petroleum Engineers, 2004.

[38] G. P. Roberts, H. A. Barnes, and P. Carew. Modelling the flow behaviour of very shear-thinning liquids. *Chemical Engineering Science*, 56(19):5617–5623, Oct 2001.

[39] V Sharma, K Park, and M Srinivasarao. Colloidal dispersion of gold nanorods: Historical background, optical properties, seed-mediated synthesis, shape separation and self-assembly. *Materials Science & Engineering R-Reports*, 65(1-3):1–38, May 2009.

[40] V. Simanzhenkov and R. Idem. *Crude Oil Chemistry.* Marcel Dekker Inc., 2003.

[41] J. G. Speight. *The Chemistry and Technology of Petroleum.* CRC Press, fourth edition, 2007.

[42] P Tapadia, S Ravindranath, and SQ Wang. Banding in entangled polymer fluids under oscillatory shearing. *Physical Review Letters*, 96(19), MAY 19 2006.

[43] P Tapadia and SQ Wang. Direct visualization of continuous simple shear in non-newtonian polymeric fluids. *Physical Review Letters*, 96(1), Jan 2006.

[44] M Tsoskounogiou, G. Ayerides, and E. Tritopoulou. The end of cheap oil: Current status and prospects. *Energy Policy*, 36(10):3797–3806, OCT 2008.

[45] R. Venkatesan, J. A. Ostlund, H. Chawla, P. Wattana, M. Nyden, and H. S. Fogler. The effect of asphaltenes on the gelation of waxy oils. *Energy and Fuels*, 17(6):1630–1640, 2003.

[46] G. Vinay, A. Wachs, and I. Frigaard. Start-up transients and efficient computation of isothermal waxy crude oil flows. *Journal of Non-Newtonian Fluid Mechanics*, 143(2-3):141–156, May 18 2007.

[47] R. F. G. Visintin, R. Lapasin, E. Vignati, P. D'Antona, and T. P. Lockhart. Rheological behavior and structural interpretation of waxy crude oil gels. *Langmuir*, 21(14):6240–6249, 2005.

[48] R. F. G. Visintin, T. P. Lockhart, R. Lapasin, and P. D'Antona. Structure of waxy crude oil emulsion gels. *Journal of Non-Newtonian Fluid Mechanics*, 149:34–39, 2008.

[49] L. T. Wardhaugh and D. V. Boger. Flow Characteristics of Waxy Crude Oils - Application to Pipeline Design. *AICHE Journal*, 37(6):871–885, Jun 1991.

[50] L. T. Wardhaugh and D. V. Boger. The measurement and description of the yielding behavior of waxy crude oil. *Journal of Rheology*, 35(6):301–308, 1991.

[51] A. Yoshimura and R. K. Prudhomme. Wall slip corrections for couette and parallel disk viscometers. *Journal of Rheology*, 32(1):53–67, Jan 1988.